ADVANCED TRENDS IN NONLINEAR OPTICS APPLIED TO DISTRIBUTED OPTICAL-FIBRE SENSORS

THÈSE N^{O} 3648 (2006)

PRÉSENTÉE LE 20 OCTOBRE 2006

À LA FACULTÉ SCIENCES ET TECHNIQUES DE L'INGÉNIEUR

Laboratoire de nanophotonique et métrologie

SECTION DE GÉNIE ÉLECTRIQUE ET ÉLECTRONIQUE

ÉCOLE POLYTECHNIQUE FÉDÉRALE DE LAUSANNE

POUR L'OBTENTION DU GRADE DE DOCTEUR ÈS SCIENCES

PAR

Dario ALASIA

laurea in ingegneria elettronica, Politecnico di Torino, Italie
ingénieur électricien diplômé EPF
et de nationalité italienne

acceptée sur proposition du jury:

Prof. C. Depeursinge, président du jury
Dr L. Thévenaz, directeur de thèse
Prof. Ph. Emplit, rapporteur
Prof. M. Gonzalez Herraez, rapporteur
Prof. N. Grandjean, rapporteur

ÉCOLE POLYTECHNIQUE
FÉDÉRALE DE LAUSANNE

Lausanne, EPFL
2006

La science a eu des merveilleuses applications; mais la science qui n'aurait en vue que les applications ne serait plus de la science, elle ne serait plus que de la cuisine. Il n'y a pas d'autre science que la science désintéressée.

Henri Poincaré, 1911

Abstract

The distributed optical-fibre sensors based on the properties of Brillouin scattering is the central object of this thesis. In the past decade, optical fibres have gained a large interest as sensors: attractive solutions based on the non-linear stimulated Brillouin scattering have been proposed in the early 90s and the possibility to achieve long-range fully distributed strain measurements has been extensively demonstrated. The Brillouin interaction is responsible for the coupling between two optical waves and an acoustic wave when a resonance condition is fulfilled. Since the resonance condition is strain and temperature-dependent, by determining the resonance frequency we directly get a measure of temperature or strain. Local information about the acousto-optical resonance condition is typically obtained by using pulsed lightwaves and a classical time-of-flight technique (BOTDA technique).

The main goal of this work has been the development of an innovative technique for the generation of optical signals, using a set of locked lasers - instead of the traditional techniques using external modulators. The utilisation of the injection-locking of semiconductor lasers is the key of the entire set-up and represents an entirely new and original approach, since it brings significant improvements in terms of SNR and costs.

As long as intense pulses propagate along the fibre, the optical signals can be seriously degraded by several nonlinear interactions occurring inside the fibre; we show that the nonlinear effect exhibiting the lowest threshold power is the modulation instability (MI) process. From the study of the dynamic behaviour of MI we could observe the Fermi-Pasta-Ulam (FPU) recurrence over few periods in very comfortable conditions.

One original application of Brillouin sensing has been the dosimetric measurement of ionising radiations in a nuclear environment. The measurement campaign has not only shown that distributed sensors based on Brillouin spectral analysis are radiation tolerant up to very high doses, but has also revealed the first observation - to our knowledge - of the negative compaction of silica in fibres.

Distributed fibre sensors based on stimulated Brillouin scattering offer a unique capability for the analysis of optical signals and nonlinear phenomena in optical fibres. We present a generalised theoretical approach to the problem of localised sensing and report on the first distributed measurement - to our knowledge - of the parametric gain in a single-pump fibre-optics parametric amplifier (FOPA).

Keywords*: nonlinear optics, Brillouin scattering, optical fibres, distributed measurements, modulation instability, four-wave mixing, semiconductor lasers, injection locking, radiation effects, silica compaction, optical signals analysis, parametric amplification.*

Version abrégée

Les capteurs distribués à fibre optique basées sur les propriétés de la diffusion Brillouin font l'objet de cette thèse. Au cours de la décennie passée, les fibres optiques ont suscité un grand intérêt en tant que capteurs : des solutions attrayantes basées sur la diffusion non linéaire Brillouin stimulée ont été proposées au début des années '90 et la possibilité de réaliser des mesures de contrainte entièrement distribuées à longue portée a été largement démontrée. L'interaction Brillouin est responsable du couplage entre deux ondes optiques et une onde acoustique, quand une condition de résonance est remplie. Puisque cette condition est dépendante des contraintes et de la température, en déterminant la fréquence de résonance, on obtient directement une mesure de la température ou des déformations subies par la fibre. En employant des ondes lumineuses pulsées et une technique classique de temps-de-vol (technique de BOTDA) on peut obtenir une information locale sur les charactéristiques de la résonance acousto-optique.

Le but principal de ce travail a été le développement d'une technique innovatrice pour la génération des signaux optiques, utilisant un jeu de lasers verrouillés - au lieu des techniques traditionnelles qui utilisent des modulateurs externes. La mise en oeuvre du verrouillage par injection de lasers à semicon-

ducteur est le point central de tout le montage expérimental et représente une approche entièrement nouvelle et originale, puisqu'elle apporte des améliorations significatives en termes de rapport signal-sur-bruit (SNR) et de coûts.

Au fur et à mesure que des impulsions intenses se propagent le long de la fibre, les signaux optiques peuvent être sérieusement dégradés par le truchement de plusieurs interactions non-linéaires se produisant à l'intérieur de la fibre ; on montre que l'effet non-linéaire manifestant la plus basse puissance de seuil est le processus d'instabilité de modulation (MI). De l'étude du comportement dynamique de l'instabilité de modulation, nous avons pu observer dans des conditions très confortables la récurrence de Fermi-Pasta-Ulam (FPU) sur quelques périodes.

Une application originale des capteurs Brillouin a été la mesure dosimétrique des rayonnements ionisants dans un environnement radioactif. La campagne de mesure a non seulement montré que les capteurs distribuées basées sur l'analyse spectrale Brillouin sont largement insensibles aux rayonnements jusqu'à des doses très élevées, mais nous a également permis d'observer pour la première fois - à notre connaissance - la compaction négative de la silice dans les fibres optiques.

Les capteurs distribuées basées sur la diffusion Brillouin stimulée offrent des possibilités uniques pour l'analyse des signaux optiques et des phénomènes non-linéaires dans les fibres optiques. Nous proposons une approche théorique généralisée du problème de la mesure localisée et présentons également la première mesure distribuée - à notre connaissance - du gain paramétrique dans un amplificateur paramétrique à fibre optique (FOPA).

Mots-clés *: optique nonlinéaire, diffusion Brillouin, instabilité de modulation, verrouillage par injection, effets de radiation.*

Remerciements

J'aimerais d'abord exprimer toute ma gratitude au Dr. Luc Thévenaz pour m'avoir accueilli au sein de son groupe et pour avoir dirigé cette thèse. Son apport scientifique, son soutien et les nombreuses discussions que j'ai eu le plaisir d'avoir avec lui, sans oublier la confiance qu'il a su m'accorder, ont rendu mon parcours scientifique non seulement agréable mais aussi intéressant. Ce travail n'aurait pu aboutir sans lui.

J'adresse également mes sincères remerciements au Professeurs Philippe Emplit, Miguel González Herráez et Nicolas Grandjean, membres du jury, pour avoir accepté de juger ce travail et avoir pris le temps de lire ce mémoire.

Ce travail a pu bénéficier de la précieuse collaboration avec le Centre d'Etude de l'Energie Nucléaire (SCK·CEN) de Mol, en Belgique : merci à Alberto Fernandez Fernandez et à Benoit Brichard pour m'avoir fourni les fibres irradiées et pour les intéressantes discussions scientifiques que nous avons eu ensemble. Je tiens également à témoigner ma reconnaissance au Laboratoire d'Optique P. M. Duffieux de l'Université de Franche-Comté de Besançon pour la fructueuse collaboration : un remerciement tout particulier à Armand Vedadi et à Thibaut Sylvestre pour leur apport scientifique et nos discussions amicales.

Un remerciement tout particulier à l'ami Miguel et à son épouse Sonia pour les enrichissantes discussions scientifiques et pour les moments d'amitié échangés ces deux dernières années. Merci également à Sébastien Le Floch pour son enthousiasme contagieux, ses suggestions et nos innombrables disputes épistémologiques.

Merci à Fredo et Pascal pour leur soutien technique et humain, et pour l'incroyable capacité à nous sortir régulièrement d'impasse. Merci à Pierrette Paulou et à Danielle Alvarez pour leur soutien administratif et pour avoir su régler les innombrables et insurmontables problèmes que je leur ai souvent soumis. Merci également aux deux équipes du NAM et du LMAM, en les personnes du Professeur Olivier Martin et du Dr. Kamiar Aminian. Je ne pourrais tous les citer sans courir le risque d'en oublier.

Un chaleureux merci à mes confrères de l'ensemble Mimesis pour leur amitié et leur soutien durant ces derniers mois de travail, en particulier à Pierre Lauper pour nos passionnantes discussions physiques sur la floculation. Un grand merci également à Anne Ramoni, Massimo Nosetti et Anne-Isabelle Desmangles pour leur encouragement, leur soutien inlassable et pour toute l'amitié dont ils ont toujours fait preuve à mon égard. Une pensée particulière va à Jean-Philippe le bernois, Pierangelo le savoyard, Sophie la rieuse, Laura la sarde et Mario le compatriote : leur soutien moral et leur amitié trouveront ici l'expression da ma plus profonde gratitude.

Je ne saurais conclure sans exprimer toute ma reconnaissance à mes parents, pour leur confiance et leur soutien qui m'accompagnent constamment, ainsi qu'à mes frères. Je leur dédie ce travail. Finalement, toute ma gratitude à mon amie Elena pour la patience dont elle a fait preuve et pour son encouragement assidu en cette fin de thèse.

Contents

List of Figures

List of Tables

Chapter 1

Introduction

Mais cependant voila deux Horloges trouvees, qui ne s'ecartent jamais de rien ce qui semblera incroyable: & toutesfois est tresveritable. Jamais d'autres Pendules que de cette nouvelle invention n'ont pu faire la meme chose; & l'on peut voir par la combien elles sont exactes; puis qu'il faut si peu de chose pour les maintenir dans un accord perpetuel.

C. Huygens, 1665

This work mainly owes to the vivid curiosity of Christian Huygens and to the brilliant intuition of Léon Brillouin. The first observation of synchronisation between two distinct oscillators, as well as the prediction of light scattering from the density fluctuations in condensed matter, can be considered true milestones in both theoretical and applied physics. Probably, neither the Dutch scientist nor the French physicist (three centuries later) could foresee the extremely high practical impact of their work on distributed sensors.

Hopefully, with the advent of the laser in the early 60s, the wide availability of intense coherent lightwaves opened new

directions of research, and nonlinear optics started to attract much attention. The injection-locking of two helium-neon laser oscillators could be successfully demonstrated, and the stimulated Brillouin scattering could be experimentally observed in crystals. Successively, with the invention of the first low-loss optical fibres and the advent of the first generation of semiconductor lasers, both Brillouin scattering and injection-locking techniques became prolific domains of interest for almost two decades.

A deeper insight into the mechanisms of the Brillouin scattering revealed that the Brillouin gain curves are actually very sensitive to several extrinsic parameters, like temperature and strain. It was then suggested that the inherent dependence of the Brillouin gain on local environmental variations can be advantageously exploited for making distributed fibre sensors. Attractive solutions based on the non-linear stimulated Brillouin scattering have been proposed in the early 90s and the possibility to achieve long-range fully distributed strain and temperature measurements has been extensively demonstrated.

The basic idea is quite simple. The Brillouin interaction is responsible for the coupling between two optical waves (called respectively pump and probe) and an acoustic wave when a resonance condition is fulfilled. Since the resonance condition is strain and temperature-dependent, by determining the resonance frequency one obtain directly a measure of temperature or strain. Local information about the acousto-optical resonance condition is typically retrieved by using pulsed lightwaves and a classical time-of-flight technique (BOTDA technique). Several experiments have been performed using two distinct lasers for generating pump and probe signals, with a manifest limitation residing in the difficulty to maintain a

stable frequency difference between the two light sources.

The parallel development of both theory and techniques for injection locking provides interesting solutions to overcome this instability. An interesting experimental configuration can then be obtained, combining the benefits of the distributed Brillouin sensing and the potentialities offered by the injection locking concept. The aim of this work is to demonstrate an innovative technique for the generation of the optical signals, and show as well that this brings significant improvements in the performances of distributed sensors, especially in terms of noise immunity and costs.

Nonlinear optics is a fascinating and continuously evolving field, which offers original possibilities of investigations. The high versatility of the Brillouin effect makes actually possible to use distributed sensing in a variety of different configurations. In particular, we present a generalised theoretical approach to the problem of localised sensing and demonstrate unique capability for the analysis of optical signals and nonlinear processes.

Outline of the dissertation

The present work is organised as follows:

Chapter 2 provides some of the mathematical backgrounds needed for a theoretical understanding of the nonlinear phenomena in optical fibres. A particular attention is devoted to the modulation instability process, regarding its detrimental effect on the performances of distributed sensors. From the study of the dynamical behaviour, we were able to experimentally observe the Fermi-Pasta-Ulam recurrence, which predicts reversibility of energy.

Chapter 3 is devoted to the physics of the Brillouin scattering in optical fibres. A general approach to the thermodynamic

nature of spontaneous scattering, as well as the coherent and intensity models describing the nonlinear stimulated Brillouin scattering are presented.

Chapter 4 deals with distributed fibre sensors based on the stimulated Brillouin scattering. The Brillouin optical time domain analysis (BOTDA) technique is described and an original experimental set-up using two injection-locked lasers is presented. The negative role played by modulation instability in long-range high-pulse powers performances is also adressed.

Chapter 5 presents two original applications of distributed sensing involving the dosimetric measurement of ionising radiation in nuclear environments and the distributed analysis of optical signals.

Chapter 6 is devoted to the conclusions.

Chapter 2

Nonlinear effects in single mode optical fibres

The boat suddenly stopped—not so the mass of water in the channel which it had put in motion; it accumulated round the prow of the vessel in a state of violent agitation, then suddenly leaving it behind, rolled forward with great velocity, assuming the form of a large solitary elevation, a rounded, smooth and well defined heap of water, which continued its course along the channel without change of form or diminution of speed.

J. S. Russell, 1834

This chapter provides some of the mathematical backgrounds needed for a theoretical understanding of the nonlinear phenomena in optical fibres. The fundamental equation governing the propagation of electromagnetic fields on nonlinear dispersive fibres is established. A particular attention is devoted to the modulation instability (MI) process whose dynamical behaviour exhibits the Fermi-Pasta-Ulam (FPU) recurrence.

2.1 Fibre nonlinearities

The response of any dielectric to light becomes nonlinear when exposed to intense electromagnetic fields. The origin of the nonlinear response is related to anharmonic motion of bound electrons and charge reorientation under the influence of applied field [1, 2]. As a result, the induced polarization $\mathbf{P}$ from the electric dipoles is not linear in the electric field $\mathbf{E}$ and satisfies the equation:[1]

$$\begin{aligned}\mathbf{P} &= \epsilon_0 \left(\boldsymbol{\chi}^{(1)} \otimes \mathbf{E} + \boldsymbol{\chi}^{(2)} \otimes \mathbf{EE} + \boldsymbol{\chi}^{(3)} \otimes \mathbf{EEE} + ... \right) \\ &= \mathbf{P}_L^{(1)} + \mathbf{P}_{NL}^{(2)} + \mathbf{P}_{NL}^{(3)} + ...\end{aligned} \tag{2.1}$$

where ϵ_0 is the vacuum permittivity, $\boldsymbol{\chi}^{(j)}$ are tensors of rank $(j+1)$ representing the jth order susceptibility, and the $\otimes$ products are tensorial products (the spatial and time dependences have been omitted for simplicity and the response of the medium has been supposed to be instantaneous).

The dominant contribution to the polarisation is the linear susceptibility $\boldsymbol{\chi}^{(1)}$ whose effects are included through the Kramers-Krönig relations in the refractive index n and the attenuation coefficient α.

The second-order susceptibility $\boldsymbol{\chi}^{(2)}$ is responsible for many effects like second harmonic generation (SHG) and sum frequency generation (SFG) in materials with a lack of inversion symmetry at molecular level. In optical fibres, principally made of silica which is an amorphous medium, it is actually negligible as a result of the macroscopic inversion symmetry of the material. In fact, the existence of a centre of inversion implies that the properties of the medium have no preferred

[1] Within the convention adopted throughout this dissertation, vector and tensor quantities appear in bold typeface, unless specified differently.

$P^{(2)}_{NL,n} = 2\sum_{k,l} \chi^{(2)}_{nkl}(-\omega_n, \omega_k, \omega_l) E_k E_l$		
$-\omega_n, \omega_k, \omega_l$	Identification	Susceptibility
$-\omega, 0, \omega$	PE	$\Re(\chi^{(2)})$
$0, -\omega, \omega$	OR	$\Re(\chi^{(2)})$
$-2\omega, \omega, \omega$	SHG	$\Re(\chi^{(2)})$
$-\omega_3, \omega_1, \omega_2$	SFG	$\Re(\chi^{(2)})$
$-\omega_3, \omega_1, -\omega_2$	DFG, PG	$\Re(\chi^{(2)})$

Table 2.1: Selected second-order processes. PE: Pockels effect; OR: optical rectification; SHG: second harmonic generation; SFG: sum-frequency generation; DFG: difference-frequency generation; PG: parametric gain. The following frequency convention has been adopted [2]: $-\omega_n + \omega_k + \omega_l = 0$.

direction: $\mathbf{P}^{(2)}_{NL}(-\mathbf{E}) = -\mathbf{P}^{(2)}_{NL}(\mathbf{E})$. As a result, $\chi^{(2)}_{ijk} = 0$ and optical fibres do not normally exhibit second-order nonlinear effects[2] [3, 4]. A selection of second-order processes is given in table 2.1.

2.1.1 Nonlinear refraction

The third-order susceptibility $\boldsymbol{\chi}^{(3)}$ is responsible for the lowest-order nonlinear effects in fibres such as third-harmonic generation (THG), four-wave mixing (FWM) and nonlinear refraction. These phenomena can be considered *elastic* in the sense that there is no exchange between the electromagnetic field and the dielectric medium, the entire energy of the wave remaining within the wave (see discussion on parametric processes on

[2]Weak second-order effects can although be generated, under particular phase-matching conditions, by the existence of electric-quadrupole and magnetic-dipole moments. We will ignore these effects in the frame of this work.

$P_{NL,n}^{(3)} = 4 \sum_{k,l,m} \chi_{nklm}^{(3)}(-\omega_n, \omega_k, \omega_l, \omega_m) E_k E_l E_m$		
$-\omega_n, \omega_k, \omega_l, \omega_m$	Identification	Susceptibility
$-\omega, \omega, -\omega, \omega$	SPM	$\Re(\chi^{(3)})$
$-\omega_2, \omega_1, -\omega_1, \omega_2$	XPM	$\Re(\chi^{(3)})$
$-\omega_B, \omega_L, -\omega_L, \omega_B$	SBS, SRS	$\Im(\chi^{(3)})$
$-\omega_a, \omega_p, \omega_p, -\omega_s$	CARS	$\Im(\chi^{(3)})$
$-\omega_i, \omega_p, \omega_p, -\omega_s$	PG	$\Re(\chi^{(3)})$
$-\omega_3, \omega_1, \omega_2, -\omega_4$	FWM	$\Re(\chi^{(3)})$

Table 2.2: Selected third-order processes. SPM: self-phase modulation; XPM: cross-phase modulation; SBS: stimulated Brillouin scattering; SRS: stimulated Raman scattering; CARS: coherent anti-Stokes Raman scattering; PG: parametric gain; FWM: four-wave mixing. The following frequency convention has been adopted [2]: $-\omega_n + \omega_k + \omega_l + \omega_m = 0$.

page 48). Since the processes leading to the generation of new frequencies are poorly efficient in optical fibres - on account of the difficulties to achieve a good phase matching - the main contribution originates from *nonlinear refraction*.

This phenomenon refers to the dependence of the refractive index upon the intensity of the electromagnetic field, resulting from the contribution of $\boldsymbol{\chi}^{(3)}$:

$$n(I) = n_0 + n_2 I \tag{2.2}$$

where I is the optical intensity ($\mathrm{W/m^2}$) inside the fibre, n_0 is the linear part, and n_2 ($\mathrm{m^2/W}$) is the nonlinear-index related to the only component of $\boldsymbol{\chi}^{(3)}$ by the relation $n_2 = \frac{3}{8n_0}\chi_{xxxx}^{(3)}$. n_2 has been experimentally evaluated [5] and is approximately equal to $2.2 \cdot 10^{-20}$ $\mathrm{m^2W^{-1}}$ in silica.

A selection of third-order processes is given in table 2.2. It

is worth to cite here two classes of effects most widely studied in nonlinear optics:

- *Self-phase modulation (SPM)*: an optical field experiences a self-induced phase shift during the propagation within the fibre:

$$\phi_{NL} = n_2 I k_0 L \tag{2.3}$$

  where k_0 is the wavevector and L is the fibre length. This phenomenon is responsible for spectral broadening of ultrashort pulses and for soliton generation.

- *Cross-phase modulation (XPM)*: an optical field at wavelength λ_1 experiences a phase shift induced by a copropagating field at a different wavelength λ_2:

$$\phi_{NL} = n_2 k_0 L(I_1 + 2I_2) \tag{2.4}$$

  The second term in the right-hand side is responsible for the asymmetric spectral broadening of copropagative pulses.[3]

2.1.2 Inelastic scattering

A second class of nonlinear effects results from stimulated *inelastic* scattering in which the optical field transfers part of its energy to the nonlinear medium. Among these effects, two important phenomena in optical fibres are related to vibrational excitation modes of silica: the stimulated Raman scattering (SRS) and the stimulated Brillouin scattering (SBS). The main

[3]The factor of 2 on the right-hand side shows that XPM is twice as effective as SPM for the same intensity, and specifically occurs for copolarised optical waves.

difference is that optical phonons are involved in the SRS process while acoustic phonons participate in SBS interaction.

Within a simple quantum-mechanical approach applicable to both SRS and SBS, a photon coming from the incident field is annihilated to create a photon to a downshifted frequency (which is called *Stokes* frequency) and a phonon with right energy and momentum to satisfy both conservation principles. On the other hand, a photon to an up-shifted frequency (which is called *anti-Stokes* frequency) can also be created if a phonon of right energy and momentum exists in the medium.

In spite of the similarities in the origins of the two processes, the different dispersion relations lead to some basic differences between the two: the major one is that SBS can only occur in the backward direction whereas SRS is more dominant in the forward direction. In the framework of this thesis, we will focus principally on the SBS which will be discussed in more details in Chapter 3.

2.2 Wave propagation in nonlinear media

To examine the propagation behaviour of an optical wave in a material, we need to consider the coupling between the light waves and the induced polarization in the matter. The starting point is Maxwell's equations for macroscopic variables, here listed in their general form (in SI units):

$$\nabla \times \mathbf{E}(\mathbf{r},t) = -\frac{\partial \mathbf{B}(\mathbf{r},t)}{\partial t} \tag{2.5a}$$

$$\nabla \times \mathbf{H}(\mathbf{r},t) = \frac{\partial \mathbf{D}(\mathbf{r},t)}{\partial t} + \mathbf{J}(\mathbf{r},t) \tag{2.5b}$$

$$\nabla \mathbf{D}(\mathbf{r},t) = \rho(\mathbf{r},t) \tag{2.5c}$$

$$\nabla \mathbf{B}(\mathbf{r},t) = 0 \tag{2.5d}$$

where **E** and **H** are respectively electric and magnetic field vectors and **D** and **B** are the corresponding electric and magnetic flux densities; ρ is the density of free charges and **J** the corresponding current density vector. In dielectric media (such as optical fibres) which contain only bound charges one has rigorously $\mathbf{J}(\mathbf{r},t)=0$ and $\rho(\mathbf{r},t)=0$.

The electric displacement **D** and the magnetic induction **B** vectors are related to the electric **E** and magnetic **H** fields by the following constitutive relations [6]:

$$\mathbf{D}(\mathbf{r},t) = \epsilon_0\mathbf{E}(\mathbf{r},t)+\mathbf{P}(\mathbf{r},t) \tag{2.6}$$

$$\mathbf{B}(\mathbf{r},t) = \mu_0\mathbf{H}(\mathbf{r},t)+\mathbf{M}(\mathbf{r},t) \tag{2.7}$$

where ϵ_0 is the vacuum permittivity, μ_0 is the vacuum permeability, **P** is the macroscopic polarization density (electric dipole moment per volume) and **M** is the magnetization (magnetic dipole moment per volume) of the medium. Since an optical fibre is a non-magnetic medium we assume $\mathbf{M}=0$.

By taking the curl of (2.5a) and using (2.6), (2.7) and (2.5b) one gets:

$$\begin{aligned}\nabla\times\nabla\times\mathbf{E}(\mathbf{r},t) &= -\frac{\partial}{\partial t}\nabla\times\mathbf{B}(\mathbf{r},t)\\ &= -\mu_0\frac{\partial}{\partial t}\nabla\times\mathbf{H}(\mathbf{r},t)\\ &= -\mu_0\frac{\partial}{\partial t}\frac{\partial\mathbf{D}(\mathbf{r},t)}{\partial t}\\ &= -\mu_0\left(\epsilon_0\frac{\partial^2\mathbf{E}(\mathbf{r},t)}{\partial t^2}+\frac{\partial^2\mathbf{P}(\mathbf{r},t)}{\partial t^2}\right)\end{aligned} \tag{2.8}$$

Since $\mu_0\epsilon_0=1/c^2$, with c being the speed of light in vacuum, we finally obtain a driven vector equation for the electric field

in time domain:

$$\nabla \times \nabla \times \mathbf{E}(\mathbf{r},t) + \frac{1}{c^2}\frac{\partial^2 \mathbf{E}(\mathbf{r},t)}{\partial t^2} = -\mu_0 \frac{\partial^2 \mathbf{P}(\mathbf{r},t)}{\partial t^2} \tag{2.9}$$

which is the most general form of the wave equation in nonlinear optics. It can be simplified by using the following vector identity:

$$\nabla \times \nabla \times \mathbf{E} = \nabla(\nabla \mathbf{E}) - \nabla^2 \mathbf{E} = -\nabla^2 \mathbf{E} \tag{2.10}$$

and by supposing that the first term in the right-hand side vanishes because $\nabla \mathbf{E}$ is very small for cases of interest.[4]

To complete the description and close the problem, a relation between $\mathbf{P}$ and $\mathbf{E}$ is needed. In general the evaluation of $\mathbf{P}$ requires a quantum-mechanical approach, especially if the optical frequency is near the medium resonance. However, in the range of interest $(0.5 - 2\mu\text{m})$ for the study of nonlinear effects in optical fibres, we are far from the medium resonances and a phenomenological relation can be used in a way similar

[4] In the linear optics of isotropic source-free media, the first term in (2.10) vanishes because $\nabla \mathbf{D} = 0$ implies that $\nabla \mathbf{E} = 0$. In nonlinear optics this term is generally non vanishing even for isotropic materials, owing to the more general relation (2.6) between $\mathbf{D}$ and $\mathbf{E}$. Fortunately it can be shown to be very small, especially when the slowly-varying amplitude approximation is valid.

to a series expansion in the field strength:

$$\begin{aligned}\mathbf{P}(\mathbf{r},t) = \epsilon_0 &\int_{-\infty}^{\infty} \boldsymbol{\chi}^{(1)}(t-t_1) \otimes \mathbf{E}(\mathbf{r},t_1)dt_1 \\ &+ \epsilon_0 \iint_{-\infty}^{\infty} \boldsymbol{\chi}^{(2)}(t-t_1,t-t_2) \otimes \mathbf{E}(\mathbf{r},t_1)\mathbf{E}(\mathbf{r},t_1)dt_1dt_2 \\ &+ \epsilon_0 \iiint_{-\infty}^{\infty} \boldsymbol{\chi}^{(3)}(t-t_1,t-t_2,t-t_3) \otimes \mathbf{E}(\mathbf{r},t_1)\cdot \\ &\qquad \cdot \mathbf{E}(\mathbf{r},t_2)\mathbf{E}(\mathbf{r},t_3)dt_1dt_2dt_3 + \dots\end{aligned} \tag{2.11}$$

The first term associated to $\boldsymbol{\chi}^{(1)}$ represents the linear response of the fibre and is responsible for the wave propagation when the power is low:

$$\mathbf{P}_L(\mathbf{r},t) = \epsilon_0 \int_{-\infty}^{\infty} \boldsymbol{\chi}^{(1)}(t-t_1) \otimes \mathbf{E}(\mathbf{r},t_1)dt_1 \tag{2.12}$$

As discussed previously in section 2.1, the second term associated to $\boldsymbol{\chi}^{(2)}$ is vanishing due to the symmetry properties of the silica molecule. The principal contribution to the nonlinear polarization is thus represented by the term associated to $\boldsymbol{\chi}^{(3)}$:

$$\begin{aligned}\mathbf{P}_{NL}(\mathbf{r},t) = \epsilon_0 &\iiint_{-\infty}^{\infty} \boldsymbol{\chi}^{(3)}(t-t_1,t-t_2,t-t_3) \otimes \mathbf{E}(\mathbf{r},t_1)\cdot \\ &\qquad \cdot \mathbf{E}(\mathbf{r},t_2)\mathbf{E}(\mathbf{r},t_3)dt_1dt_2dt_3 + \dots\end{aligned} \tag{2.13}$$

All the terms of order greater than three do not contribute significantly to the nonlinear polarization and have hence been

neglected. The polarization reduces finally to:

$$\mathbf{P}(\mathbf{r},t) = \mathbf{P}_L(\mathbf{r},t) + \mathbf{P}_{NL}(\mathbf{r},t) \tag{2.14}$$

and the formalism for dealing with the nonlinearities in fibres is completely described by (2.9), and (2.12)-(2.14). Since the nonlinear effects are relatively weak ($|\mathbf{P}_{NL}| \ll \mathbf{P}_L$) in silica fibres, a simplification can be made by considering the nonlinear polarization $\mathbf{P}_{NL}$ as a small perturbation to the linear regime discussed below.

2.2.1 Linear regime

In this section we focus on the solutions of the wave equation when nonlinearities are negligible ($\mathbf{P}_{NL} = 0$). Because (2.9) is linear in $\mathbf{E}$, we can work in the frequency domain:

$$\nabla \times \nabla \times \tilde{\mathbf{E}}(\mathbf{r},\omega) - \frac{\omega^2}{c^2}\tilde{\mathbf{E}}(\mathbf{r},\omega) = \mu_0\omega^2\tilde{\mathbf{P}}_L(\mathbf{r},\omega) \tag{2.15}$$

by expressing $\mathbf{E}(\mathbf{r},t)$ and $\mathbf{P}(\mathbf{r},t)$ in terms of their Fourier transforms

$$\tilde{\mathbf{E}}(\mathbf{r},\omega) = \int_{-\infty}^{+\infty} \mathbf{E}(\mathbf{r},t)\exp(-i\omega t)dt \tag{2.16a}$$

$$\tilde{\mathbf{P}}_L(\mathbf{r},\omega) = \int_{-\infty}^{+\infty} \mathbf{P}_L(\mathbf{r},t)\exp(-i\omega t)dt \tag{2.16b}$$

Using (2.10) and (2.12), the wave equation takes the following form:

$$\nabla^2\tilde{\mathbf{E}}(\mathbf{r},\omega) + \boldsymbol{\epsilon}(\omega)\frac{\omega^2}{c^2}\tilde{\mathbf{E}}(\mathbf{r},\omega) = 0 \tag{2.17}$$

where $\boldsymbol{\epsilon}(\omega) = 1 + \tilde{\boldsymbol{\chi}}^{(1)}(\omega)$ is the frequency-dependent dielectric tensor and $\tilde{\boldsymbol{\chi}}^{(1)}(\omega)$ is the Fourier transform of $\boldsymbol{\chi}^{(1)}(t)$.

Since $\tilde{\boldsymbol{\chi}}^{(1)}(\omega)$ is symmetrical [2] and the fibre is an isotropic medium, the dielectric tensor can be described by his unique scalar component $\tilde{\chi}^{(1)}(\omega)$ and the dielectric constant becomes: $\epsilon(\omega) = 1 + \tilde{\chi}^{(1)}(\omega)$.

The attenuation and the refractive index of the fibre are related to the real and imaginary parts of the susceptibility by the relations

$$n(\omega) = 1 + \frac{1}{2}\Re[\tilde{\chi}^{(1)}(\omega)] \tag{2.18a}$$

$$\alpha(\omega) = \frac{\omega}{nc}\Im[\tilde{\chi}^{(1)}(\omega)] \tag{2.18b}$$

and contribute to the dielectric constant in the following way:

$$\epsilon = (n + i\alpha c/2\omega)^2 \tag{2.19}$$

Because of the low optical losses in fibres, the imaginary part is negligible in comparison to the real part and we can replace $\epsilon(\omega)$ by $n^2(\omega)$ obtaining the final form of (2.17):

$$\nabla^2\tilde{\mathbf{E}}(\mathbf{r},\omega) + n^2(\omega)\frac{\omega^2}{c^2}\tilde{\mathbf{E}}(\mathbf{r},\omega) = 0 \tag{2.20}$$

To solve (2.20) it is usual to rewrite the problem in cylindrical coordinates and consider just one component of the electric field,[5] typically $\tilde{E}_z(\mathbf{r},\omega)$. Applying the separation of variables method, we will look for solutions of the form

$$\tilde{E}_z(\rho,\phi,z,\omega) = \tilde{A}(\omega)F(\rho)\exp(im\phi)\exp(i\beta z) \tag{2.21}$$

[5]Since **E** and **H** satisfy Maxwell's equations (2.5a)-(2.5d), only two components among six are independent. Due to the cylindrical symmetry of optical fibres, it is customary to choose $\tilde{E}_z$ and $\tilde{H}_z$ as independent variables and obtain the transverse components in terms of the longitudinal ones.

where $\tilde{A}(\omega)$ is the amplitude term, $F(\rho)$ a modal function, m an integer identifying the mode and β the propagation constant. By substituting one finds:

$$\frac{\partial^2 F}{\partial \rho^2} + \frac{1}{\rho}\frac{\delta F}{\delta \rho} + \left(n^2(\rho,\omega)k_0^2 - \beta^2(\omega) - \frac{m^2}{\rho^2} \right) F = 0 \qquad (2.22)$$

with $k_0 = \omega/c$.

The physical solutions are unambiguously determined by the radial dependence of the refractive index. For a step-index fibre of core radius a, the profile is given by:

$$n(\rho) = \begin{cases} \hat{n}_1 & \text{for} \quad \rho < a \\ \hat{n}_2 & \text{for} \quad \rho > a \end{cases} \qquad (2.23)$$

and the transverse distributions are respectively

$$F(\rho < a) = J_m(\kappa\rho) \quad \text{with} \quad \kappa = (\hat{n}_1^2 k_0^2 - \beta^2) \qquad (2.24)$$

in the core, and

$$F(\rho > a) = K_m(\gamma\rho) \quad \text{with} \quad \gamma = (\beta^2 - \hat{n}_2^2 k_0^2) \qquad (2.25)$$

in the cladding, where J_m and K_m represent the ordinary and modified Bessel's functions of order m.

In the case of the fundamental mode, the modal distribution can be approximated by a Gaussian distribution of the form:

$$F(\rho) = e^{-\frac{\rho^2}{w^2}} \qquad (2.26)$$

where w represents the effective radius occupied by the mode.

The propagation constant is obtained by solving the eigenvalue equation associated to (2.22) and its frequency dependence results from the frequency and radial dependence of the refractive index. Approximate analytic expressions exist in particular cases, although the evaluation of $\beta(\omega)$ generally requires a numerical approach [7].

2.2.2 Chromatic dispersion

The frequency dependence of the propagation constant $\beta(\omega)$ plays a critical role in the propagation of optical waves, especially in the case of short optical pulses, since each different spectral component travels at a different speed. In the linear regime, dispersion-induced broadening can be detrimental for optical communication systems. In the nonlinear regime the combination of dispersion and nonlinearities can result in a very different behaviour, giving rise to a variety of interesting applications and phenomena.

From a mathematical point of view, the effects of fibre dispersion are accounted for by considering a quasi monochromatic field, with its spectrum centred at a frequency ω_0 and a spectral width $\Delta\omega$, such that $|\Delta\omega| \ll \omega_0$. The propagation constant can thus be expanded in a Taylor series about the centre frequency:

$$\beta(\omega) = \beta_0 + \beta_1(\omega - \omega_0) + \frac{1}{2}\beta_2(\omega - \omega_0)^2 + \dots \tag{2.27}$$

where

$$\beta_i(\omega) = \left.\frac{d^i\beta}{d\omega^i}\right|_{\omega=\omega_0} \qquad (i = 0, 1, 2, ...) \tag{2.28}$$

From a physical point of view, β_1 is inversely related to the group velocity:

$$v_g = \frac{d\omega}{d\beta} = \frac{1}{\beta_1} \tag{2.29}$$

The group velocity is the speed at which the pulse shape, or more generally the wave envelope, moves along the fibre. In dispersive media, it is different from the phase velocity, which represents the speed of the wavefronts of a plane wave, but even if they are not identically equal, their value is approximately

the same (about $2 \cdot 10^8$ m $\cdot$ s^{-1}) in the windows of transparency of silica.

The parameter β_2 is also related to the group velocity in the following way:

$$\beta_2 = \frac{d\beta_1}{d\omega} = \frac{d}{d\omega}\left(\frac{1}{v_g}\right) = \frac{d\tau_g}{d\omega} \tag{2.30}$$

where τ_g is the group delay per unit length. β_2 takes account of the variations of the group delay experienced by the different spectral components around the central frequency ω_0 and is therefore responsible for the broadening of pulses propagating along the fibre in the linear regime. This is the reason why β_2 is often referred to as the group-velocity-dispersion (GVD) coefficient. In the fibre-optics literature and in the optical communication domain, it is common to use another parameter, D, in stead of β_2, called *chromatic dispersion*. It is related to β_2 by the relation:

$$D = \frac{d\beta_1}{d\lambda} = -\frac{2\pi c}{\lambda^2}\beta_2 \tag{2.31}$$

From a dimensional point of view, β_2 is measured in ps$^2 \cdot$km^{-1} and D in ps $\cdot$ nm$^{-1} \cdot$ km^{-1}. Figure 2.1 shows the typical measured dispersion curves of two commercially-available fibres.

One notable feature is that the chromatic dispersion curve of standard fibres vanishes at a certain wavelength λ_0, called *zero-dispersion* wavelength (ZDW).[6] Fibres with modified dispersion characteristics (obtained for instance using two or four

[6]It should, however, be noted that when pulses propagate near λ_0 the cubic and higher-order terms have to be be included in (2.27), and the dispersion does not vanish at $\lambda = \lambda_0$. Such higher-order effects can bring significant distortion both in the linear and nonlinear regime. Within the range of few nanometres around λ_0 their inclusion is no longer necessary.

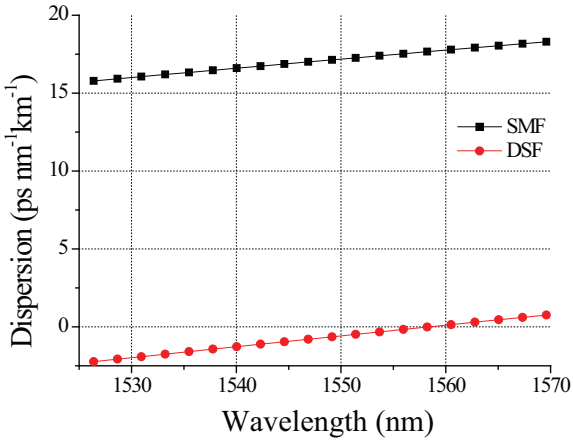

Figure 2.1: Measured variations of dispersion coefficient D with wavelength for a single mode fibre (SMF) and a dispersion shifted fibre (DSF).

cladding layers around the core) actually exhibit two ZDWs [8]. For wavelengths such that $\beta_2 > 0$ ($D < 0$), the fibre is said to exhibit *normal dispersion*, whereas for wavelengths such that $\beta_2 < 0$ ($D > 0$), the fibre exhibits *anomalous dispersion*. This kind of terminology clearly identifies two different regimes in which the interplay between the GVD and the nonlinearities leads to a qualitatively different behaviour. In one case, for example, the fibre can be used for pulse compression, while in the other case the fibre can support optical solitons, as it will be discussed later.

2.2.3 Nonlinear regime

In this section we focus on the solution of (2.9) when nonlinearities are present and the term (2.13) is no longer negligible.

Several simplifying assumptions are necessary in order to derive the basic propagation equation.

First, we consider that the polarization is maintained constant along the fibre so that a scalar approach is valid: this implies that only one component, $\chi^{(3)}_{xxxx}$, of the susceptibility tensor $\boldsymbol{\chi}^{(3)}$ is used.[7] Second, we assume that the optical field is quasi-monochromatic, so that it is possible to separate the rapidly-varying part of the electric field from the slowly-varying envelope (SVEA approximation):

$$\mathbf{E}(\mathbf{r},\omega) = \frac{1}{2}\hat{\mathbf{x}}\Re[E(\mathbf{r},t)\exp(-i\omega t)] \tag{2.32a}$$

$$\mathbf{P}_N(\mathbf{r},\omega) = \frac{1}{2}\hat{\mathbf{x}}\Re[P_N(\mathbf{r},t)\exp(-i\omega t)] \tag{2.32b}$$

$$\mathbf{P}_{NL}(\mathbf{r},\omega) = \frac{1}{2}\hat{\mathbf{x}}\Re[P_{NL}(\mathbf{r},t)\exp(-i\omega t)] \tag{2.32c}$$

Third, since the nonlinear effects are relatively weak in fibres, we consider the nonlinear polarization P_{NL} as a small perturbation to P_L. This results in an additional term in the total dielectric constant

$$\epsilon(t) = 1 + \chi^{(1)}(t) + \epsilon_{NL}(t) \tag{2.33}$$

given by:

$$\epsilon_{NL}(t) = \frac{3}{4}\chi^{(3)}_{xxxx}|E(\mathbf{r},t)|^2 \tag{2.34}$$

[7] In an isotropic medium, the third-order susceptibility $\boldsymbol{\chi}^{(3)}$ has only four non-zero components: $\chi^{(3)}_{xxxx}$, $\chi^{(3)}_{xxyy}$, $\chi^{(3)}_{xyxy}$ and $\chi^{(3)}_{xyyx}$. Far from the transition frequencies of the medium, the overall permutation-symmetry [2,9] implies that only one non-zero independent element remains eventually: $\chi^{(3)}_{xxyy} = \chi^{(3)}_{xyxy} = \chi^{(3)}_{xyyx} = \frac{1}{3}\chi^{(3)}_{xxxx}$. As a consequence, the response of the medium exhibits only two privileged directions: parallel and perpendicular to the wave polarization.

Finally, we will make the usual assumption that the nonlinear response of the fibre is instantaneous and we neglect the contribution of the molecular vibrations to $\boldsymbol{\chi}^{(3)}$. The vibrational (Raman) response occurring over a time scale of $\tau_R = 60$-70 fs in silica fibres, it is usual to consider this approximation valid for pulse widths down to the picoseconds range. We will see how to include the Raman contribution later.

The approach used to obtain the wave equation for the slowly-varying amplitude $E(\mathbf{r}, t)$ is very similar to that used for the linear regime in section 2.2.1. In particular we suppose that the solution can be written by separating variables in the form:

$$E(\mathbf{r}, t) = F(x, y)A(z, t)\exp(i\beta_0 z) \tag{2.35}$$

where $F(x, y)$ represents the radial distribution of the field, $A(z, t)$ the longitudinal slowly-varying function and β_0 the wavenumber.

Within the first-order perturbation theory, the radial distribution is not affected by the existence of nonlinear effects in the fibre and $F(x, y)$ still satisfies (2.22). The wavenumber, instead, becomes intensity dependent through an additional term affecting also the longitudinal propagation.

The details of the solution are quite complex and can be found in [3, 10]. Here, we report simply the resulting equation for the complex function $A(z, t)$:

$$\frac{\partial A}{\partial z} + \beta_1 \frac{\partial A}{\partial t} + i\frac{\beta_2}{2}\frac{\partial^2 A}{\partial t^2} + \frac{\alpha}{2}A = i\gamma|A|^2 A \tag{2.36}$$

where the spatial and temporal dependences have been omitted for simplicity and the amplitude function $A(z, t)$ is assumed to be normalised such that $P(z, t) = |A(z, t)|^2$ represents the optical power. γ is called the nonlinear coefficient of the fibre

and is defined by:

$$\gamma = \frac{n_2 \omega_0}{c A_{eff}} = \frac{3 \chi_{xxxx} \omega_0}{8 n c A_{eff}} \tag{2.37}$$

where n_2 is the nonlinear index introduced in section 2.1.1.

The parameter A_{eff} is known as the effective core area and represents the area effectively occupied by the optical field inside the fibre. It is related to the modal distribution by:

$$A_{eff} = \frac{\left(\iint_{-\infty}^{+\infty} |F(x,y)|^2 dx dy \right)^2}{\iint_{-\infty}^{+\infty} |F(x,y)|^4 dx dy} \tag{2.38}$$

and its typical values are about 85 μm^2 for single mode fibres and about 50 μm^2 for dispersion-shifted fibres.

The basic propagation equation (2.36) is usually rewritten using a retarded frame of reference moving at the group velocity. By making the following transformation

$$\tau = t - z/v_g = t - \beta_1 z \tag{2.39}$$

we easily obtain:

$$\frac{\partial A}{\partial z} + i \frac{\beta_2}{2} \frac{\partial^2 A}{\partial \tau^2} + \frac{\alpha}{2} A = i \gamma |A|^2 A \tag{2.40}$$

This particular form of the propagation equation is often referred to as the nonlinear Schrödinger equation (NLSE) and has been the starting point of all the investigations on soliton propagation in fibres.[8] It is also responsible for the modulation instability process whose dynamical evolution exhibits some remarkable properties we will discuss in the next section.

[8] Rigourously, (2.40) reduces to the actual nonliner Schrödinger equation with nonlinear potential only when $\alpha = 0$.

Delayed nonlinear response

The above equation has been derived within the assumption that the nonlinear response of the fibre is instantaneous. In general the response of the material exhibits some delay or inertia, meaning that the polarization of the medium is non resonant with the incident electric field. This is due to the fact that both electrons and nuclei respond to the optical field in a nonlinear and non-instantaneous manner. The delayed molecular contribution to the susceptibility tensor can be included in the propagation equation in the following way:

$$\frac{\partial A}{\partial z} + i\frac{\beta_2}{2}\frac{\partial^2 A}{\partial \tau^2} + \frac{\alpha}{2}A = i\gamma A\left[|A|^2 * R(\tau)\right] \tag{2.41}$$

where $*$ denotes the convolution product and $R(\tau)$ the nonlinear response function of the fibre.

Within the Born-Oppenheimer approximation [2,11], $R(\tau)$ is normalised such that $\int_0^\infty R(\tau) = 1$ and takes the form:

$$R(\tau) = (1 - f_R)\delta(\tau) + f_R h_R(\tau) \tag{2.42}$$

where $\delta(\tau)$ is the delta function and f_R represents the fractional contribution of the delayed Raman response to the nonlinear response of the fibre and is tipically estimated to be about 0.18. h_R is the Raman response function and can be expressed in an approximate analytic way:

$$h_R(\tau) = \frac{\tau_1^2 + \tau_2^2}{\tau_1 \tau_2^2} e^{-\tau/\tau_2} \sin(\tau/\tau_1) u(\tau) \tag{2.43}$$

where $u(\tau)$ is the Heaviside function and $\tau_1 = 12.2$ fs and $\tau_2 = 32$ fs are chosen to fit the actual Raman gain spectrum.

The extended equation (2.41) governs the evolution of very short pulses (down to femtoseconds range) and is used to describe fast-type interactions in fibres. It is also responsible for

interesting higher-order effects and has been extensively studied in relation to soliton self-frequency shift [12].

Effective lengths

It is useful to introduce here some length scales that are commonly employed in fibre optics literature. We refer to [3] (chapters 3 and 9) for further details.

First of all, the effective interaction length, that keeps into account the distance over which the nonlinear effects interact along the fibre:

$$L_{eff}(L) = \int_0^L e^{-\alpha z} dz = \frac{1 - e^{-\alpha L}}{\alpha} \tag{2.44}$$

where L represents the fibre length. For small values of length $L_{eff} \approx L$, whereas for big lengths it reduces to $L_{eff} \approx 1/\alpha \approx$ 21.7 km.

The dispersion length

$$L_D = \frac{T_0^2}{|\beta_2|} \tag{2.45}$$

where T_0 is the initial width of a pulse propagating in the fibre, represents the lengths over which the dispersive effects become important for the pulse evolution.

Similarly, the nonlinear length

$$L_{NL} = \frac{1}{\gamma |P_0|} \tag{2.46}$$

represents the distance over which the nonlinear effects take place within the fibre. Depending on the relative magnitudes of L, L_D and L_{NL}, the interplay of nonlinearities and dispersive effects can give rise to very different behaviours during the propagation of optical waves.

2.3 The nonlinear Schrödinger equation: basic dynamical effects

The nonlinear Schrödinger equation (NLSE) is a universal physical model providing a canonical description for the envelope dynamics of quasi-monochromatic plane waves propagating in weakly-nonlinear dispersive media [13, 14]. It arises in various physical contexts and can be applied, besides nonlinear optics [15–18], to hydrodynamics [19–21], nonlinear acoustics, quantum condensates [22], heat pulses in solids, molecular chains [23], plasma physics [24,25] and various other nonlinear instability phenomena [26]. The NLSE assumes weak nonlinearities but a finite dispersion at the scale of the carrying wave; in situations where both dispersion and nonlinearities are equally weak a 'reductive perturbative expansion' leads to the important class of long-wavelength equations, like Korteweg-de Vries and Benjamin-Ono equations [14, 27]. NLSE can also be viewed as the adiabatic limit of the more complex Zacharov systems, currently used as a model for the study of Langmuir and Alfven waves in plasmas, and the Dawey-Stewartson systems, providing canonical description of two-dimensional wave packets [14, 28].

On short times and relatively short distances, these equations exhibit linear dynamics, but cumulative nonlinear interactions can result in a significant and intense modulation of the wave amplitude on large time and space scales. As a consequence, new spectral components appear around the carrier wave up- and down-shifted by the modulation frequency. The process by which these sidebands grow exponentially during the propagation within the medium is referred to as *modulation instability (MI)* or *Benjamin-Feir instability*, after the name of the first discoverers investigating deep water waves [29]. The

phenomenon has been observed independently in nonlinear optics [30] and cold plasmas [31], and has gained a great interest in optical fibres since the first observations two decades ago [32]. Since then, it has been extensively exploited for the generation of ultrashort pulses with high repetition rate [33] and more recently as a basis for the generation of supercontinuum sources [34]. More generally, this effect is also responsible for self-focusing, self-collapsing and wave-packet contraction [14].

The growth of the unstable modulation, however, represents only the first stage of the instability. At later stages of evolution, the wave tends to demodulate and return to its original state. The energy of the system, initially confined to very few low modes, spreads to many higher modes due to the instability, but eventually returns back to the original low modes. This process repeats periodically in time and is known as *Fermi-Pasta-Ulam (FPU) recurrence* [35], by the name of the three scientists who first predicted it within the study of anharmonic lattice vibrations.[9] Further studies on the nature of the recurrence paradox have successively brought to the formulation of complete integrability of nonlinear differential equations and to the discovery of solitary stable waves, called *solitons* [39]. The occurrence within the NLSE has been experimentally verified in a large variety of research do-

[9] Fermi, Pasta and Ulam wanted to investigate the evolution of a crystal towards thermal equilibrium, by simulating a chain of particles linked by a quadratic interaction potential and a weak nonlinear interaction. They expected that the nonlinear coupling between the vibration modes would lead to an irreversible equipartition of energy, as predicted by the ergodicity hypothesis of traditional statistical mechanics. On the contrary, the long-time dynamics appeared to be periodic, with almost perfect returns to the initial conditions. A comprehensive review of the phenomenon can be found in [36–38].

mains [31, 40–46] and more recently has been demonstrated also in optical fibres [47, 48]. A comprehensive analytical approach is still lacking, but the problem can be efficiently studied, in particular conditions, restricting the analysis to the lowest order Fourier modes [49–52]. For more complex and general cases, however, a numerical approach is best suitable.

In this section, we start discussing the theoretical model dealing with the modulation instability process in optical fibres, with a particular attention to the nonlinear dynamics in the strong conversion regime. Finally, we conclude reporting on our experimental observation of the FPU recurrence and on the reversible behaviour of modulation instability.

2.3.1 Modulation instability

Modulation instability in optical fibres result from the interplay between nonlinearities and dispersion, and its typical manifestation consists in a spontaneous break up of the initially perturbed continuous wave into a periodic solitonlike pulse train [53–55]. It can also be interpreted, in the frequency domain, as a degenerate four-wave mixing process in which an intense pump wave transfers energy to a pair of weak sidebands located symmetrically on each side of the pump wave (see section 2.4.2).

A rigorous approach to the problem moves from the the NLSE (2.40), in which we have neglected the fibre losses ($\alpha = 0$):

$$\frac{\partial A}{\partial z} + i\frac{\beta_2}{2}\frac{\partial^2 A}{\partial \tau^2} = i\gamma|A|^2 A \tag{2.47}$$

Focusing on a pure continuous wave propagating inside the fibre, the equation (2.47) admits a plane wave stationary solu-

tion with an intensity-dependent phase shift of the form:

$$A(z,\tau) = \sqrt{P_0} e^{i\gamma P_0 z}. \tag{2.48}$$

We can study the linear stability of this solution considering an infinitesimal perturbation $a(z,\tau)$ of the amplitude:

$$A(z,\tau) = \left[\sqrt{P_0} + a(z,\tau)\right] e^{i\gamma P_0 z}. \tag{2.49}$$

where P_0 is assumed constant and $|a(z,\tau)|^2 \ll P_0$. By substituting (2.49) in (2.47), and linearizing with respect to a we obtain:

$$\frac{\partial a}{\partial z} + i\frac{\beta_2}{2}\frac{\partial^2 a}{\partial \tau^2} = i\gamma P_0 (a + a^*) \tag{2.50}$$

Looking for harmonic perturbations proportional to $e^{i\Omega\tau} e^{Kz}$, this leads to the following dispersion relation:

$$K = \pm\frac{1}{2}\,|\beta_2|\,\Omega\sqrt{-\Omega^2 - \mathrm{sgn}(\beta_2)\Omega_c^2} \tag{2.51}$$

where $\Omega_c = \sqrt{4\gamma P_0/|\beta_2|}$ and K and Ω are respectively the wave number and the frequency of the perturbation.

From the equation (2.51) it is easy to see that the stability of the stationary solution strongly depends on the sign of β_2. In the normal dispersion regime ($\beta_2 > 0$), K is imaginary for all Ω and the wave amplitude remains bounded. In the anomalous regime ($\beta_2 < 0$), on the contrary, K exhibits a positive real part for $\Omega < \Omega_c$ and the perturbation is exponentially amplified with z. Therefore, MI occurs only in the anomalous regime and can be explained as the instability of a wave train of wave number κ relatively to disturbances in the form of a large-scale long-time modulation, or equivalently in the form of two sideband modes $\kappa \pm K$ appearing in the spectral domain.

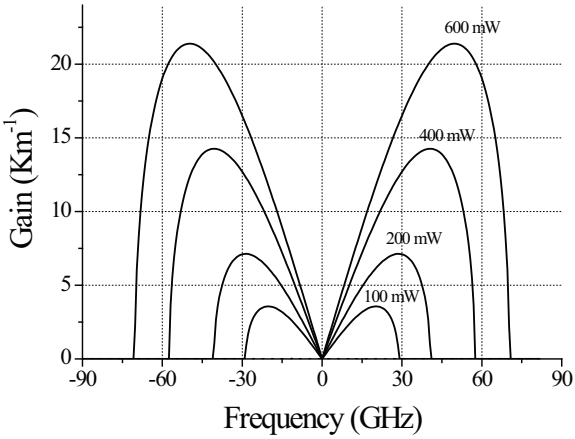

Figure 2.2: Theoretical curves showing the dependence of modulation instability spectra on several power levels. The parameters are those typical for SMF: $\beta_2 = -21.9$ ps^{2}km^{-1} and $\gamma = 1.78$ W^{-1}km^{-1} at 1550 nm.

The spectral gain curve of modulation instability is easily given by:

$$g(\Omega) = 2\Re(K) = |\beta_2\Omega| \sqrt{\Omega_c^2 - \Omega^2} \tag{2.52}$$

and is shown in Fig. 2.2 for different power levels. The maximum occurs at two frequencies shifted by Ω_{max} from the incident frequency

$$\Omega_{max} = \pm\frac{\Omega_c}{\sqrt{2}} = \pm\sqrt{\frac{2\gamma P_0}{|\beta_2|}} \tag{2.53}$$

and has the corresponding value $g_{max} = 2\gamma P_0$, which is independent of the dispersion and increases linearly with the incident power. Since g_{max} has the dimension of an inverse of a distance, the total gain along the fibre is simply obtained

multiplying g_{max} by the interaction length. When the fibre losses are taken into account, however, the critical frequency Ω_c previously calculated has to be replaced by $\Omega_c e^{-\alpha z/2}$: as a direct consequence the gain is significantly reduced and eventually vanishes as the fibre length goes to infinity. A detailed study of MI in lossy optical fibres is reported in [56] and its impact on coherent transmission systems is analysed in [57]. An interesting generalization of the linear stability analysis to the extended NLSE (2.41) can be found in [58, 59].

An evident effect of spontaneous[10] MI is the appearance of spectral lobes located symmetrically at $\pm\Omega_{max}$ on both sides of the pump[11] frequency. This corresponds, in the time domain, to the conversion of the continuous (or quasi-continuous) wave beam into a periodic pulse train with a period equal to $T = 2\pi/\Omega_{max}$. In Fig. 2.3 we show the power spectra of spontaneous MI measured at the output of a SMF fibre as a function of two different launched peak powers, while in Fig. 2.4 we show the shape of a typical pulse measured at the output of the same fibre. This measurement has been made by means of a second-harmonic-based autocorrelator, developed in our laboratory.

2.3.2 Solitons

The nonlinear development of the modulational instability in the time domain leads to the formation of self-similar structures resulting from an exact balance between the dispersive

[10] We make the distinction between a *spontaneous MI* seeded by spontaneous or thermally generated photons, and an *induced MI* seeded by one or two probe waves propagating with the incident wave.

[11] Here *pump* indicates the incident wave. The use of this terminology will be clearer when discussing parametric amplifiers (cf. section 2.4.2) and fibre sensors (see chapter 4).

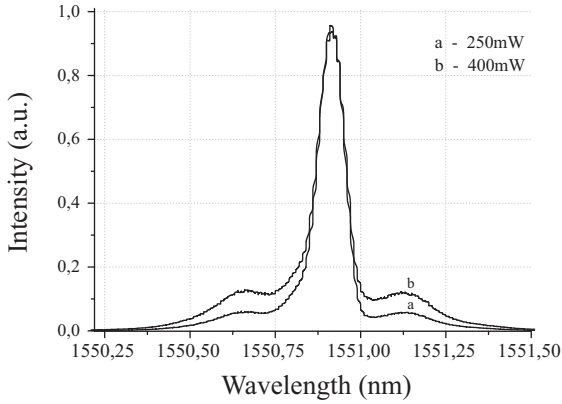

Figure 2.3: Experimental observation of spontaneous MI. The power spectra have been measured at the output of a 11.8 km long SMF fibre in the anomalous dispersion region ($\beta_2 = -21.92\,\mathrm{ps}^2\,\mathrm{km}^{-1}$). The input lightwave was a 20 ns pulse.

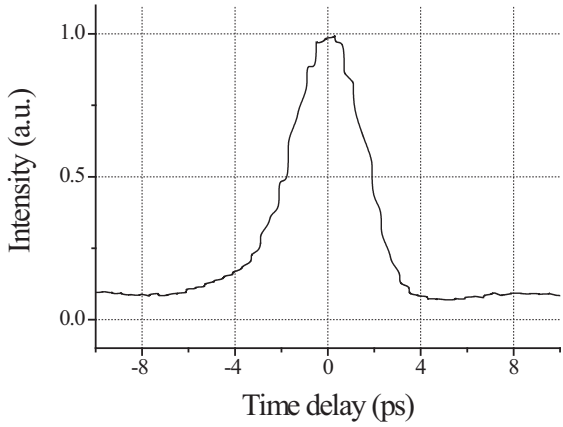

Figure 2.4: Autocorrelation trace of 20-ns input pulses measured at the output of a 11.8 km long fibre, showing the breaking into a 4 ps soliton-like pulse, measured at the FWHM. The input peak power was 300 mW.

and nonlinear effects. These structures are generally called solitons (often collapsons in plasma physics) and have the interesting property of keeping their form unchanged during the propagation within the medium [16].

From a mathematical point of view, they can be derived as the stationary solutions of the equation (2.47). Operating the following normalization

$$u = N\frac{A}{\sqrt{P_0}} \qquad \zeta = \frac{z}{L_D} \qquad \theta = \frac{\tau}{T_0} \tag{2.54}$$

we easily obtain the canonical form:

$$i\frac{\partial u}{\partial \zeta} + \frac{1}{2}\frac{\partial^2 u}{\partial \theta^2} + |u|^2 u = 0 \tag{2.55}$$

The parameter $N = \sqrt{\gamma P_0 T_0^2/|\beta_2|}$ is called the *order* of the soliton and identifies the shape and the number of solutions admitted by the equation (2.55).

The fundamental soliton corresponds to the case $N = 1$. Looking for solutions of the form $u(\zeta, \theta) = v(\theta)e^{i\kappa\zeta}$, where κ is a constant, and solving the ordinary differential equation satisfied by $v(\theta)$, we finally get:

$$u(\zeta, \theta) = \operatorname{sech}(\theta)e^{i\zeta/2} \tag{2.56}$$

In the context of optical fibres, the solution (2.56) indicates that if we are able to launch a hyperbolic-secant pulse inside an ideal lossless fibre, provided that $N = 1$ (i.e., $\gamma P_0 T_0^2 = |\beta_2|$), the pulse will propagate undistorted without change in shape for arbitrarily long distances. This feature makes the fundamental soliton particularly attracting for information transmission in optical systems, especially because it can be excited at power levels available from standard semiconductor lasers.

Higher-order solitons can be found integrating the equation (2.55) by the inverse scattering transform (IST). The description of this method, which reduces the resolution of the initial value problem to that of an inverse scattering problem for an associated linear eigenvalue equation, is quite complex and is beyond the scope of our work. We refer to [18, 27, 60] for more details. The integrability by IST leads, however, to some interesting conclusions: firstly, for a large class of initial conditions vanishing at infinity, the solutions evolve asymptotically in time to a finite set of solitons with some radiation escaping to infinity; secondly, solitons can strongly interact with other solitons, but they emerge from the collision unchanged apart from a phase shift.

2.3.3 Dynamical evolution of the instability in the strong conversion regime

The theoretical model introduced in the above section is very useful to predict the first stages of the instability and the initial soliton build-up. Since it relies on a perturbative approach, however, it does not bring any information about the longterm behaviour of modulationaly unstable waves. The exponential growth of the weak spontaneous sidebands, or equivalently the amplification of co-propagating probe waves, occurs at the expense of the pump power. Once the pump is significantly depleted, the growth is no longer exponential and other energy transfer processes take place in the fibre.

2.3.3.1 Three-wave mixing (TWM) model

A convenient technique for going beyond the limit of validity of the linear stability consists in an analytic treatment based on a truncated three-wave model [51]: in this approach the

phenomenology of the instability is limited to the interaction between the pump wave and the two first symmetric sidebands, provided there are no other spectral components falling inside the MI gain.

The waves situated at $\mp\Omega$ with respect to the pump frequency are respectively called Stokes and anti-Stokes waves, or signal and idler if we refer to the case of induced MI (see section 2.4.2). We consider that the total transverse electric field propagating along the fibre may be written as:

$$E(x,y,z,t) = f(x,y)[E_p(z)e^{i\beta_0 z} + E_s(z)e^{i(\beta_s z+\Omega t)} + E_a(z)e^{i(\beta_a z-\Omega t)}]e^{-i\omega t} \quad (2.57)$$

where $f(x,y)$ is the common transverse modal profile, $E_p(z)$, $E_s(z)$ and $E_a(z)$ are the complex amplitudes of the pump, Stokes and anti-Stokes waves, and $\beta_p = \beta(\omega)$, $\beta_s = \beta(\omega-\Omega)$ and $\beta_a = \beta(\omega+\Omega)$ are the propagation constants evaluated at the relative frequencies.

By substituting in the NLSE (2.36) and by retaining only the terms which are phase-matched, the evolution of the system is then described by the following equations:

$$-i\frac{dE_p}{dz} = \gamma\left[|E_p|^2 + 2(|E_s|^2 + |E_a|^2)\right]E_p + 2\gamma E_s E_a E_p^* e^{-i\Delta\beta z} \quad (2.58a)$$

$$-i\frac{dE_s}{dz} = \gamma\left[|E_s|^2 + 2(|E_a|^2 + |E_p|^2)\right]E_s + 2\gamma E_a^* E_p^2 e^{i\Delta\beta z} \quad (2.58b)$$

$$-i\frac{dE_a}{dz} = \gamma\left[|E_a|^2 + 2(|E_s|^2 + |E_p|^2)\right]E_a + 2\gamma E_s^* E_p^2 e^{i\Delta\beta z} \quad (2.58c)$$

where γ is the nonlinear coefficient, and $\Delta\beta = 2\beta_p - \beta_s - \beta_a = \beta_2\Omega^2$ represents the linear wave-vector mismatch. The first

terms in the right-hand sides are self-phase modulation terms, whereas the last cubic terms are are responsible for the energy exchange among waves.

We can conveniently rewrite the equations (2.58) in terms of amplitudes and phases of the waves through the relations $E_j = |E_j|\exp(i\Phi_j) = A_j\exp(i\Phi_j)$ with $j = (0, s, a)$. Since the total power $P_{tot} = |E_p|^2 + |E_a|^2 + |E_s|^2$ is conserved, it is more practical to work with normalised dimensionless variables defined as follows: $\eta(z) = A_p^2/(P_{tot})$ and $a_{a,s}(z) = A_{a,s}/(P_{tot})^{1/2}$. Finally, making a scaling on the longitudinal coordinate $\xi = \gamma P_{tot} z$, as suggested in [48], the number of effective equations reduces to the following four:

$$\frac{d\eta}{d\xi} = -4\eta a_s a_a \sin\Phi \tag{2.59a}$$

$$\frac{da_s}{d\xi} = \eta a_a \sin\Phi \tag{2.59b}$$

$$\frac{da_a}{d\xi} = \eta a_s \sin\Phi \tag{2.59c}$$

$$\begin{aligned}\frac{d\Phi}{d\xi} = \kappa_L &+ \left[2\eta - (a_s^2 + a_a^2)\right]\sin\Phi \\ &+ \left[\eta\left(\frac{a_s}{a_a} + \frac{a_a}{a_s}\right) - 4a_s a_a\right]\cos\Phi\end{aligned} \tag{2.59d}$$

where $\Phi(\xi) = \kappa_L\xi + \Phi_a(\xi) + \Phi_s(\xi) - 2\Phi_p(\xi)$ is the phase governing the degenerate four-wave mixing process (see section 2.4.1) and $\kappa_L = \beta_2\Omega^2/\gamma P_{tot}$ is the normalised linear wave-vector mismatch.

As it can be easily verified from the equations (2.59), the power flow between the pump and the sidebands only depends on their relative phase. When $\sin\Phi > 0$ the power flows from the pump to the sidebands, while for $\sin\Phi < 0$ power

flows from sidebands back to the pump. The maximum power transfer (or gain) is expected for $\Phi = \pm\pi/2$. The information about the phase matching is entirely contained in the equation (2.59d). In particular, the first term on the right-hand side, κ_L, represents the normalised linear phase mismatch as seen before, whereas the second term, $\kappa_{NL} = 2\eta - (a_s^2 + a_a^2)$, represents the nonlinear contribution due to the self- and cross-phase interaction terms. Considering the propagation of two weak sidebands in the presence of an intense pump wave ($(a_s^2 + a_a^2) \ll \eta \approx 1$) we find that the growth rate reaches a maximum for $\kappa_L = -2$, or equivalently for $|\Omega| = (2\gamma P_{tot}/|\beta_2|)^{1/2}$. This turns out to be nothing but the detuning corresponding to the maximum gain Ω_{max} of modulation instability, found within the linear stability approach.

The set of equations (2.59) admits, besides total power conservation:

$$\eta + a_s^2 + a_a^2 = 1 \tag{2.60}$$

the conservation of the power difference between the two sidebands:

$$\alpha = a_s^2 - a_a^2 \tag{2.61}$$

and the conservation of the following Hamiltonian:

$$H = 4\eta a_s a_a \cos\Phi - (\kappa - 1)\eta - {}^3\!/_2\eta^2 \tag{2.62}$$

By means of these invariant quantities, the analysis of the dynamics can be pursued by reducing the whole system to a single equation for the normalised pump power which is therefore integrable by quadrature [49, 50]. Solutions of this equation can be found in terms of periodic Jacobian elliptic or hyperbolic functions and, for suitable initial conditions, they can exhibit a recurrent behaviour.

On the basis of the first two invariants, it has also been shown [51] that the entire dynamics of the system can be equivalently described by means of a one dimensional Hamiltonian:

$$H(\eta,\Phi) = 2\eta\left[(1-\eta)^2-\alpha^2\right]^{1/2}\cos\Phi-(\kappa-1)\eta-{}^3\!/_2\eta^2 \quad (2.63)$$

as a function only of the pump power and the phase. The canonical conjugate variables (η,Φ) are thus linked together by a set of two self-consistent coupled equations:

$$\frac{d\eta}{d\xi} = \frac{dH}{d\Phi} = -2\eta\left[(1-\eta)^2-\alpha^2\right]^{1/2}\sin\Phi \quad (2.64a)$$

$$\frac{d\Phi}{d\xi} = \frac{dH}{d\eta} = (\kappa-1)+3\eta-2\frac{1+2\eta^2-3\eta-\alpha^2}{[(1-\eta)^2-\alpha^2]^{1/2}}\cos\Phi \quad (2.64b)$$

whose solutions are related to the topology of the phase-space portrait. This model allows immediate insight into the properties of solutions, since closed trajectories clearly identify a recurrent behaviour of the system.

We focus now on the case of initially symmetric weak sidebands. When pump depletion effects are neglected, we have seen that the maximum growth rate of the sidebands is predicted when the nonlinear phase-matching condition is satisfied, i.e. when $\kappa_L = -2$ or equivalently $\Omega = \Omega_{max}$. Provided that the detuning of the sidebands is fixed, the power flows from the pump to the sidebands if $\sin\Phi > 0$. As pump depletion effects cannot be neglected any more (strong conversion regime), the frequency detuning of the sidebands, yielding phase matching, starts to shift towards lower values. As a consequence, the initially phase-matched interaction becomes progressively mismatched and the rate of power transfer saturates, reducing the conversion efficiency. In an opposite way, if the

frequency detuning of the sidebands is lower than Ω_{max}, the waves are initially phase mismatched, but the interaction becomes progressively phase matched because of the pump depletion along the fibre. Better efficiencies can be obtained for such detunings and a complete conversion (full pump depletion) is predicted when $\kappa_L = -1/2$, or equivalently $\Omega = \Omega_{max}/2$. Figures 2.5 and 2.6 show respectively the phase-space portraits and the evolution of the normalised power along the fibre, theoretically calculated for these two cases of interest. The system is supposed to be ideally lossless and exhibit instantaneous response: the effect of the fibre losses and the Raman scattering is simply to speed-up the dynamics and reduce the recurrence period, as addressed in [48].

The description given by the three-wave model efficiently predicts the recurrent nature of the solutions, but provides a good estimation of the recurrence periods only in the first stages of evolution. For longer propagation distances, the dynamics become more complex, since cascaded four-wave mixing effects generate further non-negligible spectral components which make the three-wave model not completely valid: this situation can be very critical when the newly generated sidebands fall within the spectrum of MI. In this case, an approach based on the numerical solutions of the NLSE is more suitable to have a complete description of the behaviour of the system.

2.3.3.2 Reversible behaviour of MI: experimental observation

The theoretical predictions of the TWM model are of a great interest for our work, on account of the serious impact they can have on the performances of fibre sensors based on the Brillouin scattering. As it will be discussed in more details

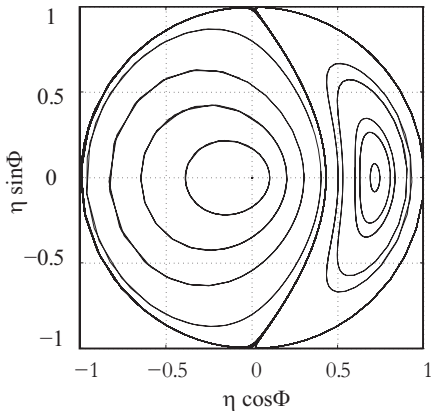

(a)

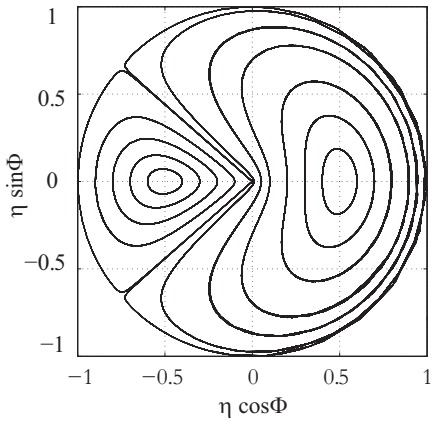

(b)

Figure 2.5: Phase-space portraits describing modulation instability with initially symmetrical weak sidebands. (a) Maximum gain condition: $\kappa = -2$, $\Omega = (2\gamma P_{tot}/|\beta_2|)^{1/2}$. The solutions are divided in two regions of periodic orbits. (b) Full depletion condition: $\kappa = -1/2$, $\Omega = (\gamma P_{tot}/2|\beta_2|)^{1/2}$. The separatrix trajectory has a cusp in the origin.

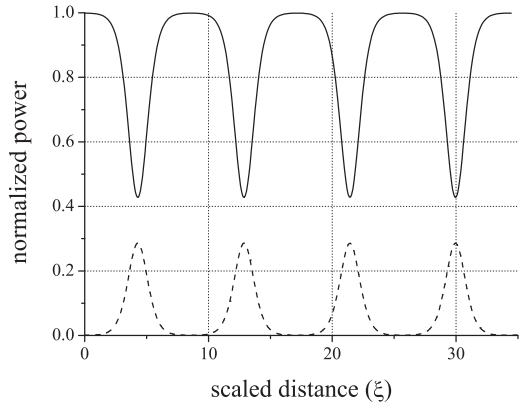

(a)

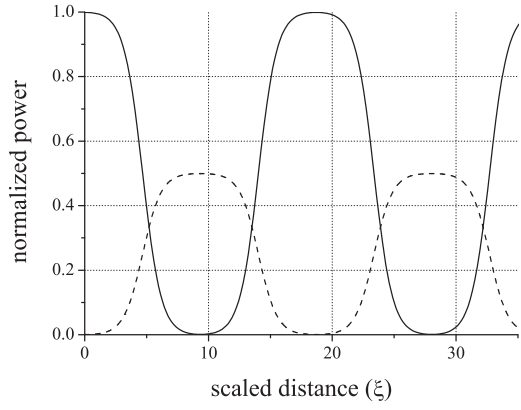

(b)

Figure 2.6: Evolution of the normalised power along the scaled longitudinal coordinate. The solid curves represent the pump power, whereas the dotted curves represent the sidebands power. (a) Maximum gain condition: $\kappa = -2$, $\Omega = (2\gamma P_{tot}/|\beta_2|)^{1/2}$. (b) Full depletion condition: $\kappa = -1/2$, $\Omega = (\gamma P_{tot}/2|\beta_2|)^{1/2}$.

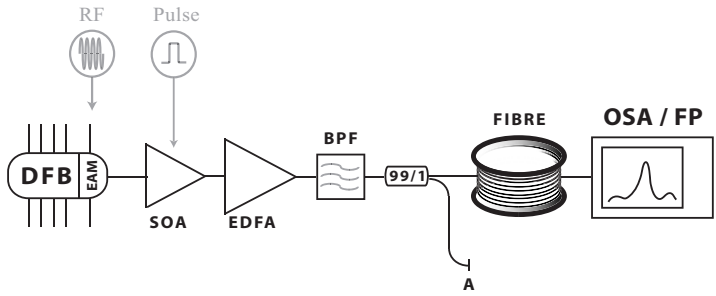

Figure 2.7: Experimental set-up. DFB: laser diode; EAM: electro-absorption modulator; RF: radio frequency generator; SOA: semiconductor optical amplifier; EDFA: erbium-doped amplifier; BPF: optical bandpass filter; OF: optical fibre; OSA: optical spectrum analyser; FP: Fabry-Perot analyser; A: optical port for evaluating the input spectra.

in Chapter 4, the Brillouin probe wave can strongly seed the MI amplification process initiated by the pump pulse and, as a consequence, an energy transfer from pump to probe takes place, causing a depletion of the Brillouin pump wave. The degree of pump depletion significantly depends on the total power of the interaction and on the relative frequency shift between pump and probe. For standard values of the Brillouin shift and for normal operating regimes, both the maximum gain condition and the full depletion condition, predicted by the TWM, can be achieved.

Experimental set-up

Figure 2.7 shows the experimental set-up used to investigate the recurrent behaviour of modulation instability. The source was a distributed feedback laser operating at 1550 nm, co-integrated with an electro-absorption modulator (EAM). The

modulator was driven by an RF generator in order to generate two sidebands situated around the pump which acted as a seed for the MI process. By changing the modulation frequency, the sidebands could be shifted relatively to the pump within the range of real Brillouin frequencies. The continuous wave light was finally gated through a semiconductor optical amplifier (SOA) driven by a pulse generator and boosted using an erbium doped fibre amplifier (EDFA). An optical bandpass filter with a 3 dB bandwidth of 1 nm was used at the output of the EDFA to reduce the additive noise due to the amplified spontaneous emission. The pump and the seed waves were then injected into a 11.8 km long standard single-mode fibre, with $\beta_2 = -21.9$ ps^{2}km^{-1} and $\gamma = 1.78$ W^{-1}km^{-1}, and the output spectra were observed on an optical spectrum analyser. By acting on the amplitude and the repetition rate of the pulses driving the SOA, the pump pulse peak power could be easily varied from 100 to 800mW, and, by acting on the RF modulation amplitude, the relative intensity of the sidebands to the pump could be varied as well. The optical port A, from the 99:1 coupler, was used to monitor the power and the spectrum at the input of the fibre.

While general theories describing the dynamical evolution of MI have continuous waves (CW) as initial conditions, we performed the experiment using square-shaped pulses. The main reason has to be found in the fact that, in optical fibres, the high pump powers required for a rigorous observation of the MI in the CW regime, would activate other nonlinear processes, the stronger of which is Brillouin scattering. This effect could seriously impair the experiment, because it is responsible for significant amounts of pump power depletion, and consequently acts like a dissipative source which negates the predictions of the conservative NLSE [48]. The use of square

pulses, actually, leads to an increase of the power threshold for the Brillouin scattering above the pump power, since the Brillouin gain is considerably reduced by the spectral spreading of the pump [61]. On the other hand, it has also been shown that square-shaped pulses approximate very well the continuous case and keep intact the long-term recurrent behaviour of the instability [48].

Experimental results (I)

We firstly set the sidebands intensity to 1/10 of the pump intensity, and fixed the frequency detuning between the pump wave and the sidebands to 10 GHz which, for an initial power of 100 mW and taking into account the attenuation over 11.8 km of fibre (see section 2.3.1), corresponds approximately to the maximum-gain condition predicted by the TWM model. The output spectra were then recorded at the far end of the fibre, for different values of the total input power. A 13 ns pulse was used and the power was varied between 100 and 750 mW.

Figure 2.8 depicts the dynamic evolution of the MI power spectra as a function of the total power, and figure 2.9 shows the powers of the pump, Stokes and anti-Stokes waves, normalised by the total input power, as a function of the total input power itself. We clearly see that, as far as the input power increases, the pump power gradually flows to the sidebands which undergo an amplification at the expense of the pump. At the same time, the interaction becomes progressively mismatched, as previously discussed, and the growth rate saturates for $P_{tot} \approx 560$ mW. From this point on, the power starts to flow back to the pump and the sidebands tend to return back to the initial state. The pump depletion achieved in this case is about 69%.

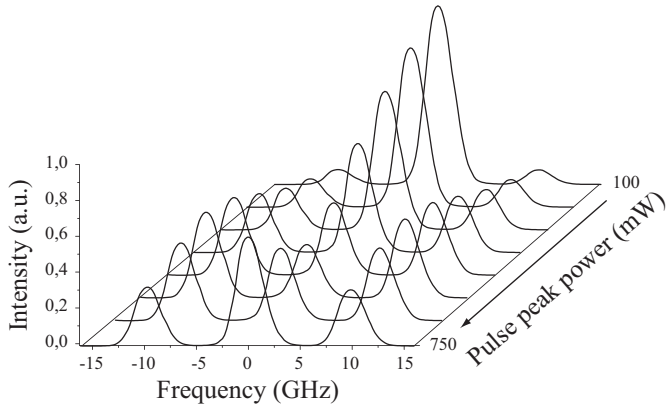

Figure 2.8: Experiment (I). Dynamical observed evolution of the MI power spectra recorded as a function of the input power.

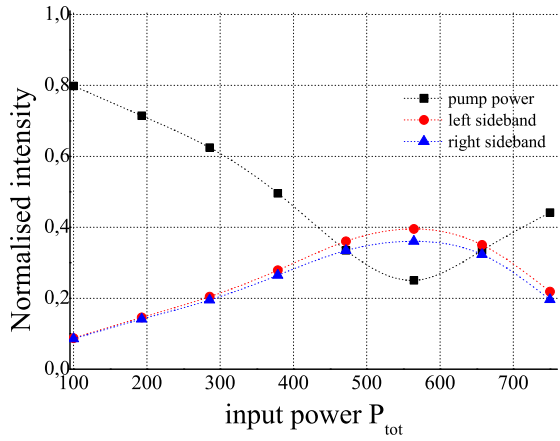

Figure 2.9: Experiment (I). Normalised powers of pump (squares), Stokes (circles) and anti-Stokes (triangles) waves as a function of the scaled distance.

Experimental results (II)
The frequency detuning was fixed to the value of 10.93 GHz which, for an initial total power of about 240 mW, corresponds approximately to the full depletion condition predicted by the TWM model. In this case, the evolution of the induced modulation instability was observed by keeping the input power approximately constant and by varying only the amplitude of the sidebands through the RF generator.

The evolution of the fundamental and of the first low-order modes is shown in figure 2.10 as a function of the RF modulation power. As predicted by the TWM model, the power flows from the pump to the first sidebands until they reach a maximum. At this point the power starts to flow back to the pump, but, since the high-order modes fall within the MI band, a part of the power starts to flow to the second sidebands, too. The process repeats again, and for increasing values of the sidebands amplitude, the interaction involves a significant number of modes as shown in figure 2.11: as a main consequence, the power does not return entirely back to the pump within the range of amplitudes considered. For such a complex dynamics, the TWM analysis loses its validity after the first half-period of recurrence and the interaction must be described by a numerical model.

By varying the sidebands amplitude, the total input power could vary between 240 and 350 mW, spanning the scaled distance ξ ($\xi = \gamma P_{tot} L$, where L is the fibre length) over the range: $\xi \in [5.04, 7.35]$. We numerically solved the NLSE by simulating the physical conditions of our experiment and restricted our analysis to the range $\xi \in [5.04, 6.11]$, over which the total input power and, consequently, the linear mismatch do not change significantly. We report and compare in figure 2.12 the numerical and experimental evolution of the powers

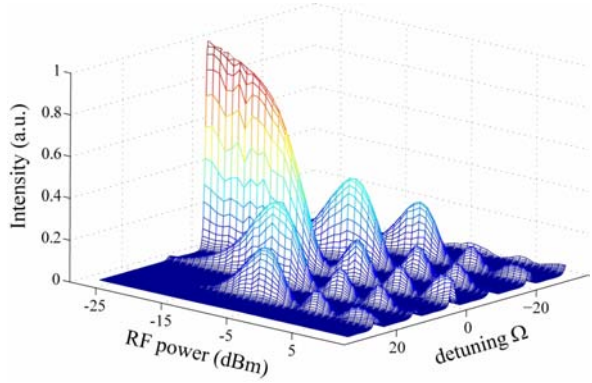

Figure 2.10: Experiment (II). Dynamical evolution of the MI spectra, as a function of the RF modulation power, showing the interaction between the first low-order modes.

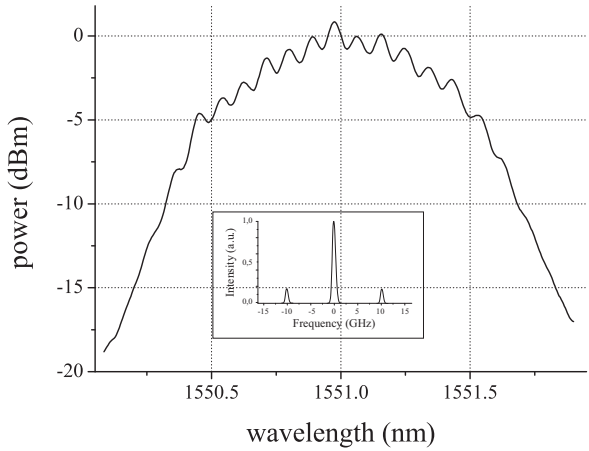

Figure 2.11: Experiment (II). Spectrum recorded at the maximum value of the RF modulation power showing the spreading of energy towards up to fourteen high-order modes. The initial spectrum is shown in the inner plot. The slightly asymmetrical aspect of the spectrum is due to the Raman response of the fibre.

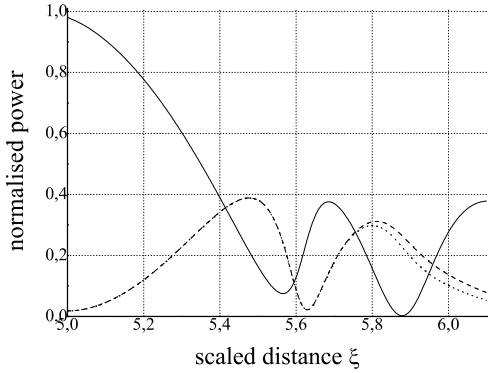

(a)

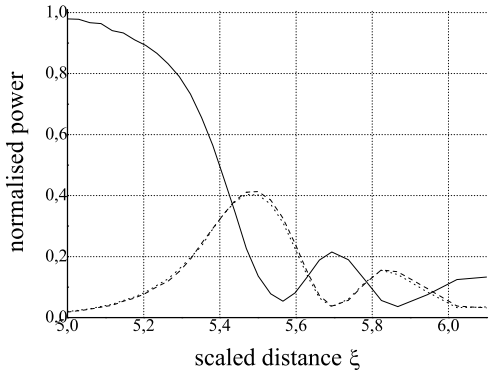

(b)

Figure 2.12: Normalised powers as a function of distance. The solid curve represents the pump wave; the dotted and the dashed curves represent respectively the anti-Stokes and the Stokes modes. (a) Numerical. (b) Experiment.

of the pump, Stokes and anti-Stokes waves, normalised by the total input power, as a function of the scaled distance.

The experimental data are in good agreement with the predictions of the numerical model. In both cases there are two recurrence periods over the range of scaled distance considered, and the evolution in the first half-period is fully comparable. The small differences appearing from $\xi \approx 5.6$ are probably due to the presence of additional nonlinear effects, in particular four wave mixing products, generated in the fibre amplifier and in the semicondctor amplifier, that we have not considered in the numerical approach. This may be a reason to the fact that the theoretical model predicts a full pump depletion (100%), whereas the pump depletion we experimentally observed reaches about 95%.

While extremely interesting from a physical point of view, this behaviour is very critical for distributed sensors, since with such strong depletions distributed measurements are no longer possible, as addressed in section 4.5.

2.4 Parametric processes

As we will discuss in the next chapter, in the stimulated scattering processes the fibre plays an active role as a nonlinear medium through the participation of molecular vibrations or acoustic phonons. In many other nonlinear phenomena instead, the fibre plays a passive role mediating the interaction between several optical waves only through the nonlinear response of bound electrons. Such processes are referred to as parametric processes since they originate from the modula-

tion of the refractive index induced by the propagating light.[12] Within a quantum-mechanical approach, this means that the initial and final states of the system are identical and hence that the photon energy is conserved.[13] Four-wave mixing and parametric amplification fall into this category.

2.4.1 Four-wave mixing (FWM)

Frequency mixing represents one of the most general nonetheless important phenomena in nonlinear optics. In this process, two or more waves interact in a nonlinear medium to produce an output at various sum or difference frequencies. Four-wave mixing [51,62–64] comes from the nonlinear response of bound electrons to the applied optical field, and refers to the interaction of four waves via the third order nonlinear polarization. From the point of view of the nonlinear refraction, assuming two input frequency components ω_1 and ω_2 (with $\omega_2 > \omega_1$), the refractive index is modulated by the difference frequency $\Delta\omega = \omega_2 - \omega_1$, which creates new sidebands for each of the input waves (often referred to as pumps); as a consequence, two new frequency components appear at $\omega_3 = \omega_1 - \Delta\omega = 2\omega_1 - \omega_2$ and $\omega_4 = \omega_2 + \Delta\omega = 2\omega_2 - \omega_1$. The generation of these new frequencies is schematically shown in figure 2.13. From

[12] Historically, the term was used to indicate those nonlinear optical processes for which the Manley-Rowe relations are valid (i.e., those involving pure reactive or lossless systems). Unfortunately, with the passing of time, the meaning has altered and is now much less precise. It is often used to refer broadly to those processes whose efficiencies, in a travelling-wave interaction, depend on phase-matching [2].

[13] Actually, some energy may be exchanged in the course of the interaction between photons and electrons (or phonons), and some photons are allowed to reside in virtual levels: the duration of this stay, however, is governed by the uncertainty principle and after very short intervals of time all the photons return to the initial state.

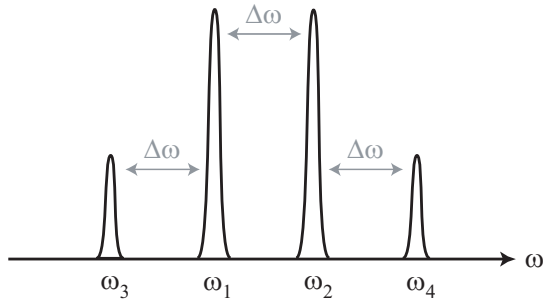

Figure 2.13: Four-wave mixing interaction in optical fibres.

a quantum-mechanical point of view, the process occurs when photons from both pumps are annihilated and new photons are created at different frequencies such that the total energy and the total momentum are conserved during the interaction [3].

The FWM is a phase-sensitive process, since the interaction strongly depends on the relative phases of all involved waves [63]. Its effect can efficiently accumulate over longer distances in a fibre only if the frequencies are symmetrically positioned relatively to each other (as described above) and the wave vectors satisfy a *phase-matching condition*:

$$\Delta\beta = \beta_1 + \beta_2 - \beta_3 - \beta_4 = 0 \tag{2.65}$$

This condition is achieved when the pump frequencies are situated in the vicinity of the zero dispersion wavelength, because only in this region it is possible to have interacting waves with similar group velocities.

The process is referred to as *degenerate* in the particular case in which the two pumps at the input of the fibre coincide ($\omega_1 = \omega_2$). In this situation, we consider that a idler[14] wave

[14]This terminology is borrowed from the field of microwaves and is

(ω_i) is generated from a pump (ω_p) and a signal wave (ω_s), and the whole interaction can be described by the TWM model discussed in section 2.3.3.1.

2.4.2 Parametric amplification

According to the theoretical predictions of the TWM model, the four-wave mixing in the degenerate case is able to transfer energy from a strong pump to two waves, respectively up-shifted and down-shifted in frequency from the pump by an amount $\Delta\omega = \omega_p - \omega_s = \omega_i - \omega_p$. The process is governed by the equations (2.59), where $\Phi(\xi)$ is the relative phase difference between the three involved waves. By controlling the phase relation, we can control the direction of the power flow between the pump and the sidebands, thus creating a *phase-sensitive* amplifier. In other words, by having signal, idler and pump photons present at the fibre input and adjusting their relative phases we are able to decide if the signal will be amplified or attenuated.

In the case of a *phase-insensitive* amplifier (see figure 2.14), we assume a strong pump, a weak signal and the idler to be zero at the input of the fibre. In this special case it results that $\Phi(\xi) = \pi/2$ at the fibre input port [65] and, by consequent, from (2.59), the signal and the idler will start to grow immediately in the fibre. By assuming that the pump remains undepleted during the parametric gain process, we may set $dE_p/dz = 0$ in the equation (2.58a) and derive an analytical

widely used in the literature of parametric amplifiers. In the TWM model the Stokes wave corresponds to the signal wave, and the anti-Stokes wave to the idler wave.

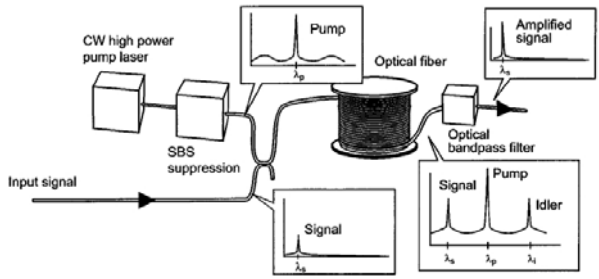

Figure 2.14: General scheme of phase-insensitive fibre-based optical parametric amplifier. From [65].

solution for the signal wave [63]:

$$P_s(L) = P_s(0)\left(1 + \left[\frac{\gamma P_0}{g}\sinh(gL)\right]^2\right) \tag{2.66}$$

where L is the length of the fibre and g is the parametric gain coefficient given by:

$$g^2 = (\gamma P_0)^2 - (\kappa/2)^2 \tag{2.67}$$

with $\kappa = \Delta\beta + 2\gamma P_0$ the total phase mismatch. The unsaturated single pass gain G_s may then be written as:

$$G_s = \frac{P_s(L)}{P_s(0)} = 1 + \left[\frac{\gamma P_0}{g}\sinh(gL)\right]^2 \tag{2.68}$$

Two different regimes can be distinguished in (2.68). For signal wavelengths close to the pump and for small fibre lengths such that the dispersion between the waves can be neglected, we have $\Delta\beta \approx 0$ and the gain reads:

$$G_s \approx 1 + (\gamma P_0 L)^2 \tag{2.69}$$

In stead, in the special case of perfect phase matching $\kappa = 0$ and for $\gamma P_0 L \gg 1$, the gain may be rewritten as:

$$G_s \approx \frac{1}{4} e^{2\gamma P_0 L} \tag{2.70}$$

Equation (2.69) and (2.70) identify respectively the region of quadratic parametric gain and the region of exponential parametric gain.

We conclude this section by observing that the performances of fibre-optics parametric amplifiers (FOPAs) strongly depend on the longitudinal fluctuations of the zero dispersion wavelength (λ_0) [66]. In fact, expanding the linear mismatch as a function of wavelength around λ_0, we find that:

$$\Delta\beta = -\frac{(2\pi c)^3}{\lambda_p^4} \beta_3 (\lambda_p - \lambda_0)(\lambda_p - \lambda_s) \tag{2.71}$$

where β_3 is the third order dispersion term. The variations on λ_0 locally modify the phase matching conditions between pump, signal and idler and dramatically affect the properties of the parametric gain spectrum.

A localised analysis of the parametric gain along the optical fibre could, thus, reveal possible imperfections in the behaviour of the amplifier and, at the same time, provide useful informations on the longitudinal distribution of the zero-dispersion wavelength, as addressed in section 5.2.2.

Bibliography

[1] N. Bloembergen, *Nonlinear optics.* WA Benjamin, 1965.

[2] P. N. Butcher and D. Cotter, *The elements of nonlinear optics.* Cambridge University Press, 1990.

[3] G. Agrawal, *Nonlinear fiber optics.* Academic Press, second ed., 1995.

[4] R. W. Boyd, *Nonlinear Optics.* Academic Press, 1992.

[5] J. Subias, J. Pelayo, R. Alonso, F. Villuendas, and C. Heras, "Electrostriction-free n_2 measurement in single-mode optical fibers based on nonlinear-polarization evolution," *J. Opt. Soc. Am. B*, vol. 19, no. 3, pp. 390–394, 2002.

[6] J. D. Jackson, *Classical electrodynamics.* Wiley, NY, 1975.

[7] J. A. Buck, *Fundamentals of Optical Fibers.* Wiley-Interscience, 2nd ed., 1995.

[8] L. G. Cohen, W. L. Mammel, and S. J. Jang, "Low-loss quadruple-clad single-mode lightguides with dispersion below 2 ps/nm/km over the 1.28-1.65 μm wavelength range," *Electron. Lett.*, vol. 18, pp. 1023–1024, 1982.

[9] D. A. Kleinmann, "Nonlinear dielectric polarisation in optical media," *Phys. Rev.*, vol. 126, pp. 1977–1979, 1962.

[10] P. V. Mamyshev and S. V. Chernikov, "Ultrashort-pulse propagation in optical fibers," *Opt. Lett.*, vol. 15, no. 19, pp. 1076–1078, 1990.

[11] C. Flytzanis, *Quantum Electronics: A Treatise*, vol. 1A: Nonlinear Optics. Academic Press, New York, 1975.

[12] J. P. Gordon, "Theory of the soliton self-frequency shift," *Opt. Lett.*, vol. 11, no. 10, p. 662, 1986.

[13] G. B. Whitham, *Linear and nonlinear waves*. Wiley Interscience, NY, 1974.

[14] C. Sulem and P. L. Sulem, *The nonlinear Schrödinger equation: self focusing and wave collapse*. Applied mathematical science, Springer Verlag, New York, 1999.

[15] L. A. Ostrovskii, "Propagation of wave packets and space-time self-focusing in a nonlinear medium," *Sov. JETP Lett.*, vol. 24, p. 797, 1967.

[16] A. Hasegawa and F. Tappert, "Transmission of stationary nonlinear optical pulses in dispersive dielectric fibres. i. anomalous dispersion," *Appl. Phys. Lett.*, vol. 23, pp. 142–144, 1973.

[17] D. Anderson, "Variational approach to nonlinear pulse propagation in optical fibers," *Phys. Rev. A*, vol. 27, pp. 3135–3145, 1983.

[18] A. Newell and J. Maloney, *Nonlinear optics*. Addison-Wesley, 1992.

[19] V. E. Zacharov, "Stability of periodc waves of finite amplitude on the surface of a deep fluid," *Sov. Phy. J. Appl. Mech. Tech. Phys.*, vol. 4, p. 86, 1968.

[20] H. C. Yuen and W. E. Ferguson Jr, "Relationship between Benjamin-Feir instability and recurrence in the

nonlinear Schrödinger equation," *Phys. Fluids*, vol. 21, pp. 1275–1278, August 1978.

[21] H. C. Yuen and B. M. Lake, "Nonlinear dynamics of deep water gravity waves," *Adv. Appl. Mech.*, vol. 22, pp. 67–229, 1982.

[22] N. N. Bogolyubov *Izv. Akad. Nauk SSSR (Proceedings of Academy of Sciences of USSR), Ser. Fiz.*, vol. 11, p. 77, 1947.

[23] Y. S. Kivshar and M. Peyrard, "Modulational instabilities in discrete lattices," *Phys. Review A*, vol. 46, no. 6, pp. 3198–3205, 1992.

[24] A. Hasegawa, "Theory and computer experiment on self-trapping instability of plasma cyclotron waves," *Phys. Fluids*, vol. 15, no. 5, pp. 870–881, 1972.

[25] A. Hasegawa, *Plasma instabilities and nonlinear effects*. Springer Verlag, Heidelberg, 1975.

[26] R. P. Sharma, K. Batra, and A. D. Verga, "Nonlinear evolution of the modulational instability and chaos using one-dimensional Zakharov equations and a simplified model," *Phys. Plasmas*, vol. 12, p. 022311(7), 2005.

[27] M. Ablowitz and H. Segur, *Solitons and the inverse scattering transform*. SIAM, Philadelphia, 1981.

[28] V. Y. Belashov and S. V. Vladimirov, *Solitary Waves in Dispersive Complex Media*. Springer Verlag, Berlin, Heidelberg, NY, 2005.

[29] T. B. Benjamin and J. Feir, "The disintegration of wave trains on deep water," *J. Fluid Mech.*, vol. 27, no. 3, pp. 417–430, 1967.

[30] V. I. Bespalov and V. I. Talanov *Sov. Phys. JETP Lett.*, vol. 3, p. 307, 1966.

[31] T. Taniuti and H. Washimi, "Self-trapping and instability of hydromagnetic waves along the magnetic field in a cold plasma," *Phys. Rev. Lett.*, vol. 21, pp. 209–212, 1968.

[32] K. Tai, A. Hasegawa, and A. Tomita, "Observation of modulational instability in optical fibers," *Phys. Rev. Lett.*, vol. 56, pp. 135–138, January 1986.

[33] K. Tai, A. Tomita, J. L. Jewell, and A. Hasegawa, "Generation of subpicosecond solitonlike optical pulses at 0.3 THz repetition rate by induced modulational instability," *Appl. Phys. Lett.*, vol. 49, no. 5, pp. 236–238, 1986.

[34] M. González-Herráez, S. Martín-López, P. Corredera, M. L. Hernanz, and P. R. Horche, "Supercontinuum generation using a continuous-wave Raman fiber laser," *Opt. Commun.*, vol. 226, pp. 323–328, 2003.

[35] E. Fermi, J. Pasta, and H. C. Ulam, "Studies of nonlinear problems I," *Collected papers of Enrico Fermi*, vol. edited by E. Segrè (Univ. Chicago Press), Vol. 2, p. 977, 1965.

[36] D. K. Campbell, P. Rosenau, and G. Zaslavsky, "Introduction: The Fermi-Pasta-Ulam problem. The first fifty years," *Chaos*, vol. 15, p. 015101, 2005.

[37] G. P. Berman and F. M. Izrailev, "The Fermi-Pasta-Ulam problem. Fifty years of progress," *Chaos*, vol. 15, p. 015104, 2005.

[38] T. Dauxois, M. Peyrard, and S. Ruffo, "The Fermi-Pasta-Ulam "numerical experiment": history and pedagogical perspectives," *Eur. J. Phys.*, vol. 26, pp. S3–S11, 2005.

[39] N. J. Zabusky and M. D. Kruskal, "Interaction of "solitons" in a collisionless plasma and the recurrence of initial states," *Phys. Rev. Lett.*, vol. 15, pp. 240–243, August 1965.

[40] F. D. Tappert and C. N. Judice, "Recurrence of nonlinear ion acoustic waves," *Phys. Rev. Lett.*, vol. 29, pp. 1308–1311, november 1972.

[41] B. M. Lake, H. C. Yuen, H. Rungaldier, and W. E. Ferguson, "Nonlinear deep-water waves: theory and experiment. Part 2. Evolution of a continous wave train ," *J. Fluid Mech.*, vol. 83, no. 1, pp. 49–74, 1977.

[42] K. Longrenn, *Solitons in action.* Academic, NY, 1978.

[43] P. A. E. M. Janssen, "Modulational instability and the Fermi-Pasta-Ulam recurrence," *Phys. Fluids*, vol. 24, no. 1, pp. 23–26, 1981.

[44] A. Berezine, "Can an electromagnetic field exist in a form of Fermi-Pasta-Ulam recurrence?," *J. Phys. D: Appl. Phys.*, vol. 22, pp. 577–583, 1989.

[45] N. N. Akhmediev, D. R. Heatley, G. I. Stegeman, and E. M. Wright, "Pseudorecurrence in the two-

dimensional modulation instability with a saturable self-focusing nonlinearity," *Phys. Rev. Lett.*, vol. 65, pp. 1423–1426, September 1990.

[46] V. M. Burlakov, S. A. Darmanyan, and V. N. Pyrkov, "Modulation instability and recurrence phenomena in anharmonic lattices," *Phys. Review B*, vol. 54, no. 5, pp. 3257–3265, 1996.

[47] G. Simaeys Van, P. Emplit, and M. Haelterman, "Experimental demonstration of the Fermi-Pasta-Ulam recurrence in a modulationally unstable optical wave," *Phys. Rev. Lett.*, vol. 87, p. 33902(4), July 2001.

[48] G. Simaeys Van, P. Emplit, and M. Haelterman, "Experimental study of the reversible behaviour of modulational instability in optical fibers," *J. Opt. Soc. Am. B*, vol. 19, pp. 477–486, March 2002.

[49] E. Infeld, "Quantitative theory of the Fermi-Pasta-Ulam recurrence in the nonlinear Schrödinger equation," *Phys. Rev. Lett.*, vol. 47, pp. 717–718, September 1981.

[50] P. Henrotay, "Periodic solutions and recurrence for linear Schrödinger equation: a Fourier-mode approach," *Journal de mécanique*, vol. 20, no. 1, pp. 159–168, 1981.

[51] G. Cappellini and S. Trillo, "Third-order three-wave mixing in single-mode fibres: exact solutions and spatial instability," *J. Opt. Soc. Am. B*, vol. 8, pp. 824–838, April 1991.

[52] S. Trillo and S. Wabnitz, "Dynamics of the nonlinear modulational instability in optical fibers," *Opt. Lett.*, vol. 16, pp. 986–988, July 0991.

[53] N. N. Akhmediev and V. I. Korneev, "Modulation instability and periodic solutions of the nonlinear Schrödinger equation," *Theor. Math. Phys. (U.S.S.R)*, vol. 69, pp. 1089–1092, 1986.

[54] N. Akhmediev and A. Ankiewicz, "First-order exact solutions of the nonlinear Schrödinger equation in the normal-dispersion regime," *Phys. Review A*, vol. 47, pp. 3213–3221, April 1993.

[55] D. Mihalache and N. C. Panoiu, "Analytic method for solving the nonlinear Schrödinger equation describing pulse propagation in dispersive optic fibres," *J. Phys. A: Math Gen.*, vol. 26, pp. 2679–2697, 1993.

[56] M. Karlsson, "Modulational instability in lossy optical fibres," *J. Opt. Soc. Am. B*, vol. 12, no. 11, pp. 2071–2077, 1995.

[57] A. Hasegawa and K. Tai, "Effects of modulational instability on coherent transmission systems," *Opt. Lett.*, vol. 14, no. 10, pp. 512–514, 1989.

[58] W. Krolikowski, O. Bang, J. J. Rasmussen, and J. Wyller, "Modulational instability in nonlocal nonlinear kerr media," *Phys. Review E*, vol. 64, no. 1, p. 016612, 2001.

[59] J. Wyller, W. Krolikowski, O. Bang, and J. J. Rasmussen, "Generic features of modulational instability in nonlocal Kerr media," *Phys. Review E*, vol. 66, no. 6, p. 066615, 2002.

[60] V. K. Zacharov and A. B. Shabat *Sov. Phys. J.E.T.P.*, vol. 34, pp. 62–69, 1972.

[61] D. Cotter, "Suppression of stimulated Brillouin scattering during transmission of high power narrowband laser light in monomode fibre," *Electron. Lett.*, vol. 18, pp. 638–640, 1982.

[62] K. Hill, D. Johnson, B. Kawasaki, and R. MacDonald, "CW three wave mixing in single-mode optical fibers," *J. Appl. Phys.*, vol. 49, pp. 5098–5106, 1978.

[63] R. H. Stolen and J. E. Bjorkholm, "Parametric amplification and frequency conversion in optical fibers," *IEEE J. Quantum Electron.*, vol. QE-18, pp. 1062–1072, 1982.

[64] K. Inoue, "Four-wave mixing in an optical fiber in the zero-dispersion wavelength region," *J. Lightwave Technol.*, vol. 10, pp. 1553–1562, 1992.

[65] J. Hansryd, P. Andrekson, M. Westlund, J. Li, and P.-O. Hedekvist, "Fiber-based optical parametric amplifiers and their applications," *IEEE JSTQE*, vol. 8, no. 3, pp. 506–520, 2002.

[66] A. Mussot, E. Lantz, A. Durecu-Legrand, C. Simonneau, D. Bayart, T. Sylvestre, and H. Maillotte, "Zero-dispersion wavelength mapping in short single-mode optical fibers using parametric amplification," *IEEE Photon. Tech. Lett.*, vol. 18, no. 1, pp. 22–24, 2006.

Chapter 3

Brillouin Scattering

...mes premiers raisonnements étaient assez complexes et ne laissaient pas apparaître le sens physique des calculs...

Léon Brillouin, 1931

3.1 Linear scattering

3.1.1 Generalities

Scattering is a general physical process whereby some form of radiation, such as light, sound, or moving particles, is forced to deviate from a straight trajectory by one or more localised non-uniformities in the medium through which it passes.

Light scattering specifically occurs as a consequence of fluctuations in the optical properties of a material medium: a completely homogeneous material can actually scatter light only in the forward direction [1, 2]. When the optical power is such that the optical properties of the system are unmodified by the presence of the incident light beam, we refer to the scattering process as *spontaneous* or *linear*. Additionally, if the

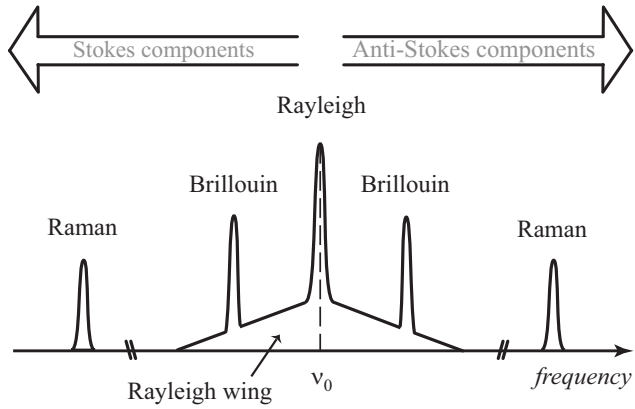

Figure 3.1: Spontaneous scattering. Typical spectral components of the observed spectrum in an inhomogeneous medium.

energy of the scattered photons is conserved, and hence there is no frequency shift induced by the process, the scattering is considered to be *elastic*, whereas if an energy exchange occurs within the medium during the process, the scattered photons undergo a frequency shift and the scattering is considered to be *inelastic*.[1]

Under the most general circumstances, the spectrum of the scattered light has the form shown in figure 3.1, in which Raman, Brillouin, Rayleigh and Rayleigh-wing features are present. By definition, the components that are shifted to lower frequencies are known as *Stokes* components, whereas the components that are shifted to higher frequencies are known as *anti-Stokes* components. The different features in the scattered spectrum are generated by different processes, depending

[1]These terminology derives from the kinetic theory of the collision of solid bodies, which can often be used to model scattering processes.

on the particular type of interaction between the radiation and the matter.

Rayleigh scattering is an elastic process originating from non propagating density fluctuations. Formally, it can be described as the scattering from fluctuations of the medium entropy (i.e., variations of the degree of molecular organization state).

Rayleigh-wing scattering is an elastic scattering resulting from fluctuations in the orientation of anisotropic molecules. Since the molecular reorientation process is very rapid, the corresponding peak has a very large spectral width. A rigorous physical description is quite complex and can be found in [1,3].

Brillouin scattering is an inelastic process generated by travelling density perturbations, associated to pressure variations in the medium [4]. Formally, it can be considered as the result of the interaction of photons with acoustic phonons. The relatively low frequencies of these modes induce a limited frequency shift, in the 10^{10} Hz region.

Raman scattering is a highly inelastic process originating from the interaction of light with high-frequency vibrational modes of the molecules of the medium. Formally, it results from the the interaction between photons and optical phonons of the structure. This yields frequency shifts in the 10^{14} Hz region, namely three orders of magnitude greater than for Brillouin shifts. Further details can be found in [2].

The propagation of optical waves in an optical material is governed by the following equation (see section 2.2):

$$\nabla^2\mathbf{E}(\mathbf{r},t) - \frac{1}{c^2}\frac{\partial^2\mathbf{E}(\mathbf{r},t)}{\partial t^2} = \mu_0\frac{\partial^2\mathbf{P}(\mathbf{r},t)}{\partial t^2} \tag{3.1}$$

where, for an homogeneous and isotropic medium, the polarisation vector is related to the electric field through the dielec-

tric susceptibility of the medium, $\mathbf{P} = \epsilon_0 \chi \mathbf{E}$. Nevertheless, a real medium is generally inhomogeneous and anisotropic; since light scattering originates from fluctuations in the optical properties of the medium, the dielectric susceptibility can be conveniently represented as follows [5]:

$$\boldsymbol{\chi}(\mathbf{r}, t) = \chi \mathbf{I} + \boldsymbol{\Delta\chi}(\mathbf{r}, t) \tag{3.2}$$

where χ and $\mathbf{I}$ are respectively the mean dielectric susceptibility of the medium and the identity tensor, and where $\boldsymbol{\Delta\chi}(r, t)$ represents the fluctuations in the dielectric susceptibility tensor leading to light scattering. Due to this change in the susceptibility, the material develops an additional polarisation:

$$\begin{aligned} \mathbf{P}(\mathbf{r}, t) &= \epsilon_0 \chi \mathbf{E}(\mathbf{r}, t) + \epsilon_0 \boldsymbol{\Delta\chi}(\mathbf{r}, t) \otimes \mathbf{E}(\mathbf{r}, t) \\ &= \epsilon_0 \chi \mathbf{E}(\mathbf{r}, t) + \boldsymbol{\Delta\epsilon}(\mathbf{r}, t) \otimes \mathbf{E}(\mathbf{r}, t) \end{aligned} \tag{3.3}$$

where the second term is usually referred to as the *induced electronic polarisation.*

Introducing (3.3) in (3.1) and using the fact that $n = \sqrt{1 + \chi}$ (see section 2.2.1), we easily obtain:

$$\nabla^2 \mathbf{E}(\mathbf{r}, t) - \frac{n^2}{c^2} \frac{\partial^2 \mathbf{E}(\mathbf{r}, t)}{\partial t^2} = \mu_0 \frac{\partial^2}{\partial t^2} (\boldsymbol{\Delta\epsilon} \otimes \mathbf{E}) \tag{3.4}$$

where the right-hand side acts as a source for the generation of scattering processes.

The fluctuations in the dielectric tensor can be decomposed into the sum of a scalar contribution and a traceless tensor as follows:

$$\boldsymbol{\Delta\epsilon}(\mathbf{r}, t) = \Delta\epsilon(\mathbf{r}, t)\mathbf{I} + \boldsymbol{\Delta\epsilon}^t(\mathbf{r}, t) \tag{3.5}$$

The diagonal scalar term $\Delta\epsilon$ arises from fluctuations in thermodynamic quantities like density, temperature, entropy or

pressure and is responsible for Brillouin and Rayleigh scatterings [6]. The purely out-of-diagonal terms $\boldsymbol{\Delta\epsilon}^t$ can in turn be decomposed into the sum of a symmetric ($\boldsymbol{\Delta\epsilon}^s$) and an anti-symmetric ($\boldsymbol{\Delta\epsilon}^a$) contribution, both statistically independent and intrinsically related to the optical polarisability of the medium [3]. The symmetric part is responsible for Rayleigh-wing scattering, whereas the anti-symmetric part gives rise to Raman scattering.

In this section we focus our attention to the processes based on static and propagating density fluctuations.

3.1.2 Rayleigh scattering

The fluctuations in the scalar dielectric constant can be related to the fluctuations in thermodynamic variables, such as the material density (ρ) and temperature (T), by the following relation:

$$\Delta\epsilon = \left.\frac{\partial\epsilon}{\partial\rho}\right|_T \Delta\rho + \left.\frac{\partial\epsilon}{\partial T}\right|_\rho \Delta T \tag{3.6}$$

To good accuracy, the second term can usually be ignored (the error is estimated to be of the order of 2%), since the dielectric constant typically depends more on density than on temperature [1]. We can thus rewrite (3.6) as:

$$\Delta\epsilon = \frac{\gamma_e}{\rho_0}\Delta\rho \tag{3.7}$$

where ρ_0 denotes the mean density of the material and where we have introduced the electrostrictive constant [7]:

$$\gamma_e = \rho_0 \left.\frac{\partial\epsilon}{\partial\rho}\right|_{\rho=\rho_0} \tag{3.8}$$

The variations in density, $\Delta\rho$, can be expressed in terms of pressure p and entropy s, as follows:

$$\Delta\rho = \left.\frac{\partial\rho}{\partial p}\right|_s \Delta p + \left.\frac{\partial\rho}{\partial s}\right|_p \Delta s \tag{3.9}$$

The first term describes adiabatic density fluctuations (i.e., acoustic waves) and leads to Brillouin scattering. The second term corresponds to isobaric density fluctuations (i.e., temperature or entropy variations at constant pressure) and is responsible for Rayleigh scattering.

Entropy fluctuations can be described by a diffusion equation having the following form:

$$\rho c_p \frac{\partial \Delta s}{\partial t} - \kappa \nabla^2 \Delta s = 0 \tag{3.10}$$

where c_p denotes the specific heat at constant pressure and κ the thermal conductivity. A general solution of (3.10) is:

$$\Delta s(\mathbf{r}, t) = \Delta s_0 e^{-\delta t} e^{-i\mathbf{q}\cdot\mathbf{r}} \tag{3.11}$$

where the damping rate of the entropy disturbance is given by $\delta = \kappa q^2/\rho c_p$. It is easy to see that these entropy waves do not propagate; as a result the term of the induced polarisation proportional to Δs gives rise only to unshifted components of the scattered light.

3.1.3 Spontaneous Brillouin scattering

The propagation of pressure fluctuations, Δp, through the medium is governed by the following equation [1, 2]:

$$\frac{\partial^2 \Delta p}{\partial t^2} - \Gamma \nabla^2 \frac{\partial \Delta p}{\partial t} - v_a^2 \nabla^2 \Delta p = 0 \tag{3.12}$$

where v_a is the velocity of sound in the medium.[2] It can be conveniently expressed in terms of thermodynamic variables as follows:

$$v_a = \sqrt{\left.\frac{\partial p}{\partial \rho}\right|_s} = \sqrt{\frac{K}{\rho}} = \sqrt{\frac{1}{\rho C_s}} \tag{3.13}$$

where K is the bulk modulus and C_s is the adiabatic compressibility. The coefficient Γ is an acoustic damping parameter, related to the shear (η_s) and bulk (η_b) viscosity coefficients of the material: $\Gamma = (4/3\eta_s + \eta_b)/\rho_0$.

Equation (3.12) admits a general solution of the form:

$$\Delta p(\mathbf{r}, t) = \frac{1}{2}\Delta p_0 \, \Re\left[e^{i(\mathbf{q}\cdot\mathbf{r} - \Omega t)}\right] \tag{3.14}$$

where $\mathbf{q}$ and Ω must satisfy the phonon dispersion relation [10], $\Omega = v_a|\mathbf{q}|$. By assuming that the incident optical field is monochromatic

$$E(\mathbf{r}, t) = \frac{1}{2}E_0 \, \Re\left[e^{i(\mathbf{k}\cdot\mathbf{r} - \omega t)}\right] \tag{3.15}$$

and by inserting into (3.4) the term of the induced polarisation proportional to Δp, the scattered field must obey the following wave equation:

$$\nabla^2\mathbf{E} - \frac{n^2}{c^2}\frac{\partial^2\mathbf{E}}{\partial t^2} = -\frac{1}{2}\frac{\gamma_e C_s}{c^2}\,\Re\Big[(\omega-\Omega)^2 e^{i(\mathbf{k}-\mathbf{q})\mathbf{r} - i(\omega-\Omega)t} + (\omega+\Omega)^2 e^{i(\mathbf{k}+\mathbf{q})\mathbf{r} - i(\omega+\Omega)t}\Big] \tag{3.16}$$

[2] This equation, which is well known in the field of acoustics, can be easily derived from the Navier-Stokes equations for the case of a viscous and compressible fluid [8, 9].

The first term in the left-hand side is an oscillating component with wave vector $\mathbf{k}' = \mathbf{k} - \mathbf{q}$ and frequency $\omega' = \omega - \Omega$, and leads to Stokes scattering. The wave vectors and the frequencies of the three interacting waves are related by the dispersion relations $\omega = |\mathbf{k}|c/n$, $\omega' = |\mathbf{k}'|c/n$, $\Omega = |\mathbf{q}|v_a$, and have definite values that depend on the scattering direction considered, as illustrated in figure 3.2. The frequency of the acoustic wave (Ω) being much smaller than the optical frequencies involved (ω,ω'), we have that $|\mathbf{k}| \approx |\mathbf{k}'|$. The analysis of the figure easily shows that $|\mathbf{q}| = 2|\mathbf{k}| \sin(\theta/2)$, which brings to the final expression:

$$\Omega = 2n\omega \frac{v_a}{c} \sin(\theta/2) \tag{3.17}$$

We note that the frequency shift is equal to zero for forward scattering, and is maximum for backscattering ($\theta = \pi$). In this case of particular interest for optical fibres, the shift reads: $\Omega = 2n\omega v_a/c$. From a quantum point of view, the absorption of an incident photon is followed by the emission of a phonon and of a new photon at a lower frequency.

In an analogous way, the second term in (3.16) is an oscillating component with wave vector $\mathbf{k}' = \mathbf{k} + \mathbf{q}$ and frequency $\omega' = \omega + \Omega$, and leads to anti-Stokes scattering (see figure 3.3). From a quantum point of view, the absorption of an incident photon and of a phonon is followed by the emission of a new photon at a higher frequency.

If we include in the analysis the attenuation of the acoustic wave through the damping parameter Γ, we find that the light scattered into direction θ is not monochromatic, but exhibits a frequency broadening whose width is given by:

$$\delta\omega = \Gamma|\mathbf{q}|^2 = 4n^2\Gamma\frac{\omega^2}{c^2} \sin^2(\theta/2) \tag{3.18}$$

This is due to the fact that the acoustic waves propagate only

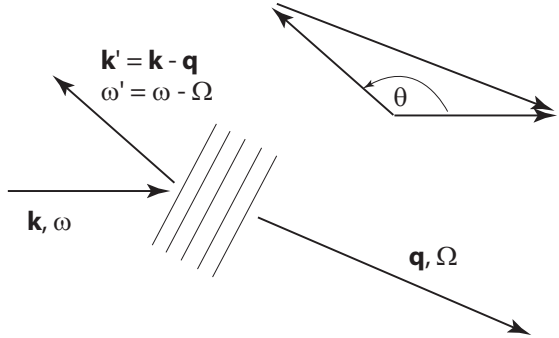

Figure 3.2: Illustration of Stokes scattering

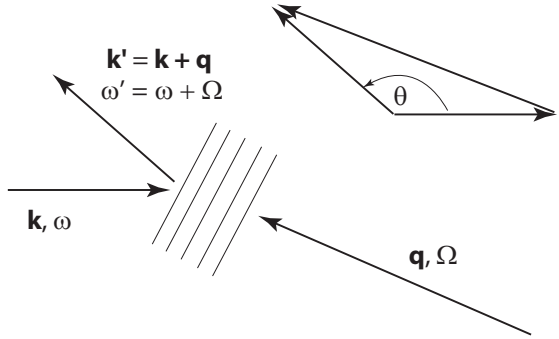

Figure 3.3: Illustration of anti-Stokes scattering

Wavelength (nm)	Brillouin shift (GHz)	Brillouin linewidth (MHz)
514	34	100
832	21.6	70
1320	12.8	35
1550	10.8	29

Table 3.1: Characteristics of the Brillouin spectrum in optical fibres at different operating wavelengths. The acoustic velocity in silica is approximately equal to 5775 m/s.

over a few optical wavelengths (just few micrometres) and that, consequently, the intensity of the acoustic wave undergoes an exponential decrease:

$$|\Delta p(t)|^2 = |\Delta p(0)|^2 e^{-t/\tau_p} \tag{3.19}$$

where $\tau_p = 1/(\Gamma|\mathbf{q}|^2)$ represents the average lifetime of the acoustic phonons in the medium and is inversely proportional to the acoustic damping coefficient. In the Fourier domain, the backscattered spectrum of the exponential damping has a Lorentzian shape with a full width at maximum half (FWMH) equal to:

$$\frac{\delta\omega}{2\pi} = \frac{1}{\pi\tau_p} \tag{3.20}$$

Table 3.1 summarises some typical values of the characteristics of the Brillouin spectrum in standard single-mode silica optical fibres at different operating wavelengths.

3.2 Stimulated Brillouin scattering

We dealt, in the previous section, with spontaneous scattering which is a linear effect occurring as the result of thermal fluctuations in the density. In contrast, when the fluctuations within the medium are induced by the presence of the optical field the scattering process becomes a nonlinear effect and is referred to as *stimulated*.

Stimulated Brillouin scattering (SBS) in optical fibres can be described as a three-wave interaction between a pump wave, an optically induced acoustic wave, and the scattered light in the form of a counterpropagating Stokes wave. The diagram of the three wavevectors is schematically reported in figure 3.4. Actually, the pump light is scattered by the refractive index variations associated to the sound wave via Bragg diffraction; the pump and the scattered signal interact then to produce a moving interference pattern, which reinforces the acoustic wave, and the process continues.

The physical mechanism by which the interference between the pump and the Stokes wave can drive an acoustic wave is electrostriction.

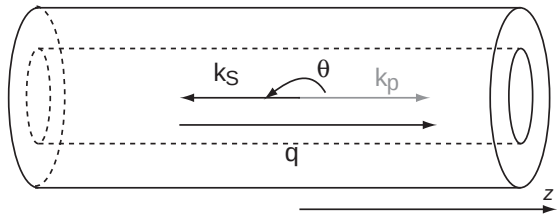

Figure 3.4: Geometry of Brillouin scattering in optical fibres. k_p: forward propagating pump wave; k_S: backscattered Stokes wave; q: acoustic wave.

3.2.1 Electrostriction

Electrostriction is the tendency of many materials (silica is one of them) to become compressed in the presence of an electric field. This process may be viewed as a consequence of the maximisation of potential energy, the molecules being attracted towards the regions of high optical intensity in order to increase the stored energy.

From a microscopical point of view, the electrostrictive force acting on the dielectric material can be derived in terms of the dipole moment acting on an individual molecule placed in the fringing field of a capacitor [2]. Nonetheless, we have opted here for a more global point of view and we derive the electrostrictive force on the basis of energy considerations [11].

We consider a volume V of a dielectric material, globally unperturbed and located in a quasi-stationary electric field $\mathbf{E}(\mathbf{r})$. We admit, moreover, that the surface S, boundary of V, stay unchanged and that the response of the material is instantaneous. Under these conditions, the electric energy contained in the volume V is given by:

$$W(t) = \frac{1}{2}\iiint_V \mathbf{D}^*(\mathbf{r},t)\mathbf{E}(\mathbf{r})\,dV = \frac{1}{2}\iiint_V \epsilon(\mathbf{r},t)|\mathbf{E}(\mathbf{r})|^2\,dV \tag{3.21}$$

where $\epsilon(\mathbf{r},t) = \epsilon_0(1+\chi(\mathbf{r},t))$. As a result of electrostriction, the local changes in density ($d\rho$) result in local changes in the dielectric constant ($d\epsilon$) by means of (3.7). Consequently the energy variations are accounted for by:

$$\frac{\partial W}{\partial t} = \frac{1}{2}\frac{\partial \epsilon}{\partial \rho}\iiint_V \frac{\partial \rho(\mathbf{r},t)}{\partial t}|\mathbf{E}(\mathbf{r})|^2\,dV \tag{3.22}$$

Expressing the conservation of matter in the form of the con-

tinuity equation

$$\frac{\partial \rho(\mathbf{r},t)}{\partial t} = -\nabla(\rho(\mathbf{r},t)\mathbf{v}) \tag{3.23}$$

where $\mathbf{v} = \mathbf{v}(\mathbf{r},t)$ is the velocity of the matter displacements, we obtain:

$$\begin{aligned}\frac{\partial W}{\partial t} &= \frac{1}{2}\frac{\partial \epsilon}{\partial \rho}\iiint_V |\mathbf{E}(\mathbf{r})|^2 \nabla\left(\rho(\mathbf{r})\mathbf{v}\right)\, dV \\ &= -\frac{1}{2}\frac{\partial \epsilon}{\partial \rho}\iiint_V \left[\nabla(\rho(\mathbf{r})|\mathbf{E}(\mathbf{r})|^2\mathbf{v}) - \rho(\mathbf{r})\mathbf{v}\nabla|\mathbf{E}(\mathbf{r})|^2\right] dV\end{aligned} \tag{3.24}$$

The first term in the previous integral is vanishing: applying the divergence theorem and using the fact that the boundary S is supposed to stay unchanged, we easily find that

$$\iiint_V \nabla(\rho(\mathbf{r})|\mathbf{E}(\mathbf{r})|^2\mathbf{v})\, dV = \oint_S \rho(\mathbf{r})|\mathbf{E}(\mathbf{r})|^2\mathbf{v}\, d\mathbf{S} = 0 \tag{3.25}$$

and thus obtain the final expression for the electric power dissipated within the dielectric medium:

$$\frac{\partial W}{\partial t} = \frac{1}{2}\frac{\partial \epsilon}{\partial \rho}\iiint_V \left[\rho(\mathbf{r})\mathbf{v}\nabla|\mathbf{E}(\mathbf{r})|^2\right]\, dV \tag{3.26}$$

On the other hand, the total work dW of the external forces within the volume V during the time interval dt can be written as [12]:

$$\frac{dW}{dt} = \iiint_V \mathbf{f}\cdot\mathbf{v}\, dV \tag{3.27}$$

where $\mathbf{f}$ represents the force density per unit volume. Comparing the expression for the mechanical power transferred to

the material (3.27) and the expression for the electrical power dissipated through electrostriction (3.26), we eventually find:[3]

$$\mathbf{f}(\mathbf{r}) = \frac{1}{2}\rho\frac{\partial\epsilon}{\partial\rho}\nabla|\mathbf{E}(\mathbf{r})|^2 = \frac{1}{2}\gamma_e\nabla|\mathbf{E}(\mathbf{r})|^2 \tag{3.28}$$

where $\mathbf{f}$ represents the electrostrictive force per unit volume, and γ_e is the electrostrictive constant previously defined in (3.8).

Since the molecular mass displacement is an inherently slow effect, the material is characterised by a reaction time much higher than the period of the incident optical waves. For this reason, in the above formulation the intensity of the electric field should be replaced by its time-average over several optical periods:

$$\mathbf{f}(\mathbf{r}) = \frac{1}{2}\gamma_e\nabla\left\langle|\mathbf{E}(\mathbf{r})|^2\right\rangle \tag{3.29}$$

As a consequence, only the low frequency components of the optical intensity (associated for example to the envelope of the interference pattern between two optical waves) would give rise to an electrostrictive pressure within the medium, as depicted in figure 3.5.

As we will show in the next section, the electrostrictive force defined by (3.29) actually behaves as a source term in the equation describing the evolution of the material density, thus making the nonlinear coupling between the acoustic and the optical waves.[4]

[3] In the derivation of this expression we have implicitly assumed that the electrostriction is the only force at the origin of the compression (adiabaticity condition).

[4] One must not forget that the electrostrictive effect is also an important component of the Kerr effect, and contributes to the nonlinear refractive index, n_2, as well [13].

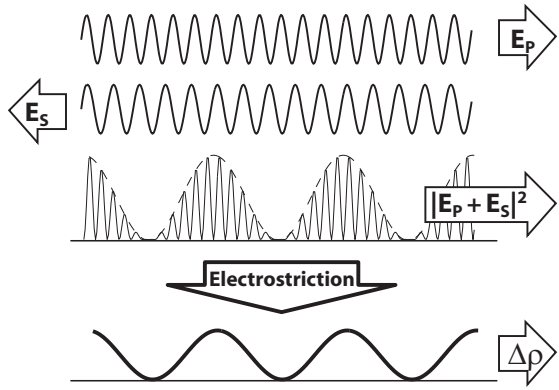

Figure 3.5: Generation of a pressure wave by means of electrostriction. The density variations of the medium are induced by the envelope of the interference between the two optical waves (counterpropagating as for SBS in optical fibres).

3.2.2 Classical theory

The process of SBS acts classically as a nonlinear interaction between a pump lightwave and a Stokes lightwave (respectively at frequencies ν_p and $\nu_S < \nu_p$), by means of a sound wave.

For an incident pump of sufficient intensity, the spontaneously scattered light can become quite intense. The beat field resulting from the interference of the two optical waves generates an acoustic wave (at frequency ν_B) through electrostriction. The incident pump is then scattered off the refractive index variation engendered by the density variations, and the scattered light (downshifted in frequency by an amount ν_B) adds constructively with the Stokes radiation that induced the acoustic disturbance. The process repeats again and, as a result, the acoustic and Stokes waves reinforce each other leading to the amplification of the Stokes wave. The physical

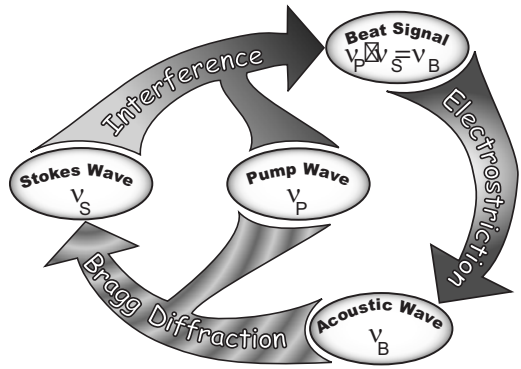

Figure 3.6: Graphical representation of the processes involved in the SBS process. From [14].

process is referred to as stimulated Brillouin scattering and can be schematically illustrated by the feedback loop of figure 3.6.

The propagation of the three involved waves is described by the following equations:

$$\nabla^2 \mathbf{E}_p - \frac{n^2}{c^2}\frac{\partial^2 \mathbf{E}_p}{\partial t^2} = \mu_0 \frac{\partial^2 \mathbf{P}_p^{NL}}{\partial t^2} \tag{3.30a}$$

$$\nabla^2 \mathbf{E}_S - \frac{n^2}{c^2}\frac{\partial^2 \mathbf{E}_S}{\partial t^2} = \mu_0 \frac{\partial^2 \mathbf{P}_S^{NL}}{\partial t^2} \tag{3.30b}$$

$$\frac{\partial^2 \Delta\rho}{\partial t^2} - \Gamma\nabla^2 \frac{\partial \Delta\rho}{\partial t} - v_a^2 \nabla^2 \Delta\rho = -\nabla \mathbf{f} \tag{3.30c}$$

where $\mathbf{E}_p$ and $\mathbf{E}_S$ are respectively the pump and the Stokes waves, and $\Delta\rho$ is the density variation which has been chosen instead of pressure to describe the acoustic wave. The equations (3.30) are coupled together through the driving terms in the right-hand side, given by the following constitutive rela-

tions:

$$\mathbf{P}_{p,S}^{NL}(\mathbf{r},t) = \Delta\epsilon\mathbf{E}_{p,S}(\mathbf{r},t) = \frac{\gamma_e}{\rho_0}\Delta\rho(\mathbf{r},t)\mathbf{E}_{p,S}(\mathbf{r},t) \tag{3.31a}$$

$$\nabla\mathbf{f}(\mathbf{r},t) = \frac{1}{2}\gamma_e\nabla^2\left\langle|\mathbf{E}_p(\mathbf{r},t) + \mathbf{E}_S(\mathbf{r},t)|^2\right\rangle \tag{3.31b}$$

We focus essentially on the properties of Stokes scattering - the mathematical description of anti-Stokes scattering being similar, except only a sign change in the definition of the Brillouin gain - and we assume that the waves are quasi-monochromatic so that the slowly-varying envelope approximation (SVEA) can be applied:

$$\mathbf{E}_p = \mathbf{e}_p\,\frac{1}{2}\Re\left[E_p\left(z,t\right)\,e^{i(\omega_p t - k_p z)}\right] \tag{3.32a}$$

$$\mathbf{E}_S = \mathbf{e}_S\,\frac{1}{2}\Re\left[E_S\left(z,t\right)\,e^{i(\omega_S t + k_S z)}\right] \tag{3.32b}$$

$$\Delta\rho = \quad\frac{1}{2}\Re\left[A\left(z,t\right)\,e^{i(\Omega t - qz)}\right] \tag{3.32c}$$

where $\mathbf{e}_p$ and $\mathbf{e}_S$ are the unit polarisation vectors for the pump and the Stokes waves.

By substituting the equations (3.32) in the source terms (3.31), and by retaining only the resonant terms for each wave, we obtain:

$$\mathbf{P}_p^{NL} = \mathbf{e}_p\frac{1}{2}\frac{\gamma_e}{\rho_0}\,\Re\left[A\left(z,t\right)E_S\left(z,t\right)e^{i(\omega_p t - k_p z)}\right] \tag{3.33a}$$

$$\mathbf{P}_S^{NL} = \mathbf{e}_S\frac{1}{2}\frac{\gamma_e}{\rho_0}\,\Re\left[A^*\left(z,t\right)E_p\left(z,t\right)e^{i(\omega_S t + k_S z)}\right] \tag{3.33b}$$

$$\nabla\mathbf{f} = \frac{1}{2}\gamma_e q^2\sqrt{\eta_P}\,\Re\left[E_p(z,t)E_S^*(z,t)e^{i(\Omega t - qz)}\right] \tag{3.33c}$$

where $\eta_P = |\mathbf{e}_p\cdot\mathbf{e}_S|^2$ represent the polarisation efficiency of the process. Substituting then (3.33) and (3.32) into (3.30) and

applying the SVEA, after some calculation we get the system of three coupled equations often referred to as *coherent model* of the SBS [9, 15, 16]:

$$\left[\frac{\partial}{\partial z} + \frac{n}{c}\frac{\partial}{\partial t} + \frac{\alpha}{2}\right] E_p = -\sqrt{\eta_P}\frac{ik_p\gamma_e}{4\varepsilon\rho_0} A E_S e^{i\Delta\omega t} \tag{3.34a}$$

$$\left[\frac{\partial}{\partial z} - \frac{n}{c}\frac{\partial}{\partial t} - \frac{\alpha}{2}\right] E_S = \sqrt{\eta_P}\frac{ik_S\gamma_e}{4\varepsilon\rho_0} A^* E_p e^{-i\Delta\omega t} \tag{3.34b}$$

$$\left[\frac{\partial}{\partial z} + \frac{2\Omega - j\Gamma q^2}{2\Omega v_a}\frac{\partial}{\partial t} + \frac{\Gamma q^2}{2v_a}\right] A = -\sqrt{\eta_P}\frac{iq\gamma_e}{4v_a^2} E_p E_S^* e^{-i\Delta\omega t} \tag{3.34c}$$

where the optical attenuation, α, and a possible frequency detuning from the resonance condition, $\Delta\omega = \omega_S + \Omega - \omega_p$, have been added phenomenologically.

Since the phonon propagation distance is typically small compared to the distance over which the optical waves vary significantly, the electric fields in (3.34c) can be considered as constants with respect to the spatial integration. Assuming steady-state conditions, the amplitude of the acoustic wave is then given by:

$$A(z,t) = -\frac{iq\gamma_e}{4\Gamma_B v_a}\sqrt{\eta_P} E_P(z,t) E_s^*(z,t) \frac{e^{-i\Delta\omega t}}{1 - i(2\Delta\nu/\Delta\nu_B)} \tag{3.35}$$

with $\Delta\nu_B = \Gamma_B/\pi$, where $\Gamma_B = \Gamma q^2/2$ denotes the Brillouin linewidth (cf. equation (3.18)). Substituting (3.35) into (3.34a) and (3.34b), and still assuming steady-state conditions, we get two coupled equations relating just the pump and the

Stokes waves:

$$\frac{\partial E_p}{\partial z} = -\eta_P \frac{q k_p \gamma_e^2}{16\epsilon\rho_0\Gamma_B v_a} \frac{E_p \left|E_S\right|^2}{1 - i\left(2\Delta\nu/\Delta\nu_B\right)} - \frac{\alpha}{2} E_p \tag{3.36a}$$

$$\frac{\partial E_S}{\partial z} = -\eta_P \frac{q k_S \gamma_e^2}{16\epsilon\rho_0\Gamma_B v_a} \frac{E_S \left|E_p\right|^2}{1 - i\left(2\Delta\nu/\Delta\nu_B\right)} + \frac{\alpha}{2} E_S \tag{3.36b}$$

The real part of the right hand members is responsible for the energy transfer between the optical waves, whereas the imaginary part is responsible for a propagation phase associated to the nonlinear interaction.

These equations can be transformed in a more easily handled system of coupled equations for the optical intensities of the fields through the transformation: $I_{p,S} = \frac{1}{2} n \epsilon_0 c |E_{p,S}|^2$. Substituting into (3.36), with proper manipulation we eventually obtain the *intensity model* of the SBS:

$$\frac{\partial I_p}{\partial z} = -\eta_P \, g_B\left(\nu\right) I_p \, I_S - \alpha I_p \tag{3.37a}$$

$$\frac{\partial I_S}{\partial z} = -\eta_P \, g_B\left(\nu\right) I_p \, I_S + \alpha I_S \tag{3.37b}$$

where $g_B(\nu)$ denotes the Brillouin gain spectrum defined as:

$$g_B\left(\nu\right) = g_B \frac{\left(\Delta\nu_B/2\right)^2}{(\nu - \nu_B)^2 + \left(\Delta\nu_B/2\right)^2} \tag{3.38}$$

g_B is the line-centre Brillouin gain factor and corresponds to a frequency detuning between the pump and the Stokes wave exactly equal to the Brillouin shift: $\nu_p - \nu_S = \nu_B = \Omega/2\pi$. It can be related to the constitutive parameters of the medium through the following relation:

$$g_B = 2 \frac{q k_S \gamma_e^2}{16\epsilon\rho_0\Gamma_B v_a} \frac{2}{n\epsilon_0 c} = \frac{2\pi \, n^7 p_{12}^2}{c \, \lambda_p^2 \rho_0 \, \Delta\nu_B \, v_a} \tag{3.39}$$

where λ_p denotes the pump wavelength and p_{12} is the longitudinal elasto-optic coefficient. In amorphous silica, the measured value of g_B is approximately equal to $5 \cdot 10^{-11}$ m/W.

From the equations (3.37), we clearly see that the nonlinear interaction between the two counterpropagating optical waves brings an energy transfer from the pump to the Stokes wave resulting in a net amplification for the Stokes signal, and that the gain spectrum follows a Lorentzian distribution, centred on ν_B, with FWHM equal to $\Delta\nu_B$ (see figure 3.7).[5] On the other hand, by expressing the electrical fields in the equations (3.36) in terms of their intensities and phases

$$E_{p,S}(z) = \sqrt{\frac{2}{n\epsilon_0 c} I_{p,S}(z)} e^{\mp i\phi_{p,S}^{SBS}(z)} \tag{3.40}$$

and by taking the imaginary part, we easily obtain the expression for the additional phase shifts due to the stimulated scattering process:

$$\frac{\partial\phi_p^{SBS}}{\partial z} = \frac{1}{2}\eta_P g_B I_S \frac{(2\Delta\nu/\Delta\nu_B)}{1+(2\Delta\nu/\Delta\nu_B)^2} \tag{3.41a}$$

$$\frac{\partial\phi_S^{SBS}}{\partial z} = \frac{1}{2}\eta_P g_B I_p \frac{(2\Delta\nu/\Delta\nu_B)}{1+(2\Delta\nu/\Delta\nu_B)^2} \tag{3.41b}$$

The nonlinear phase shifts have been defined such that a positive $\phi_{p,S}^{SBS}$ results in a supplementary positive delay. Conse-

[5] While in the spontaneous scattering Stokes and anti-Stokes components have comparable amplitudes (cf. figure 3.1), in the stimulated scattering the Stokes is dominant and the anti-Stokes vanishes. On account of energy and momentum conservation throughout the process (cf. section 3.1.3), Stokes scattering creates phonons, while anti-Stokes scattering annihilates them [17]. As the stimulated process starts, the anti-Stokes phonon population is rapidly depleted and the anti-Stokes scattering is significantly reduced. Eventually, when the full stimulated regime is reached, the anti-Stokes component totally disappears.

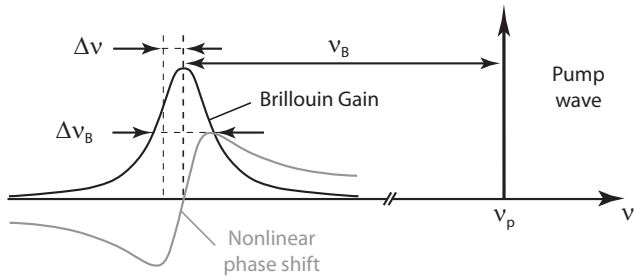

Figure 3.7: Representation of the Lorentzian shape of the Brillouin gain spectrum and of the associated nonlinear phase shift.

quently, equations (3.41) imply that both the optical waves are retarded when $\Delta\nu$ is positive and advanced when $\Delta\nu$ is negative. The Kramers-Krönig relations are then satisfied and it is possible to see in figure 3.7 the proportionality between the nonlinear shift and the derivative of the Brillouin gain curve. The phase characteristics of the SBS can be successfully utilised in fibres to optically control the group velocity of optical signals, as it has been recently demonstrated [18].

Stimulated anti-Stokes scattering

The mathematical development just presented for the Stokes scattering can be used as well to describe the propagation of a wave at the anti-Stokes frequency ($\nu_{AS} > \nu_p$). The interaction between the pump and a counterpropagating anti-Stokes wave can then be described by the following equations:

$$\frac{\partial I_p}{\partial z} = -\eta_P \, g_B(\nu) \, I_p \, I_{AS} - \alpha I_p \tag{3.42a}$$

$$\frac{\partial I_{AS}}{\partial z} = +\eta_P \, g_B(\nu) \, I_p \, I_{AS} + \alpha I_{AS} \tag{3.42b}$$

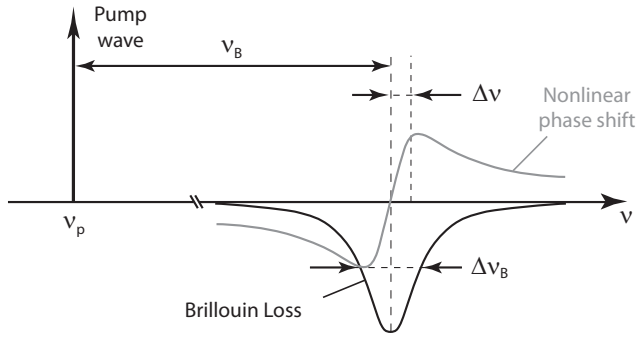

Figure 3.8: Representation of the Lorentzian shape of the Brillouin loss spectrum and of the associated nonlinear phase shift.

which are formally similar to equations (3.37). Nevertheless, while the minus sign in the first right-hand term of equation (3.37b) predicts an amplification of the Stokes signal, the plus sign in the first right-hand term of equation (3.42b) implies that the anti-Stokes signal undergoes an attenuation during the propagation (in the $-z$ direction) within the fibre.

The Brillouin loss spectrum still follows a Lorentzian distribution, centred on ν_B, with FWHM equal to $\Delta\nu_B$, as shown in figure 3.8.

3.2.3 Steady-state solutions

The equations (3.37), respectively (3.42), can not be solved in a close analytic form [19], except for the case of zero attenuation [20, 21]. By setting $\alpha = 0$ in the (3.37), we easily see that $\frac{\partial I_p}{\partial z} = \frac{\partial I_S}{\partial z}$, and hence we have:

$$I_p(z) = I_S(z) + C \tag{3.43}$$

where the value of the integration constant C depends on the boundary conditions. Using this result, the equation (3.37b) can be rewritten as:

$$\frac{\partial I_S}{\partial z} = -\eta_P g_B(\nu)(I_S(z) + C)I_S(z) \tag{3.44}$$

which admits a general solution of the form:

$$I_S(z) = \frac{KCe^{-\eta_P g_B(\nu)z}}{1 - KCe^{-\eta_P g_B(\nu)z}} \tag{3.45}$$

where the value of the integration constant K also depends on the boundary conditions.

Since the value of $I_p(z)$ is known at $z = 0$, the constant C can be conveniently expressed as follows: $C = I_p(0) - I_S(0)$. Substituting then into (3.45) for $z = 0$, we easily find that: $K = I_p(0)/I_S(0)$.

The spatial distributions of the pump and Stokes waves intensities are then fully described by the following equations:

$$I_p(z) = I_p(0)\frac{1 - r}{1 - re^{-\gamma z}} \tag{3.46a}$$

$$I_S(z) = I_p(0)\frac{r(1 - r)}{e^{\gamma z} - r} \tag{3.46b}$$

where $\gamma = \eta_P g_B(\nu) I_p(0)(1 - r)$ is often referred to as simple-pass gain and $r = I_p(0)/I_S(0)$.

Three different regimes can be distinguished, corresponding to three different physical situations: weak interaction regime, weak saturation regime and strong interaction regime [16].

Weak interaction regime

In the weak interaction regime, pump depletion can be neglected and, consequently, the probe is exponentially ampli-

fied. To the lowest order in r, the equations (3.46) can be approximated by:

$$I_p(z) = I_p(0) \tag{3.47a}$$

$$I_S(z) = rI_p(0)e^{-\eta_P g_B(\nu) I_p(0) z} \tag{3.47b}$$

These solutions are in agreement with the general solutions as far as $r < 10^{-4}$. Curves (i) on figures 3.9(a) and 3.9(b) show the evolution of $I_p(z)$ and $I_S(z)$ for $r = 10^{-5}$.

Weak saturation regime

The weak saturation regime is obtained for r in the range 10^{-3} to 10^{-2}. The pump is still undepleted, but the single-pass gain is now lower than in the case of weak interaction regime:

$$I_p(z) = I_p(0) \tag{3.48a}$$

$$I_S(z) = rI_p(0)e^{-\eta_P g_B(\nu) I_p(0)(1-r) z} \tag{3.48b}$$

Curves (ii) show the solutions for $r = 0.005$.

Strong saturation regime

The strong saturation regime is obtained for $r > 10^{-2}$. To take into account the pump depletion which is no more negligible in this situation, we can expand the equation (3.46a) to the first order in r, and neglecting the term in r^2, we obtain:

$$I_p(z) = I_p(0)[1 - r(1 - e^{-\eta_P g_B(\nu) I_p(0)(1-r) z})] \tag{3.49a}$$

$$I_S(z) = rI_p(0)e^{-\eta_P g_B(\nu) I_p(0)(1-r) z} \tag{3.49b}$$

Curves (iii) and (iv) show the solutions for $r = 0.01$ and $r = 0.5$.

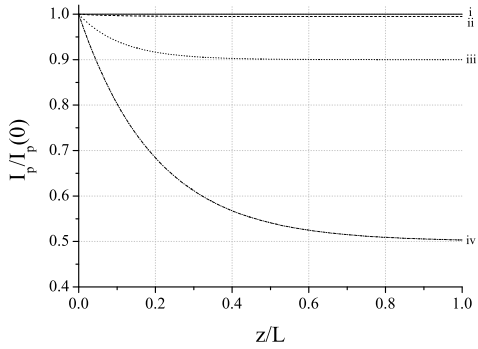

(a)

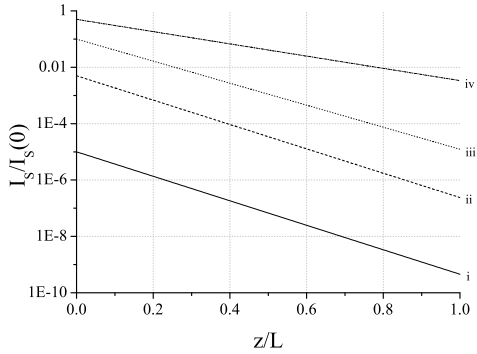

(b)

Figure 3.9: Spatial distribution of the (a) pump and (b) Stokes waves intensities as a function of distance ($\eta_P = 1$, $L = 10$km, $P_p(0) = 10\mu$W, $A_{eff} = 80\mu$m^2, $g_B = 5 \cdot 10^{-11}$m/W). The approximated solutions (3.47), (3.48) and (3.49) are perfectly superposed to the general solutions (3.46) calculated for: (i) r=10^{-5}; (ii) r=0.005; (iii) r=0.1; (iv) r=0.5.

To conclude this section, we stress on the fact that the equations (3.46) give the spatial distribution of the field intensities in terms of the boundary values $I_p(0)$ and $I_S(0)$. However, since the boundary values that are physically known are $I_p(0)$ and $I_S(L)$, we must express the unknown quantity $I_S(0)$ in terms of $I_p(0)$ and $I_S(L)$. We set, then, $z = L$ in (3.46b) and obtain the following transcendental equation in the variable r:

$$I_S(L) = I_p(0)\frac{r(1-r)}{e^{\gamma L} - r} \tag{3.50}$$

which can be numerically solved to express r in terms of the known quantities $I_p(0)$ and $I_S(L)$.

Approximate solutions of the equations (3.37) and (3.42) including the attenuation terms can be found in [19] and [22].

3.2.4 SBS in optical fibres

All nonlinear effects are dependent upon the intensity of the electromagnetic field in the medium. However, since it is the total optical power entering and leaving the fibre that is usually measured, some method is required for converting between the two when comparing theoretical and experimental results. The measured optical power leaving a fibre is simply the integral of the intensity distribution over the fibre cross section. Assuming a uniform intensity distribution, I, over a core of area A_{core}, the intensity can be calculated from the measured power, P_{meas}, using:

$$I = \frac{P_{meas}}{A_{core}} \tag{3.51}$$

Nevertheless, the field in a single mode fibre is not evenly distributed or even fully contained within the core. It is larger at the fibre axis than near the core-cladding interface and extends into the cladding to a degree depending on the actual

refractive index profile. Calculating a uniform intensity in the core using previous equation will underestimate the value on the axis of the fibre and overestimate the value near the core-cladding interface [23].

The effective area parameter, A_{eff}, introduced in section 2.2.3 (see page 22) has been defined for the purposes of calculating nonlinear effects. It is a single value, based on the modal field distribution (MFD), and can be used instead of A_{core} to calculate a value for the optical intensity. In conventional step-index fibres, the mode field is well approximated by a Gaussian function of radius w at the $1/e$ amplitude points (cf. equation (2.26) on page 16). In this case, the effective area can be shown simply to be

$$A_{eff} = \pi w^2(\lambda) \tag{3.52}$$

where $2w(\lambda)$ represents the MFD diameter of the fibre at the operating wavelength, λ.

The mode field diameter is a well-established parameter with recognised measurement procedures. However, for fibres that do not have simple step-index geometry such as dispersion-shifted and dispersion-flattened fibres, the mode field cannot be approximated by a Gaussian function and alternative methods are required to calculate the effective area. This can be done either by measuring the field distribution and using the equation (2.37) (see [24]), or by including a fibre-dependent correction factor into expression (3.52) and using the standard fibre MFD value [25].

SBS power threshold

On the basis of the considerations given above, the equations (3.37) of the incoherent model describing the spatial evolution

of the pump and Stokes waves can be expressed in terms of the optical powers, instead of the optical intensities:

$$\frac{\partial P_p}{\partial z} = -\eta_P \frac{g_B(\nu)}{A_{eff}} P_p P_S - \alpha P_p \tag{3.53a}$$

$$\frac{\partial P_S}{\partial z} = -\eta_P \frac{g_B(\nu)}{A_{eff}} P_p P_S + \alpha P_S \tag{3.53b}$$

where P_p and P_S are respectively the pump and Stokes power.

The evolution of the Stokes wave in the case of undepleted pump, but considering the attenuation term, is then given (accordingly to (3.47b)) by:

$$P_S(z) = P_S(L) e^{-\alpha(L-z)} e^{-\eta_P \frac{g_B(\nu)}{A_{eff}} P_p(0) L_{eff}(z)} \tag{3.54}$$

where L_{eff} is the effective length defined in section 2.2.3 (see page 24).

The Brillouin threshold is the critical pump power for which the emerging Stokes backscattered power becomes equal to the transmitted pump power [26]. It can be expressed as follows [27]:

$$P_{th} \approx K_{SBS} \frac{19 A_{eff}}{g_B L_{eff}} \tag{3.55}$$

where K_{SBS} is a polarisation factor depending on the polarisation of the pump and Stokes waves and takes values between 1 and 2 (typically 1.5 for completely scrambled polarisation). P_{th} typically amounts to some mW for 20-25km long standard fibres; it can be, however, conveniently increased in optical communication systems by broadening the gain spectrum through proper dithering of the pump wave frequency [28].

3.3 Influence of extrinsic parameters on the Brillouin gain spectrum

The properties of the Brillouin gain spectrum in an optical fibre can be modified by a variety of parameters. Some of them are *intrinsic* in the sense that they are related to the physical constitution of the medium, like the refractive index profile, the dopant material, the concentration of dopants and the birefringence. Others are *extrinsic* because they are not related to the physical structure of the medium and act as external variables, like temperature, strain and pressure.

The major interest in using Brillouin scattering for distributed sensing purposes comes expressly from the inherent sensitivity of the gain curve to the extrinsic parameters (see chapter 4), whereas the effect of the intrinsic variables is generally considered as a drawback to performances.

Effect of polarisation

By inspection of the equations (3.37) it is easy to see that the polarisation is a particularly critical parameter. In fact, since the polarisation efficiency η_P multiplies the Brillouin gain factor, the efficiency of the stimulated scattering process decreases if the optical waves do not have the same polarisation ($\eta_P < 1$). Eventually, when the polarisations are perfectly orthogonal ($\eta_P = 0$), no acoustic wave is generated and the SBS is completely suppressed. A comprehensive review of the polarisation effects on the Brillouin gain is reported in [14,24,29].

In an ideal fibre, the two fundamental eigenmodes are fully degenerated and carry uncoupled linear orthogonal polarisations having the same propagation constant. In real fibres, slight imperfections in the shape of the fibre's core induce a

finite amount of birefringence, resulting from the difference in the propagation constants of the eigenmodes. As a consequence, the state of polarisation of the optical waves varies during the propagation within the fibre. In the case of low-birefringent standard fibres, the polarisation variations are usually modelled as a three-dimensional Brownian motion [30]. It can be shown that the resulting efficiency η_P of the scattering process lies between 1/3 and 2/3 depending on the relative input polarisation of the two counterpropagating waves [24, 29]. As a major consequence, the measure of the Brillouin gain curve has to be made as a two-stages procedure, consisting in an adjustment of the polarisations in order to have respectively the maximal and the minimal gain contrast [31].

Effect of dopant concentration

The wave-guiding properties of an optical fibre are intimately related to the refractive index difference between the core and the cladding. The index enhancement in the core of standard fibres is typically obtained by the introduction of small quantities of dopants, such as germanium, phosphorus or titanium [24], in the core silica matrix. The nature and the concentration of dopants have a direct influence on the guiding properties of the acoustic waves inside the fibre [32–34].

Figure 3.10 reports the measurements of the Brillouin frequency shift and the Brillouin linewidth for several fibre samples exhibiting different concentrations of germanium oxide in the core.[6] The experimental points show an excellent correlation with the linear regression, and, for a pump wavelength of 1550 nm, the slope of the regression line is -80 MHz/mol%

[6]The concentration of germanium dioxide is generally expressed in percentage of the molar weight of GeO_2 over the molar weight of SiO_2.

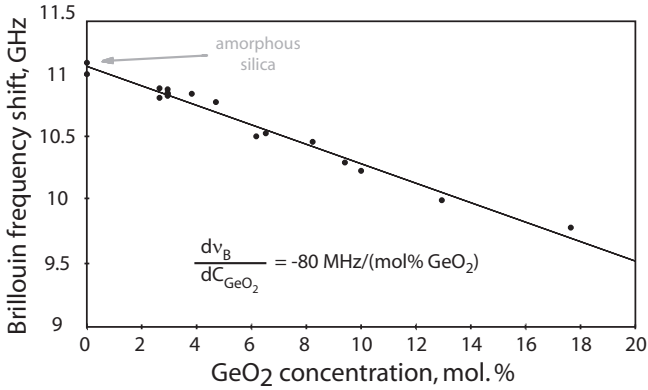

(a)

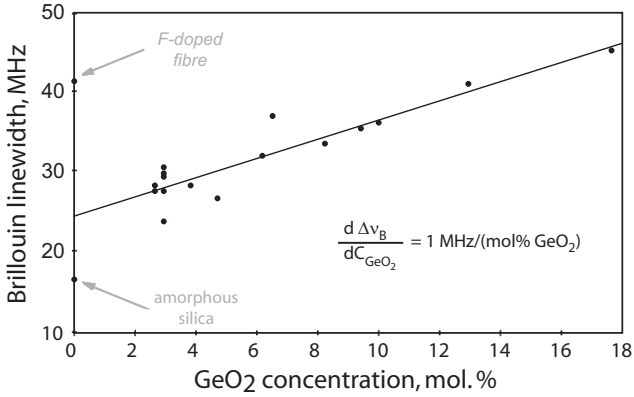

(b)

Figure 3.10: Influence of GeO_2 dopant concentration on the Brillouin gain spectrum at 1550nm. (a) Brillouin frequency shift. (b) Brillouin linewidth. From [24] (curves have been recalculated at 1550 nm by [14]).

GeO_2 (figure 3.10a). The negative sign of the slope finds its origin in the fact that the sound velocity in pure GeO_2 ($\sim$ 3780 m/s) is markedly lower than in silica ($\sim$ 5775 m/s). This dependence on the chemical composition can be used to identify the different fibers in a telecom network or to check the homogeneity of their composition [35]. The linewidth of the Brillouin gain is also found to vary linearly with the GeO_2 concentration, the constant of proportionality being close to 1 MHz/mol% GeO2 (figure 3.10b).

Effect of temperature and strain

According to the equation (3.17), the Brillouin shift, ν_B, is directly proportional to the acoustic velocity, v_a, which in turn is essentially dependent on temperature and density [36]. Any variations of these quantities can be evaluated through the measurement of the Brillouin gain spectrum.

Several studies [24,37] have previously demonstrated a linear variation of the Brillouin shift with temperature in the range -30 to 90°C (figure 3.11). This dependence can be expressed as:

$$\nu_B(T) = \nu_B(T_r) + C_T(T - T_r) \tag{3.56}$$

where T_r is a reference temperature and C_T denotes the Brillouin temperature coefficient. Typical values for C_T lie between 1.05 and 1.36 MHz/°C, at 1550 nm, depending on the fibre type. Is has also been shown that the increase in the Brillouin gain peak value exactly compensates for the narrowing of the spectrum [14,24], such that the product $g_0(T)\Delta\nu_B(T)$ stays constant. A comprehensive study of the physical properties of the Brillouin spectrum at very low and very high temperatures can be found in [22, 38]. When a longitudinal[7] strain

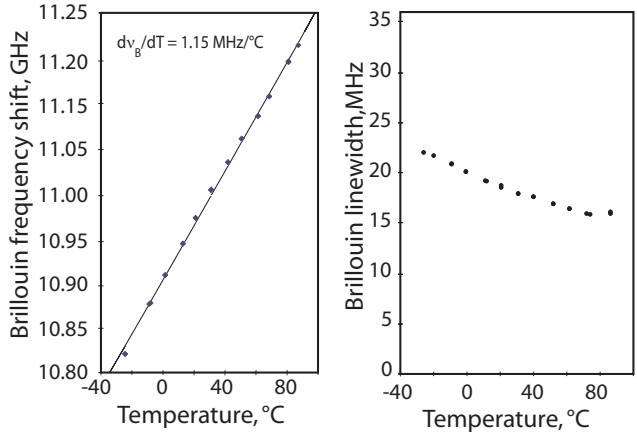

Figure 3.11: Dependence of Brillouin frequency shift and Brillouin linewidth on the temperature of a standard fibre. From [24] (curves have been recalculated at 1550 nm by [14].

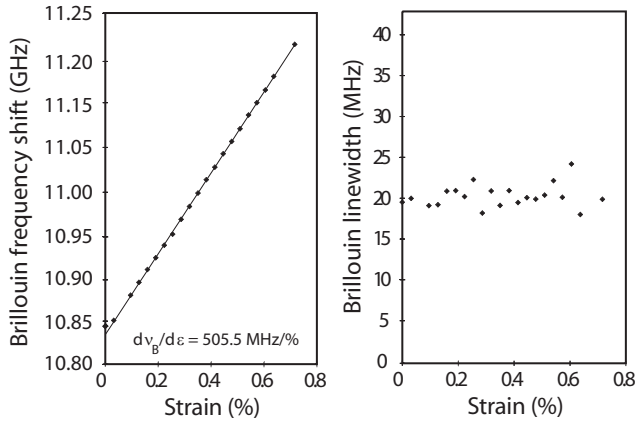

Figure 3.12: Dependence of Brillouin frequency shift and Brillouin linewidth on the longitudinal strain applied on a standard fibre. From [24] (curves have been recalculated at 1550 nm by [14]).

is applied to an optical fibre, the acoustic velocity changes according to the density variations of the medium. The Brillouin shift exhibits then a dependence on the applied strain of the form:

$$\nu_B(\epsilon) = \nu_B(0) + C_\epsilon \epsilon \tag{3.57}$$

where ϵ denotes the tensile strain applied to the fibre and C_ϵ is the Brillouin strain coefficient. The resulting curve (figure 3.12) displays a linear behaviour practically up to the breaking limit of the fibre ($\sim$1% of elongation). For the depicted fibre, C_ϵ has a typical value of 50.5 kHz/$\mu\epsilon$.[8] In general, the strain coefficient depends on the fibre composition and on the nature of the coating material. Some coatings are expressly used to reinforce the mechanical characteristics of the fibre and take a part of the applied stress, while other are simply used to protect the fibre from external agents. For what concerns the Brillouin linewidth, it does not seem to exhibit significant strain dependent variations.

We conclude this section reporting on the case when the fibre is submitted to high hydrostatic pressure. The Brillouin shift can then be expressed as:

$$\nu_B(P) = \nu_B(0) + C_P P \tag{3.58}$$

where P is the pressure and C_P is the Brillouin pressure coefficient. A typical value for C_P is -91MHz/kbar [22].

[7] By longitudinal strain we mean strain induced by stress along the fibre length. Strain induced by lateral pressure has very little effect on the Brillouin frequency shift [24].

[8] Elongations are usually measured in % of the overall length. Nonetheless, $\mu\epsilon$ are often employed in literature, one microstrain ($\mu\epsilon$) corresponding to a relative elongation of 10^{-6}.

Bibliography

[1] I. L. Fabelinskii, *Molecular Scattering of Light*. Plenum Press, New York, 1968.

[2] R. W. Boyd, *Nonlinear Optics*. Academic Press, 1992.

[3] Y. R. Shen, *The principles of nonlinear optics*. Wiley, NY, 1984.

[4] L. Brillouin, "Diffusion de la lumière et des rayons X par un corps transparent homogène : influence de l'agitation thermique," *Annales de Physique*, vol. 17, pp. 88–122, 1922.

[5] L. D. Landau and E. M. Lifshitz, *Statistical physics*. Butterworth-Heinemann, 3rd ed., 1984.

[6] I. L. Fabelinskii and V. S. Starunov, "Some studies of the spectra of thermal and stimulated molecular scattering of light," *Appl. Opt.*, vol. 6, no. 11, pp. 1793–1804, 1967.

[7] W. Kaiser and M. Maier, *Laser handbook*. North-Holland, Amsterdam, 1972.

[8] L. D. Landau and E. M. Lifshitz, *Fluid mechanics*. Butterworth-Heinemann, 2nd ed., 1987.

[9] E. Picholle, *Dynamique de la diffusion Brillouin stimulée dans les fibres optiques*. PhD thesis, Université de Nice - Sophia Antipolis, 1991.

[10] C. Kittel, *Introduction to solid state physics*, ch. 5. John Wiley & Sons, Inc., 4th ed., 1971.

[11] P. Lorrain and D. R. Corson, *Champs et ondes électromagnétiques*. Librairie Armand Collin, Paris, 1979.

[12] R. P. Feynman, R. B. Leighton, and M. Sandy, *The Feynman Lectures on Physics*, vol. 1. Addison Wesley, 2nd ed., 2005.

[13] A. Melloni, M. Frasca, A. Garavaglia, A. Tonini, and M. Martinelli, "Direct measurement of electrostriction in optical fibers," *Opt. Lett.*, vol. 23, no. 9, pp. 691–693, 1998.

[14] M. Facchini, *Distributed optical fiber sensors based on Brillouin scattering*. PhD thesis, Ecole Polythecnique Fédérale de Lausanne, 2002.

[15] V. Lecoeuche, *Stabilité et comportements dynamiques génériques des lasers Brillouin à fibre*. PhD thesis, Université des Sciences et Technologies de Lille, 1996.

[16] L. Stépien, *Diffusion Brillouin stimulée dans les fibres optiques: bruit d'intensité du laser et brûlage de trous spectral dans le générateur et l'amplificateur*. PhD thesis, Université des Sciences et Technologies de Lille, 2002.

[17] A. Yarif, *Optical Electronics*. The Oxford Series in Electrical and Computer Engineering, Oxford University Press, USA, 4th ed., 1991.

[18] M. González-Herráez, K.-Y. Song, and L. Thévenaz, "Optically controlled slow and fast light in optical fibres using stimulated Brillouin scattering," *Appl. Phys. Lett.*, vol. 87, p. 081113, 2005.

[19] L. Chen and X. Bao, "Analytical and numerical solutions for stady state stimulated Brillouin scattering in a single-mode fiber," *Opt. Commun.*, vol. 152, pp. 65–70, June 1998.

[20] C. L. Tang, "Saturation and spectral characteristics of the Stokes emission in the stimulated Brillouin process," *J. Appl. Phys.*, vol. 37, pp. 2945–2955, July 1966.

[21] R. H. Enns and I. P. Batra, "Saturation and depletion in stimulated light scattering," *Phys. Lett.*, vol. 28A, pp. 591–592, January 1969.

[22] S. Le Floch, *Etude de la diffusion Brillouin stimulée dans les fibres optiques monomodes standard. Application aux capteurs de température et de pression.* PhD thesis, Université de Bretagne Occidentale, 2001.

[23] R. Billington, "Measurement methods for stimulated Raman and Brillouin scattering in optical fibres," tech. rep., NPL Report COEM 31, June 1999.

[24] M. Niklès, *La diffusion Brillouin dans les fibres optiques: étude et application aux capteurs distribués.* PhD thesis, Ecole Polytechnique Fédérale de Lausanne, 1997.

[25] Y. Namihira, A. Miyata, and N. Tanahashi, "Nonlinear coefficient measurements for dispersion shifted fibres using self-phase modulation method at 1.55 μm," *Electron. Lett.*, vol. 30, no. 14, pp. 1171–1172, 1994.

[26] R. G. Smith, "Optical power handling capacity of low loss optical fibers as determined by stimulated Raman and Brillouin scattering," *Appl. Opt.*, vol. 11, no. 11, pp. 2489–2494, 1972.

[27] L. Thévenaz, "Limitations caused by nonlinear effects," *COST 241, Final Report, SG2.4*, pp. 97–100, 1998.

[28] D. Cotter, "Suppression of stimulated Brillouin scattering during transmission of high power narrowband laser light in monomode fibre," *Electron. Lett.*, vol. 18, pp. 638–640, 1982.

[29] O. Deventer and J. Boot, "Polarization properties of stimulated Brillouin scattering in single-mode fibres," *J. Lightwave Technol.*, vol. LT-12, pp. 585–590, 1994.

[30] G. J. Foschini and C. D. Poole, "Statistical theory of polarization dispersion in single mode fibers," *J. Lightwave Technol.*, vol. 9, no. 11, pp. 1439–1456, 1991.

[31] M. Niklès, L. Thévenaz, and P.-A. Robert, "Brillouin gain spectrum characterisation in single-mode optical fibres," *J. Lightwave Technol.*, vol. 15, no. 10, pp. 1842–1851, 1997.

[32] N. Shibata, R. G. Waarts, and R. P. Braun, "Brillouin-gain spectra for single-mode fibers having pure-silica, GeO_2-doped and P_2O_5-doped cores," *Opt. Lett.*, vol. 12, pp. 269–271, April 1987.

[33] N. Shibata, K. Okamoto, and Y. Azuma, "Longitudinal acoustic modes and Brillouin-gain spectra for GeO_2 doped-core single mode fibres," *J. Opt. Soc. Am. B*, vol. 6, no. 6, pp. 1167–1174, 1989.

[34] W. M. Henri, "Fibre acoustic modes and stimulated Brillouin scattering," *Intern. J. Optoelectron.*, vol. 7, no. 4, pp. 453–, 1996.

[35] L. Thévenaz, M. Niklès, A. Fellay, M. Facchini, and P.-A. Robert, "Applications of distributed fibre sensing," in *Proceedings of SPIE International Conference on Applied Optical Metrology*, (Balatonfüred, Hungary), pp. 374–381, 1998.

[36] S. P. Timoshenko and J. N. Goodier, *Theory of Elasticity*, ch. 14. McGraw-Hill, NY, 1970.

[37] T. Kurashima, T. Horiguchi, and M. Tateda, "Thermal effects on the Brillouin frequency shift in jacketed optical silica fibres," *Appl. Opt.*, vol. 29, no. 15, pp. 2219–2222, 1990.

[38] A. Fellay, *Extreme temperature sensing using Brillouin scattering in optical fibres*. PhD thesis, Ecole Polytechnique Fédérale de Lausanne, 2003.

Chapter 4

Distributed sensing based on stimulated Brillouin scattering

4.1 Introduction

The action of sensing is a very common and natural action human beings do in every-day life in order to collect informations about the physical world. How these informations are perceived and interpreted by the brain, and how the reality is modelled on our perception are fascinating speculations for philosophers and epistemologists [1, 2].

From a metrological point of view, a sensor is a physical (electrical, mechanical, chemical, dielectric, ...) device that maps an environmental attribute to a quantitative measurement in a form easily understandable by the brain. Sensors are based on a transduction principle consisting in the conversion of energy from one form to another.

The optical fibre, which has been specifically designed to transmit light signals and is the major responsible of the information revolution which has characterized the past 20 years, can behave as a transducer as well. This aspect has brought to another technological revolution, not involving communications, which is the ever expanding field of optical fibre sensors.

An important advantage of fibre optic sensors is their ability to provide passive sensing of a wide range of physical fields. This not only means that the sensor head operates without the need for electrical power, but that the overall system, including the input-output fibres which serve as telemetry links, is also electrically passive. By consequence, the whole system exhibits a low intrinsic susceptibility to the effects of electromagnetic interference and electromagnetic pulse, making fibre sensors suitable for use in explosively hazardous or electrically noisy environments [3–5].

Sensors can be mainly classified distinguishing between two general approaches to the problem of sensing: point and distributed measurement. *Point* sensors are able to retrieve informations about a particular physical quantity only relatively to their specific spatial position. On the contrary, *distributed* sensors can collect informations about physical parameters on an extended region throughout the sensor itself [6–8].

The inherent distributed sensing nature of intrinsic fibre sensors can be used to create unique forms of sensors for which, in general, there is no counterpart on conventional sensor technologies. In an intrinsic sensor, the modulation of the optical carrier induced by the measurand field occurs while the light remains guided within the fibre, in contrast to extrinsic sensors where the light, in general, leaves the fibre in the sensing region, passes through some external transduction element and is then re-coupled back into a fibre that guides the optical signal

to a detector [9].

Intrinsic distributed fibre sensors are particularly attractive for use in applications where monitoring of single or multiple measurands is required for a large number of points or continuously, as a function of location, along the path of the fibre. They can be used for measuring strain [10], temperature [11], pressure [12], electrical and magnetic fields, radiation (neutrons, γ-rays, and X-rays) and vibrations. Other application areas include monitoring of stress in large civil structures [13,14] such as buildings, bridges, dams, mines (detection of surface movements) and tunnels (detection of rock deformation during construction), vehicles and machines (such as aircraft, ships, high-speed trains, or space shuttles). They can also be used for leakage and crack detection in pipelines, for temperature profiling over a wide range of temperatures [11] in electrical power transformers, generators, reactor systems, pressure vessels, power cables [15] and for simple fire detection. Other important applications include the evaluation of damages in composite materials and the monitoring of composite materials during production processes, especially in the aerospace industry [4, 5, 7, 16, 17]. Good reviews of distributed fibre sensing applications can be found in [17–19].

Distributed optical fibre sensors involve a large variety of different techniques. Classical methods, such as optical time-domain reflectometry (OTDR) [20] and Raman OTDR [21], rely on the measurement of the intensity of backscattered light as a function of time, whereas polarisation optical time-domain reflectometry (POTDR) [22] is based on the monitoring of the polarisation state of the back-reflected light. In Brillouin optical time-domain reflectometry (BOTDR) [23], the location information is obtained as in OTDR, except the fact that the signal magnitude is obtained from the Brillouin scatter-

ing frequency shift. An improved version of BOTDR, of particular interest in the frame of this work, is Brillouin optical time-domain analysis (BOTDA) [24], which utilises two counterpropagating lightwaves to amplify the optical signal bringing the location information. In frequency-modulated continuous-wave (FMCW) [25] methods, the frequency spectrum of the detected light yields the spatial distribution of the measured variable, and in optical coherence domain reflectometry (OCDR) [26] an optical coherence function is synthesized into a sensing fibre, which returns the measured-variable information at a certain distance. Finally, interferometric techniques employ a ring interferometer, such as a Sagnac loop, with some other interferometer, such as a Michelson [27] or another Sagnac [28] interferometer, to obtain the spatial information. A comprehensive review of the state of the art and a comparison of the performances (according to range and resolution) of the different methods can be found in [5].

In this chapter we illustrate the technique of distributed measurement based on the Brillouin scattering (BOTDA) and we describe our original sensing system, presenting the figures of merit and discussing some of the physical effects which limit the performances of the sensor. After spending some words on the theory of injection-locking in semiconductor lasers, and presenting its application to the generation of extremely pure optical signals, we focus in particular on the impact modulation instability has on the performances of Brillouin sensors.

4.2 Brillouin optical time domain analysis: a distributed sensing technique

The first idea at the origin of distributed fibre sensing techniques has to be found in the invention of the optical time-domain reflectometry (OTDR) [20], which enables nondestructive evaluation of the optical fibre loss by time-resolved measurement of backward Rayleigh scattering. The principle of operation is very straightforward and consists in a time-of-flight analysis [29, 30] like that used by radars: an intense pulse is launched into the fibre and the backscattered light is recorded as a function of time; knowing the velocity of light in silica, the temporal variations of the backscattered power can be converted into spatial variations, making thus possible the location of bad splices or other regions with abnormally high losses.

Nonetheless, since Rayleigh scattering is very weak especially in single mode fibres and at long wavelengths, to overcome the dynamic range limitations of conventional OTDR, Horiguchi and Tateda [24] proposed and demonstrated a new technique based on the Brillouin interaction between an optical pump pulse and a counterpropagating continuous probe wave, and they named it BOTDA (Brillouin optical time-domain analysis). The optical configuration is depicted in figure 4.1. The principle of operation is similar to that of OTDR with the only difference that when the frequency shift between the pump pulse and the probe wave is tuned to the Brillouin frequency shift of the fibre, the probe intensity is amplified through the stimulated Brillouin scattering process. The existence of localised anomalies within the fibre is then detected as a function of time through the usual reflectometric analysis. The optical signal power of BOTDA can be more than 100 times greater than the Rayleigh backscattered power, and the use of

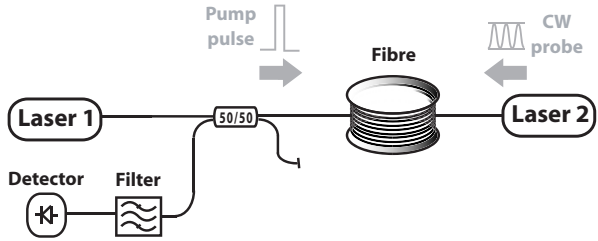

Figure 4.1: Optical configuration for the BOTDA. The frequency shift between the pump pulse wave and the continuous probe wave is tuned to the Brillouin shift of the fibre. In the crossing region with the pump pulse, the probe intensity undergoes an amplification and is spatial-resolved through the usual time-of-flight analysis.

an optical filter before the detection stage can further enhance this contrast.

The dependence of the Brillouin gain on several extrinsic parameters, like strain and temperature (see section 3.3), makes the BOTDA a good candidate for distributed sensing [31, 32]. Since the sensing information is frequency encoded in the Brillouin shift by means of the relations (3.57) and (3.56), it is essential to retrieve the Brillouin gain spectrum at any location along the fibre, by simply varying the frequency of the continuous probe wave relatively to the pump pulse frequency. The Brillouin shift is then unambiguously determined as a function of distance and the spatial profiling of variables like temperature or strain can be easily retrieved. The principle of operation of such a distributed sensor is depicted in figure 4.2.

BOTDA for distributed strain and temperature measurement was first demonstrated at 1.32 μm by using a Nd:YAG laser and a DFB laser diode [31]: the frequency accuracy was

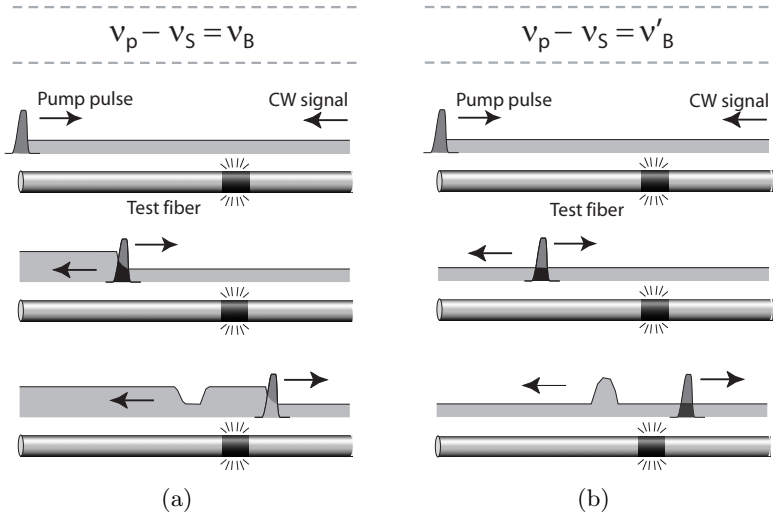

Figure 4.2: Principle of operation of a distributed sensor in the pulsed pump-continuous probe wave configuration. Under normal conditions, the optical fibre exhibits a Brillouin frequency equal to ν_B and the Brillouin gain is constant along the fibre. When strain and/or temperature are applied on some section of the fibre, the Brillouin frequency shifts to ν'_B and the Brillouin gain drastically decreases. (a) If the frequency difference between the pump and the probe waves is tuned to ν_B, the probe is amplified all over the fibre except at the specified location; (b) conversely, if the frequency difference is tuned to ν'_B, the probe is amplified only at the specified location.

10 MHz and the spatial resolution was 100 m. The frequency accuracy could be improved to 1 MHz (corresponding to a strain and temperature accuracy of 20 $\mu\epsilon$ and 1.5°C) by using an external grating cavity laser diode with a narrower linewidth; better spatial resolutions (down to 1 m) could successively be obtained at 1.55 μm using an erbium doped fibre amplifier (EDFA) to boost the power of the pump pulse. Later, Bao *et al.* [33] significantly extended the BOTDA performances by using Brillouin loss rather than Brillouin gain, and achieved a 32 km sensing length with a spatial resolution of 5 m.

These measurements were performed using two distinct lasers for generating pump and probe signals, with a manifest limitation residing in the difficulty to maintain a stable frequency difference between the two light sources.[1] To overcome this problem, Niklès *et al.* [34] proposed to generate both the pump and the probe waves from a single physical light source by using an electro-optical modulator (EOM) and by properly setting its DC bias. This approach implies, withal, that the probe signal is made of two sidebands, the upper of which is not relevant for the measurement and needs to be accurately filtered. In addition, to efficiently suppress the carrier frequency, the DC bias must be correctly set using a very stable and precise PID regulator and the EOM must exhibit a good extinction ratio (at least 30 dB). Since standard commercially available EOMs are rather expensive components and exhibit a typical extinction ratio of 20 dB, we report on a different and efficient scheme using two distinct injection-locked lasers.

[1] The wavelengths of two independent lasers drift slightly in time through scarcely controllable environmental parameters such as temperature or electrical current, but sufficiently enough to decrease the signal to noise ratio and seriously impair the Brillouin gain measurement.

4.3 Theory and applications of injection locking in semiconductor lasers

In march 1665 Christiaan Huygens wrote a letter to his father Constantyn to tell him an amazing phenomenon he had observed some days before while confined to bed by illness. He noticed that the pendulums of two clocks hung on the wall of his room invariably felt into synchronism when brought close enough to each other, but became free-oscillating when kept farther apart [35]: he explained the coupling mechanism by mechanical vibrations transmitted through the wall[2] [36]. This simple anecdote (mainly cited on [37] and [38]) represents the first observation of synchronization between two oscillators. This effect is very common in a variety of natural systems, from mechanical constructions to highly complex biological organisms involving two or more oscillators: some striking natural examples include the locking of human circadian rhythms to the length of the day[3], the interaction between pacemaker cells in the heart, the communication between neurons in the cortex and the synchronised flashing mating calls of entire trees of tropical fireflies [41, 42].

The frequency locking phenomenon between two oscillators has been an area of interest for physicists and mathematicians for centuries. Later observations are reported by Lord Rayleigh in 1907 who observed the coupling between two tuning forks on

[2]Huygens had not only given an exact description, but also a brilliant qualitative explanation of mutual synchronization; he correctly understood that the conformity of the rhythms had been caused by an imperceptible motion of the beam.

[3]It has been observed for example that humans left in isolated bunkers reveal a "free-running" sleep-wake period of about 25 hours but, when brought back to the nature, they are injection-locked to the Earth's cycle [39, 40].

a table top and studied the locking behaviour as a function of frequency and coupling strength [43]: this could be regarded as the beginning of a systematic investigation of synchronization in modern physics. Nevertheless, the phenomenon did not begin to be entirely understood until the development of nonlinear dynamics by Poincaré [44]. This new mathematical tool allowed Appleton [45] and Van der Pol, another Dutch scientist, to study the forced oscillator in details for the first time [46,47]. The advent of radio-communication era brought on a vigorous research into electrical circuits that also led to advances in the understanding of locking phenomena. With his pioneer works on microwave-tubes oscillators, Adler demonstrated nearly two decades later that the frequency locking synchronization can also apply to electronic circuits [48] with a significant improvement regarding phase noise reduction [49, 50].

It was not until 1966, shortly after the invention of the laser, however, that Stover and Steiner demonstrated the locking of two helium-neon laser oscillators [51] and only in the early seventies Buczek provided a review of the theory and applications of laser injection locking with CO_2 lasers [52]. In the late seventies, the improvements in semiconductor laser characteristics, such as increased spectral purity and high mode stability, provided new motivation for injection locking these lasers. The first demonstration of semiconductor laser injection locking is due to Kobayashi and Kimura in 1980 [53] and the theoretical approach was generalized by Otsuka and Tarucha in 1981 [54]. Later works dealt with several promising applications for both speed digital and coherent transmission systems. It was shown that the technique ensures single-mode operation under high-speed modulation [55–58]; enhances the modulation bandwidth reducing relaxation oscillations [59–61]; can reduce the partition noise, the linewidth, and the frequency

noise [62–64]; can limit the frequency chirping [65, 66]; is able to generate optical frequency- and phase-modulation [67, 68]; can amplify FM signals [69]; can be used to obtain optical frequency conversion [70] and to generate microwave signals [71].

In parallel with the development of applications, the theory of semiconductor laser locking has evolved as well. Lang pointed out that including the linewidth enhancement factor, which takes account of the carrier-dependent refractive index, was necessary for the theoretical developments of injection locked semiconductor lasers [72]. He showed also, from the linear stability analysis of the semiconductor rate equations, that for certain operating conditions within the locking bandwidth, the slave becomes dynamically unstable. Successive works dealt with the theoretical evaluation of the spectral densities of the intensity and phase noise [73, 74], and more recently a particular attention has been devoted to bistability and chaos synchronisation in injection-locked lasers [75].

We briefly report here some mathematical tools needed for a theoretical understanding of the injection locking phenomena in distributed feedback (DFB) semiconductor lasers. A comprehensive study can be found in [76].

4.3.1 Rate and phase equations

In the cavity of an optically injected laser the electromagnetic field of the light from the master laser adds to the internal field of the free-running laser. Let $E_s(t)$ and $E_m(t)$ be the complex electric fields of, respectively, the slave and the master laser. According to [72], the rate equation for the intracavity field

may be written as:

$$\frac{dE_s}{dt} = \left\{ -i\omega_{th} + \frac{1}{2}(G(t) - \gamma)(1 - i\beta_c) \right\} E_s(t) + \frac{1}{\tau_L} E_m(t) \tag{4.1}$$

where ω_{th} is the angular frequency of the slave laser at threshold, $G(t)$ is the modal gain per unit time, and τ_L is the cavity round trip time. β_c is the linewidth enhancement factor and is defined by the carrier-induced variation of real and imaginary part of the susceptibility χ [77]:

$$\beta_c \equiv \frac{d[\Re\{\chi\}]/dN}{d[\Im\{\chi\}]/dN} \tag{4.2}$$

with N the free charge carrier number in the active region of the laser. γ is the photon loss, and is defined as the sum of the cavity loss α_m and the internal loss α_{int}, multiplied by the group velocity:

$$\gamma = v_g(\alpha_m + \alpha_{int}) \tag{4.3}$$

The slave laser intracavity field and the injected optical field from the master laser can be written as:

$$E_s(t) = A_s(t)e^{-i(\omega_R t + \phi_s(t))} \tag{4.4a}$$

$$E_m(t) = A_m(t)e^{-i(\omega_R t + \phi_m(t))} \tag{4.4b}$$

where A_s and A_m are slowly varying field amplitudes, ϕ_s and ϕ_m are phase terms, and ω_R is a constant reference angular frequency. Assuming that the master laser is an ideally stable monochromatic source, the phase of the injected signal is constant: $\phi_m(t) = \phi_{m0}$. Since the reference frequency can be freely chosen [37,76], it is advantageous to set ω_R equal to the angular frequency of the master laser: $\omega_R = \omega_m$.

Inserting the equations (4.4) in (4.1), after separating the real and imaginary parts, we easily get two equations for the amplitude and phase of the intracavity field:

$$\frac{dA_s}{dt} = \frac{1}{2}(G-\gamma)A_s + \frac{1}{\tau_L}A_m\cos(\phi_{m0}-\phi_s) \tag{4.5a}$$

$$\frac{d\phi_s}{dt} = -(\omega_m-\omega_{th}) + \frac{1}{2}\beta_c(G-\gamma) + \frac{1}{\tau_L}\frac{A_m}{A_s}\sin(\phi_{m0}-\phi_s) \tag{4.5b}$$

where the explicit time dependences have been dropped for simplicity. The above equations can be conveniently expressed in terms of the intracavity laser photon numbers, P_s and P_m [77]. To this end, the slowly varying amplitudes A_s and A_m are normalised as follows:

$$P_s = V_P A_s^2 \qquad P_m = V_P A_m^2 \tag{4.6}$$

where $V_P = V/\Gamma$ is the volume of the optical mode, defined as the active volume (V) divided by the confinement factor (Γ) [78]. By expressing the fields A_s and A_m in terms of the dimensionless intracavity photon populations, respectively P_s and P_m, we obtain:

$$\frac{dP_s}{dt} = (G-\gamma)P_s + R_{sp} + 2\rho P_s\cos\theta \tag{4.7a}$$

$$\frac{d\theta}{dt} = \Delta\omega - \frac{1}{2}\beta_c(G-\gamma) - \rho\sin\theta \tag{4.7b}$$

where ρ contains the ratio between the injected and the total photon numbers:

$$\rho = \frac{1}{\tau_L}\sqrt{\frac{P_m}{P_s}} \tag{4.8}$$

θ contains the slave laser phase: $\theta(t) = \phi_{m0} - \phi_s(t)$, and $\Delta\omega$ denotes the angular frequency difference between the master

and the free-running slave: $\Delta\omega = \omega_m - \omega_{th}$. The term R_{sp}, keeping account of the spontaneous emission rate, has been added phenomenologically.[4]. From the inspection of the equations (4.5), we clearly see that the terms which are actually responsible for the external injection locking are the sine and cosine terms in the right-hand side.

The description of the model is completed by the equations relating the carrier number to the modal gain. We mainly focus on distributed feedback (DFB) lasers, which have been used in the frame of this work. For a single-mode diode laser with a bulk active region, the carrier rate equation reads [77]:

$$\frac{dN}{dt} = \eta_i \frac{I}{q} - \gamma_e N - G P_s \tag{4.9}$$

where η_i is the internal quantum efficiency, I the electric current driving the device, q the unit charge, and γ_e the total carrier loss rate which takes account of both radiative and nonradiative recombination mechanisms. The modal gain per unit time G is related to the carrier and the photon number by the following expression:

$$G = \frac{\Gamma v_g a}{V} \frac{N - N_0}{\sqrt{1 + P_s/P_{sat}}} \tag{4.10}$$

where a is linear gain constant, P_{sat} the saturated photon number, and N_0 the active layer carrier number at transparency.

[4] $R_{sp}(t)$ is assumed to depend linearly on the gain through the population inversion factor, n_{sp}, which is determined by the separation between the quasi-Fermi levels in the valence and conduction bands and the lasing frequency [77]

4.3.2 Steady-state behaviour of injection-locked slave lasers

Assuming that the slave laser is driven at constant current above threshold, the steady-state behaviour is obtained by setting the time derivatives in equations (4.7) and (4.9) equal to zero:

$$(G-\gamma)P_s + R_{sp} + 2\rho P_s \cos\theta = 0 \tag{4.11a}$$

$$\Delta\omega + \frac{1}{2}\beta_c(G-\gamma) - \rho\sin\theta = 0 \tag{4.11b}$$

$$\eta_i\frac{I}{q} - \gamma_e N - GP_s = 0 \tag{4.11c}$$

By combining the first two equations and neglecting the spontaneous emission rate, one get an expression for the angular frequency offset $\Delta\omega$:

$$\Delta\omega = \rho(\sin\theta - \beta_c\cos\theta) \tag{4.12}$$

The first sine term is characteristic for any kind of externally locked oscillators [48] and hence also for injection-locked laser oscillators. The second term, in stead, is specific to semiconductor devices because of their non-negligible linewidth enhancement factor, β_c.

Setting $\theta_0 = \arctan(\beta_c)$ as an auxiliary variable, the equation (4.12) may be rewritten as:

$$\Delta\omega = \rho\sqrt{1+\beta_c^2}\sin(\theta-\theta_0) \tag{4.13}$$

and, considering that the sine takes values within $[-1,+1]$, we obtain a simple expression for the maximum angular frequency offset between the master and the free-running laser:

$$\Delta\omega_{max} = |\omega_m - \omega_{th}|_{max} = \rho\sqrt{1+\beta_c^2} = \frac{1}{\tau_L}\sqrt{\frac{P_m}{P_s}(1+\beta_c^2)} \tag{4.14}$$

Equation (4.14) shows that for a given photon number (or power) ratio, P_m/P_s, the static locking range extends from $-\Delta\omega_{max}$ to $+\Delta\omega_{max}$, and increases with the square root of the injected power. The steady-state solutions for the photon P and carrier populations N, as well as for the phase θ of the injection-locked slave laser at a given point (P_m/P_s,$\Delta\omega$) inside the locking range, are reported in [76].

To investigate the stability of the steady-state solutions with respect to weak perturbations, a small signal analysis of the equations (4.7) and (4.9) must be applied. Omitting excessive mathematical details for which we refer to [76–78], from the linear stability analysis it is seen that the static locking range is divided into two main regions: an area of stable locking and an area of dynamic instability, predominantly at positive detunings. This situation is depicted in figure 4.3, where the predictions of the theoretical model are fully validated by experimental measurements [76].

To compare the measurements with the model, a relationship is needed between the injected photon number P_m and the incoming mode-matched power P_{inj}, and also between the total intacavity photon number P_s and the outcoupled power per facet P_{out}^{fr}. Admitting that the slave diode laser emits about the same power through both facets, P_{out}^{fr} may be related to P_s by [77]:

$$P_{out}^{fr} = \frac{1}{2}\frac{\hbar\omega_{th}P_s}{\tau_L}\,2\alpha_m\;L \tag{4.15}$$

where $\hbar\omega_{th}$ is the photon energy, α_m the distributed mirror loss and L the cavity length. Since the frequency of the injected signal from the master laser is virtually identical to the resonant frequency of the free-running slave lasing mode, α_m can be viewed as the cavity loss for both out- and in-coupled light. Therefore, by analogy, the injected energy per round-trip time

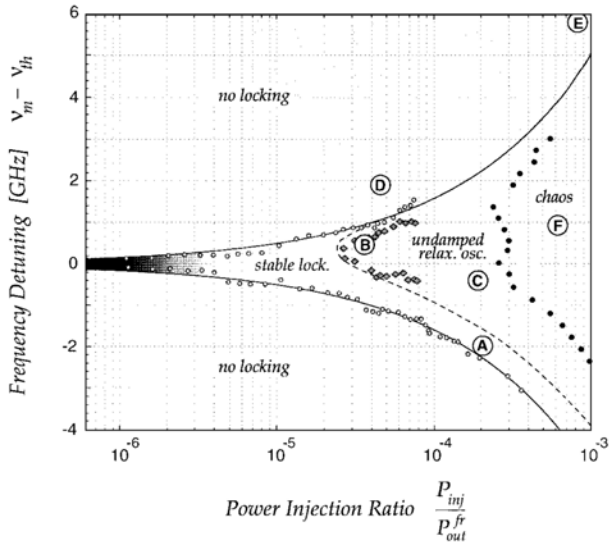

Figure 4.3: Locking range $\Delta\nu$ versus optical power ratio P_{inj}/P_{out}^{fr}. Dots, circles and diamonds denotes measurements, while lines result from theoretical model. Mainly four regimes can be distinguished: stable locking (A), unstable locking with undamped relaxation oscillations at low injection (B,C), unstable locking with chaos at high injection (F), and a regime with no locking (D,E). From [76].

coupled into the slave may be written as [76]:

$$\frac{\hbar\omega_{th}P_m}{\tau_L} = 2\alpha_m L\, P_{inj} \tag{4.16}$$

and by combining (4.15) and (4.16) we easily find:

$$\frac{P_{inj}}{P_{out}^{fr}} = \zeta\frac{P_m}{P_s} \tag{4.17}$$

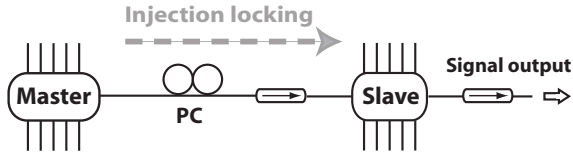

Figure 4.4: Basic injection-locking configuration of two DFB semiconductor lasers. The isolator protects the master from any light of the slave, and polarisation controller (PC) is properly set to maximise the polarisation coupling.

with $\zeta = 1/[2(\alpha_m L)^2]$ the coupling factor. Measurements and theoretical model are now entirely linked.

In the next section we address an important case of applications in which two DFB semiconductor lasers are in a master–slave configuration, and we present the advantages of injection locking for optical signal processing as well (especially for the generation of pure AM, pure FM and frequency-shifted optical wave forms).

4.3.3 Application of injection locking to the generation of optical signals

The basic injection-locking configuration of two DFB semiconductor lasers is shown in figure 4.4. The master is carefully isolated in order to prevent light coupling from the slave to the master and to protect master cavity from back-reflected light, and a polarisation controller (PC) is properly set to make polarisation matching inside the cavity (see section 4.4).

Beyond the trivial case of injection locking when the slave laser simply perfectly replicates the master CW emission, more interesting configurations can be set up to achieve more sophisticated signals. In particular the traditional drawback of

mixed FM–AM modulation resulting from the direct modulation of a laser diode can be overcome to a wide extent using injection locking. Traditionally pure AM, FM and SSB modulation spectra are obtained using a single or a combination of expensive external modulators. It can be shown that the same result can be obtained with excellent performances using an injection-locking scheme with two DFB lasers [79]. Such a solution turns out to be frequently cost-effective with the further advantage of better signal purity.

Pure AM modulation This is achieved by operating the master laser in CW mode and modulating the current of the slave at the modulation frequency. The carrier of the slave locks on the master emission line, resulting in no frequency dithering and therefore no unwanted FM modulation, as shown in figure 4.5. It can be observed that the spectrum is substantially narrowed and becomes symmetrical as expected for pure AM, while the time response is unchanged with or without locking. The amount of injected power into the slave must be carefully adjusted to obtain the proper emission characteristics.

In figure 4.5, for a modulation frequency $f = 200$ MHz, the AM power modulation index $M = \Delta P/P$ remains unchanged at $M = 0.2$ before and after locking, while the FM modulation index $\beta = \Delta f/f$ is changed from $\beta = 6.4$ to $\beta = 0.013$, demonstrating the massive reduction in frequency dithering resulting from injection locking.

Pure FM modulation In this case the current of the master laser is modulated at the modulation frequency while the slave is operated in CW mode. The instantaneous frequency of the slave laser locks onto the instantaneous emission line of

the master. The slave shows no significant change in its emission power, resulting in a pure frequency dithering, as shown in figure 4.6 where the slave spectrum is broad and symmetrical. While the master shows in the time domain an important AM modulation as expected from direct modulation, no AM modulation is observed in the slave emission, demonstrating pure FM modulation. Here the operating condition requires that the instantaneous frequency range lies within the locking range. More quantitatively a FM modulation index of $\beta = 2.8$ was measured, while the power AM modulation index was $M = 0.41$ in the master emission and was only $M = 0.009$ in the slave emission, corresponding to a -20.5 dB residual AM modulation.

Locking on a modulation sideband Optical frequency shifting can be simply achieved by modulating the current of the master laser and by locking the slave on one of the modulation sidebands: as a consequence, the frequency difference of the two lasers is perfectly stable (see section 4.4). The experimental configuration is identical to that shown in figure 4.4, the only difference being that the modulation frequency exceeds the locking range, so that only one frequency component of the modulation spectrum matters for the injection locking. It must be pointed out that the slave laser may be locked as well on a higher order sideband, resulting in an optical frequency difference that is a multiple of the applied modulation frequency. This is particularly convenient in the microwave domain, and locking up to the fifth harmonic was successfully demonstrated [76]. Such a scheme can be conveniently applied in many experimental configurations, in particular for distributed Brillouin fibre sensing for which this technique was successfully demonstrated, as discussed in the next section.

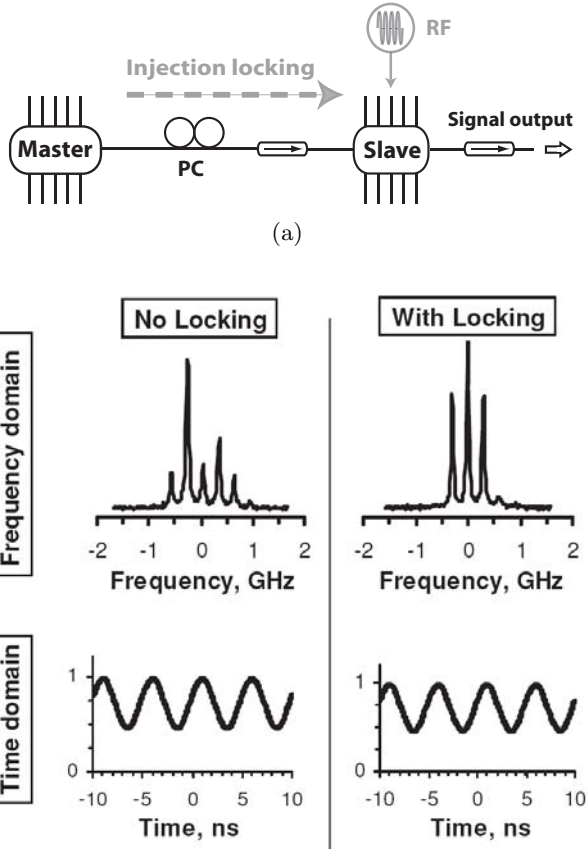

Figure 4.5: Injection-locking configuration for pure AM modulation. The spectrum and time-domain wave form of the slave laser are shown before and after locking to the master laser.

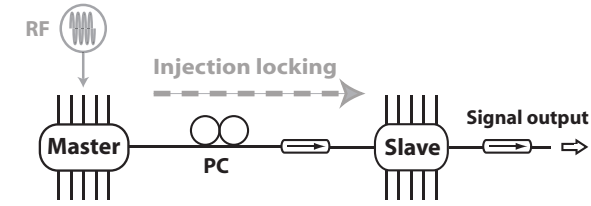

(a)

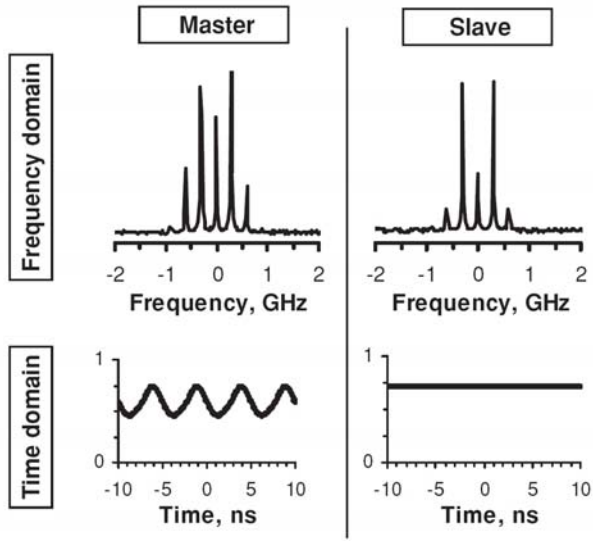

(b)

Figure 4.6: Injection-locking configuration for pure FM modulation. The spectra and time-domain wave forms of the master and of the slave laser are shown.

4.4 Experimental set-up based on injection locking of two distinct lasers

We saw in section 4.2 that both the pump and the probe waves for distributed Brillouin sensing can be generated from a single physical light source by using an electro-optic modulator and by properly setting its DC bias [34]. We addressed as well some practical problems concerning the relatively high costs and the unsatisfactory extinction ratios exhibited by commercially available EOMs. Actually, the effect of the finite extinction ratio of an electro-optic modulator on the performances of distributed probe–pump Brillouin sensor systems is quite critical, since it affects the Brillouin spectral shape and limits the ability of BOTDA to obtain localised spatial information [80].

Injection-locking constitutes an alternative and efficient method to provide stable, while tunable, frequency difference between the two lightwaves. This approach consists in modulating the master laser radiation and locking the (unmodulated) slave laser to a sideband of the master. The beat note between the master laser and the injection locked slave laser provides, this way, a high power and spectrally very pure RF signal. This concept of millimetre-wave optical generation by modulation sideband injection locking has been experimentally demonstrated in [76] and [81].

The block diagram of our set-up is schematically shown in figure 4.7. Both master and slave lasers are distributed-feedback (DFB) semiconductor lasers at the operating wavelength of 1550 nm, characterised by a few mW output power. The master laser is directly modulated in intensity at a frequency within the Brillouin shift range, thanks to the built-in electro-absorption modulator (EAM), which creates small sidebands which are used for injection locking. The locking

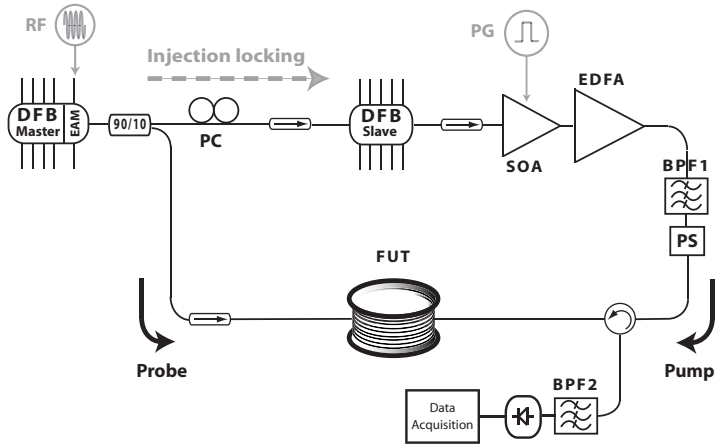

Figure 4.7: Schematic diagram of the injection-locking based configuration. Master, Slave: distributed feedback lasers; EAM: electro-absorption modulator; SOA: semiconductor optical amplifier; EDFA: erbium-doped fibre amplifier; RF: radio-frequency generator; PG: pulse generator; PC: polarisation controller; PS: polarisation scrambler; BPF1, BPF2: optical band pass filters; FUT: fibre under test.

channel consists in a short fibre line used to lock the frequency of the slave laser on one modulation sideband of the free running master laser, by injecting a small quantity of the master radiation into the cavity of the slave laser. It must be pointed out that the main peculiarity of this configuration resides in the fact that the slave laser exhibits two cleaved facets without anti-reflexion coatings and built-in isolators, and that, consequently, the cavity is accessible through both facets, as shown in the figure.[5] In our case, the left facet is used for locking, while the right facet is used as the actual output of the laser.

[5]In previous experiments [76, 81], injection locking was performed through the built-in slave isolator in the blocking direction.

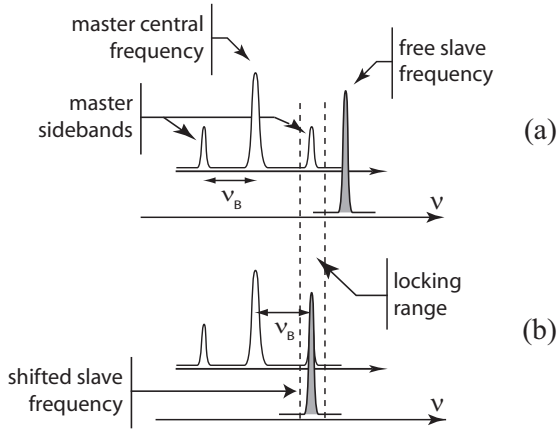

Figure 4.8: Schematic representation of the spectra of the master and slave lasers. (a) No locking: the free running slave laser lays outside the locking range. (b) Locking: the slave frequency is tuned within the locking range.

In order to maximise the interaction and avoid undesirable polarisation switching between TE and TM modes, the intracavity and injected fields polarisations are properly set using a polarisation controller (PC). The master laser is isolated up to 70 dB in order to prevent light coupling from the slave to the master and to protect master cavity from backreflected light. The output facet of the slave laser is isolated as well up to 80 dB to avoid backreflections at the fibre ends, which could lead to injurious self-injection locking.

The operating principle is schematically depicted in figure 4.8. In its free-running operation, the slave laser lays outside the locking range and is not influenced by the presence of the master radiation in its cavity. When the slave frequency is tuned within the locking range, in stead, the slave laser

locks very rapidly on the modulation sideband of the master. Thereafter, by simply changing the RF modulation frequency, the probe-pump detuning is changed accordingly. For standard values of the injection ratio (see figure 4.3), the frequency scanning range, that extends usually over a few hundred of MHz, is fully contained within the locking range, and the phase locking between master and slave is maintained throughout the scanning of the Brillouin gain curve.

This configuration provides two outputs with distinct optical frequencies, showing a beat note with the ideal stability given by the microwave generator, as shown in figure 4.9. These outputs can be simply delivered in two separate fibres and be used as different pump and probe signals. Unlike the sideband technique [34], no other idle wave is present in the set-up, except the residual modulation sideband with very low amplitude, which turns out to very significantly improve the noise characteristics of the technique.

The master laser was used to deliver the probe signal, and the light from the slave laser was boosted through an erbium-doped fibre amplifier (EDFA) to act as a pump in the Brillouin interaction. As described so far, the configuration makes possible the measurement of the Brillouin gain spectrum only integrated over the whole length of the fibre placed in the measurement channel. To make distributed measurements possible, the pump was simply gated through a semiconductor optical amplifier (SOA), driven by a pulse generator, and placed just before the EDFA.

Previous works investigated the possibility of taking profit of the dynamical characteristics of injection-locking, by performing the time coding of the Brillouin signal through the application of a short pulse on the driving current of the slave laser [79]. According to this approach, the pump (slave) laser

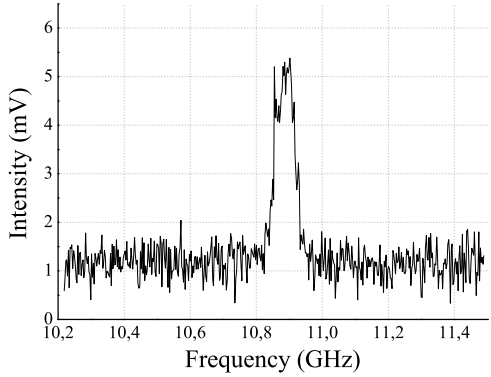

(a)

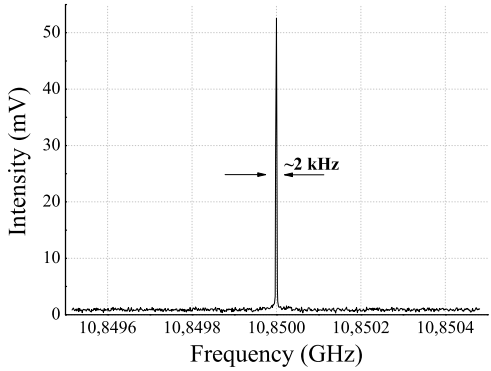

(b)

Figure 4.9: Electrical spectrum of the beat note between the master laser and the injection-locked slave laser. (a) Slave unlocked; (b) Slave locked.

is always on and its operating current is set, so that none of the emission lines (carrier+sidebands) of the master lie inside both the locking range and the Brillouin gain spectrum. When a current pulse is applied to the slave to move its free-running frequency into the locking range, it rapidly locks and the interaction takes place. When the pulse is stopped, the locking condition is no longer satisfied and the slave free-running frequency is again out of the locking range and of the Brillouin spectrum, so that no interaction is possible.

While promising and flexible over short distances, this technique is not entirely suitable for long-range operations, where high pump powers must be used (see section 4.5). The necessary requirement that the launched power is limited to below the threshold of any nonlinear effects becomes even more restrictive for CW pump powers. For these reasons, a different solution based on SOAs, in an optical gating configuration, was investigated. In the context of distributed Brillouin sensors, moreover, commercially available SOAs represent a good alternative to EOMs, since they are less expensive and can exhibit very high extinction ratios (> 35 dB).

To reduce the additive noise due to the amplified spontaneous emission, the output signal from the EDFA was filtered by an optical bandpass filter (BPF1) with a 3 dB bandwidth of 1 nm. A polarisation scrambler (PS) was additionally used to get rid of the random variations of the Brillouin gain due to the birefringence of the sensing fibre (see section 3.3). For very high pump pulse power operations, a second filter (BPF2) was also used in front of the detector, to filter the additional noise originated by the Rayleigh backscattered light from the Brillouin pump pulse (cf. section 5.2.2).

The distributed measurement is performed by acquiring the spatial (temporal) traces of the Brillouin gain for different

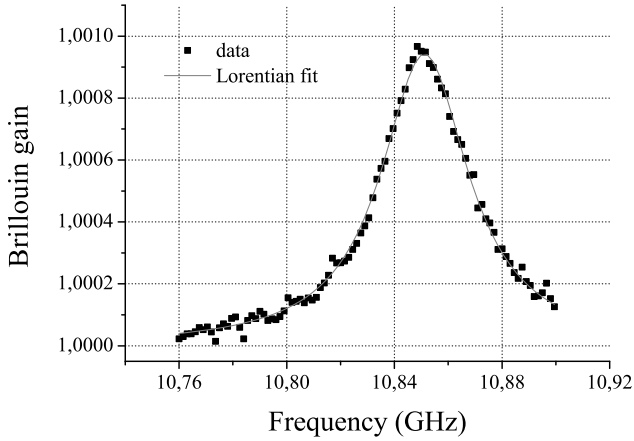

Figure 4.10: Brillouin gain spectrum measured in a sample of 50 m long γ-irradiated single-mode fibre (cf. section 5.1).

frequencies covering the Brillouin gain spectrum, $g_B(\nu_i, z)$. At each position z_k, the parameters of the Brillouin gain $g_B(\nu, z_k)$ are, then, extracted (through a Lorentzian nonlinear fit) and the Brillouin frequency shift and linewidth are fully retrieved.

In figure 4.10 we show the Brillouin gain spectrum measured in a sample of 50 m long γ-irradiated single-mode fibre (see section 5.1). This measurement was performed in very critical conditions, since the irradiated sample exhibited an optical attenuation equal to 170 dB/km. Nevertheless, despite the high noise level, the quality of the detected signal is quite representative of the efficiency of our sensing technique, in terms of SNR.

Figure 4.11 shows, in stead, a 3D representation of the Brillouin gain distribution, $g_B(\nu, z)$, and the processed Bril-

louin shift, $\nu_B(z)$, over the concatenation of a 200 m long single-mode fibre (SMF) and a 450 m long dispersion-shifted fibre (DSF), with a spatial resolution of 2m. In figure 4.11(a) we can distinguish the secondary Brillouin gain peak typically present in DSF, and in figure 4.11(b) the two different fibres are clearly shown. This measurement was effectuated without optical filters.

This set-up is very stable and intrinsically characterised by a very low noise level, which is imputable to the way pump and probe signals are generated and interact locally within the fibre. Distributed Brillouin sensors suffer, however, from some physical limitations to performances. We refer to [19] for a detailed discussion of the limitations due to the Raman scattering and the spectral broadening of the pump pulse. In the next section, we discuss the detrimental role played by another nonlinear effect: the modulation instability process.

4.5 Impact of modulation instability on the performances of distributed fibre sensors

We saw in the previous sections that BOTDA techniques involve the use of two counterpropagating optical waves, called respectively pump and probe waves, whose frequency separation must be kept constant and close to the Brillouin shift, ν_B, of the fibre. The most straightforward method to obtain these waves is through the modulation (at a frequency ν_B) of the light emitted by a single laser [34, 81]. In the spectral domain, this modulation process results in the creation of one or more lateral bands on both hands of the laser centre frequency: the use of one of these sidebands as Brillouin probe results in an

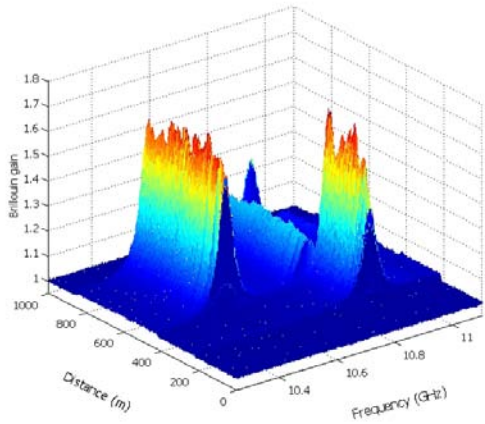

(a)

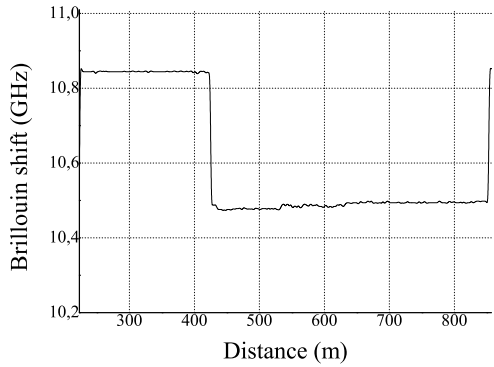

(b)

Figure 4.11: (a) 3D representation of the Brillouin gain distribution, $g_B(\nu, z)$, along two concatenated fibres. The DSF exhibits a secondary Brillouin peak gain. (b) Processed Brillouin shift, $\nu_B(z)$, clearly showing the the two different fibres.

ideal frequency stability between the pump and probe waves.

In order to maximise the sensor range and to improve the spatial resolution, high power pump pulses must be used, with the necessary requirement that the launched power is limited to below the threshold of any nonlinear effects that would, otherwise, be no longer negligible and would introduce errors in the detected Brillouin signal. In previous works, it was considered that the stimulated Raman scattering is the main effect which seriously limits the permissible input powers [82], and hence degrades long range measurements.

However, taking into account that the fibres used for sensing usually present anomalous dispersion at the pump wavelength and that the peak power of the pump pulse reaches typically 200-300 mW, the modulation instability (MI) process turns out to be the principal limiting effect, since it exhibits a much lower threshold. This was recently accounted for in sensors based on spontaneous Brillouin scattering [83], as a result of the spectral self-broadening of the pump pulse. In the case of BOTDA sensors based on stimulated Brillouin scattering, the effect of modulation instability is initiated entirely differently and is even more critical, since the probe wave can strongly seed the MI amplification process and this may consequently lead to an energy transfer from pump to probe. This results in a rapid pump depletion in the case of conventional SMFs, which manifests itself through a dramatic degradation of the sensor performances.

In this section we report on the experimental evidence of the detrimental effect of modulation instability in sensors based on stimulated Brillouin scattering [84].

4.5.1 Pump broadening

The experimental set-up used to investigate the impact of modulation instability on the performances of Brillouin distributed sensors is the same used to investigate FPU recurrence and is shown in figure 2.7 (on page 41).

We investigated and compared the effects of MI on two different fibres, respectively a 11.8 km-long SMF in the anomalous dispersion region ($\beta_2 = -21.92\ \mathrm{ps^2\,km^{-1}}$) and a 3.5 km-long DSF in the normal dispersion region ($\beta_2 = +7.65\ \mathrm{ps^2\,km^{-1}}$). A 20 ns pulse was used and the peak power was varied from 100 to 600 mW.

First, the output spectrum of spontaneous MI (with no modulation of the laser) was measured on an optical spectrum analyser for both fibres as a function of the input power. Figures 4.12 and 4.13 show the power spectra recorded at the far end of the fibres as the launched pulse peak power is increased. In the case of the SMF (figure 4.12) the effect of the MI becomes stronger as the power increases. The spectral lobes, which appear symmetrically on both sides of the central frequency, become broader and a significant amount of pump depletion is observed. In the case of the DSF (figure 4.13), according to theory (see section 2.3.1), the MI does not manifest itself by reason of its negative dispersion at 1.55μm, and the power spectrum shape stays unchanged. The pump depletion observed for high pulse peak powers is due to stimulated Raman scattering [82] present at 1660 nm, as shown in the inner plot.

A brief word of comment becomes here necessary. One could object that the results shown in figures 4.12 and 4.13 are not fully comparable on account of their different lengths (by approximately a factor 3). This is partly true in the sense that

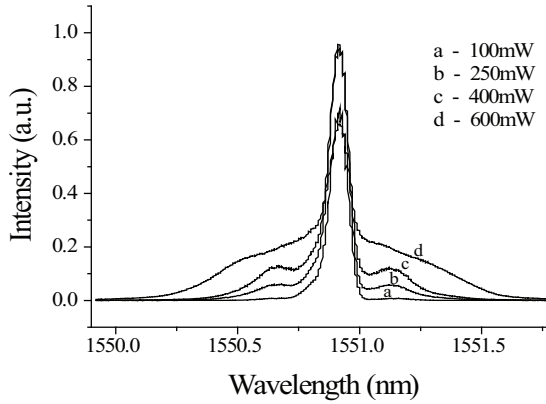

Figure 4.12: Measured power spectra of spontaneous MI for a SMF in the anomalous dispersion region ($\beta_2 < 0$). The input lightwave was a 20 ns pulse and the fibre was 11.8 km long.

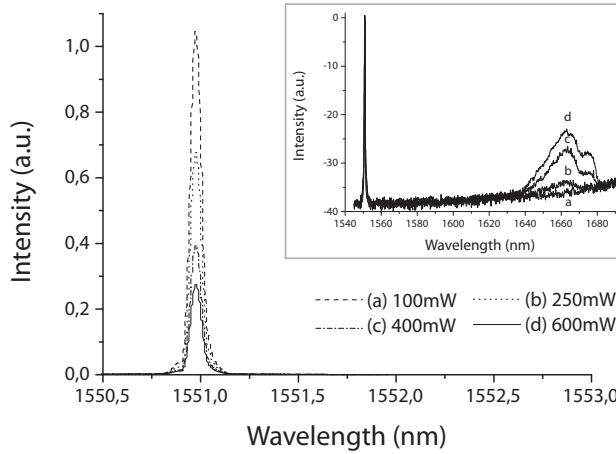

Figure 4.13: Measured power spectra of spontaneous MI for a DSF in the normal dispersion region ($\beta_2 > 0$). The input lightwave was a 20 ns pulse and the fibre was 3.5 km long. The inner plot shows the Raman scattering appearing at 1660 nm.

a pulse peak power of 600mW in the case of the DSF would correspond to a pulse peak power of approximately 200mW in the case of the SMF. Nonetheless, considering that the DSF exhibits a smaller effective area than the SMF by approximately a factor 2 (we remind that A_{eff} is related to the nonlinear fibre coefficient by an inverse proportionality law), the results depicted in figures 4.12 and 4.13 can be compared by means of approximately a factor 1.5. According to the example cited above, a pulse power of about 600mW for a DSF would correspond to approximately 400mW for a SMF.

Finally the expected absence of MI and, consequently, of pump broadening, suggest that the DSF can be more safely used with larger input powers, and that the long range operations are limited, actually, only by the Raman threshold.

4.5.2 Sidebands amplification

Beside a significant amount of pump broadening, a second critical effect of MI consists in the amplification of the sidebands resulting from the modulation of light at the Brillouin frequency. Figure 4.14 shows the theoretical MI gain spectra, discussed in section 2.3.1, on which the Brillouin sidebands have been superposed.

The MI gain spectrum changes along the fibre as a result of fibre loss and pump pulse power depletion. Using the expressions provided by Hasegawa and Tai [85], the spatially integrated gain, $G = \int_0^{z_m} g(z)dz$, can be parametrised as follows:

$$G = 1.6\frac{P}{\alpha\lambda A_{eff}}\sqrt{R}\left[\left(1-\frac{R}{4}\right)^{1/2} - \frac{\sqrt{R}}{2}\tan^{-1}\left(\frac{4}{R}-1\right)^{1/2}\right] \tag{4.18}$$

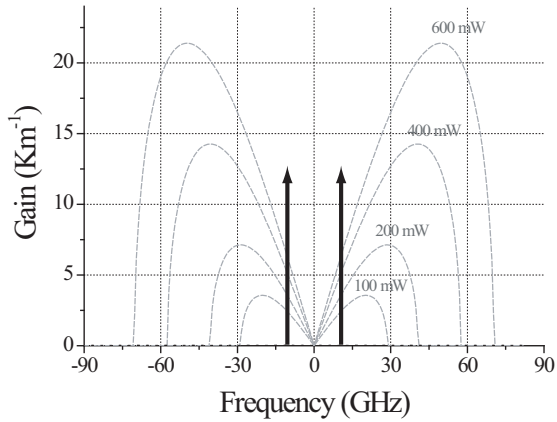

Figure 4.14: Modulation sidebands at the Brillouin frequency superposed to the MI gain spectra as a function of several power levels in SMF, at 1550 nm ($\beta_2 = -21.9$ ps^{2}km^{-1} and $\gamma = 1.78$ W^{-1}km^{-1}).

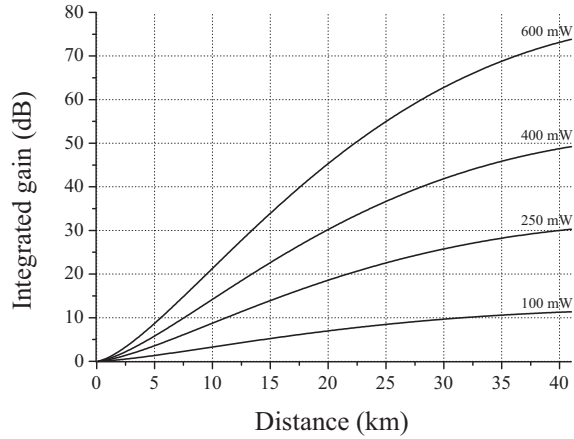

Figure 4.15: Spatially integrated gain of MI along a standard SMF as a function of distance, calculated at $\nu = \nu_B$ for several launched pulse peak powers ($\beta_2 = -21.9$ ps^{2}km^{-1} and $\gamma = 1.78$ W^{-1}km^{-1}).

by a quantity R defined by:

$$R = 1.1 \cdot 10^{-4} \frac{\nu^2 A_{eff}}{P} (-\lambda^3 D) \tag{4.19}$$

where P is the pulse peak power in mW, A_{eff} is the effective core area in μm^2, α is the fibre loss rate in dB/km, λ is the pump wavelength in μm, D is the dispersion coefficient in ps/nm/km, $z_m = -(2\alpha)^{-1} \ln(R/4)$ is the distance at which the MI gain becomes negative as a result of the fibre loss rate, and ν is the sideband frequency in GHz.

In figure 4.15 we computed the spatially integrated gain for the two sidebands plotted in figure 4.14 (at $\nu = \nu_B$) along a standard SMF as a function of distance and for several launched pulse peak powers. For a fibre length of 10 km the integrated gain is approximately equal to 8dB for a launch power of 250mW, and raises to about 20dB for a 600mW peak power.

To evaluate the MI effect existing in a standard SMF on the modulated laser, we set the sidebands intensity to 1/20 of the pump intensity and we recorded the output spectra at the far end of an 11.8 km SMF for different pump pulse peak power values. The results reported in figure 4.16 clearly show that, as far as the input pulse power is increased, the intensity of the pump wave gradually decreases and the sidebands undergo an amplification, to the detriment of the pump power.

The occurrence of pump depletion is clearly depicted in figure 4.17 where the left- and right-sideband intensities have been normalised by the pump wave intensity and reported as a function of the input pulse peak power. As shown, both sidebands drastically increase along with power, and for powers above 500 mW the sidebands are even greater than the depleted pump. Increasing further the input peak power, the interaction can exhibit the FPU recurrence (see section 2.3.3.2)

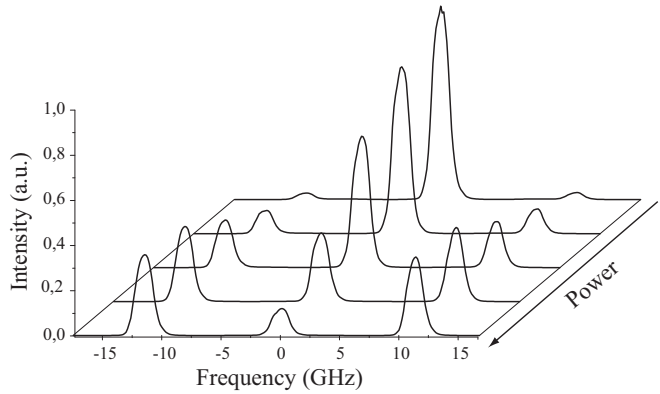

Figure 4.16: Experimental evolution of the output spectra recorded at the far end of an 11.8 km SMF for different pump pulse peak power values. The sidebands intensity was fixed to 1/20 of the pump intensity at the fibre input.

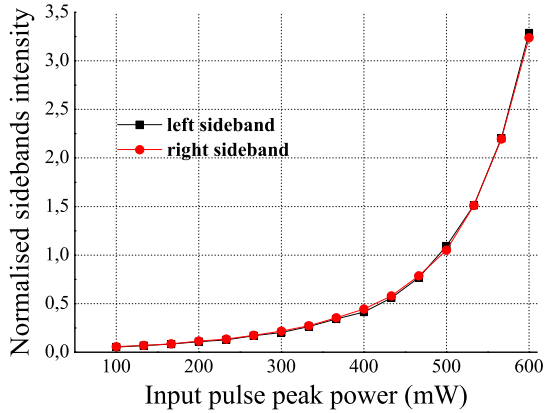

Figure 4.17: Brillouin sidebands intensities normalised by the pump wave intensity reported as a function of the input pulse peak power.

and the pump depletion can reach up to 100%. With such a strong depletion distributed measurements based on BOTDA techniques are definitely no longer possible.

It must be noticed, however, that modulation instability has no influence on the probe wave, as a result of its counter-propagating nature. By contrast, it can play an active role on any wave components which copropagate in the vicinity of the pump wave. This is actually the case of the residual modulation sidebands from optical filtering [34]: assuming filtering with a typical 20 dB of rejection ratio, the residual sidebands have sufficient intensity to undergo an amplification during the propagation within the fibre, and may be responsible for significant amounts of pump depletion in long-range operations.

4.5.3 Discussion

We investigated the undesirable effects of modulation instability in BOTDA sensors, with an aim of understanding the pump depletion occurring in the case of high pulse power operations. It turns out that not only the MI process is responsible for a significant amount of pump broadening, but that the probe wave lying within the MI gain spectrum, generated by the pump pulse, can also be amplified along a fibre exhibiting anomalous dispersion at the detriment of the pump power. SMFs seem, thus, to be inappropriate to be used at high powers to achieve high resolutions and range, as previously demonstrated for the systems based on spontaneous Brillouin scattering [83].[6]

To overcome the pump depletion due to MI, one solution consists in using single mode fibres exhibiting normal disper-

[6] At first glance MI may look more limitative in BOTDA, but actually it is not the case, since such systems require a lower pump power to observe Brillouin gain thanks to the stimulated process.

sion, in which case, we were not able to observe any appreciable changes in the sidebands intensity. One other solution could consist in substituting the intensity modulation by a phase modulation: ideally the presence of strong ripples due to SPM seeding the MI process would be avoided. Further experiments should be done to verify if the phase modulation is not rapidely converted into an intensity modulation due to the propagation within a dispersive fibre.

Bibliography

[1] T. Jarvilehto, "How to revise the theory of sensing?," *Psiloquy*, vol. 10, no. 8, 1999.

[2] X. Zubiri, *Sentient intelligence*. Xavier Zubiri Foundation of North America, 1999.

[3] A. J. Rogers, "Distributed optical fibre sensors for measurement of pressure, strain and temperature," *Phys. Rep.*, vol. 169, no. 2, pp. 99–143, 1988.

[4] E. Udd, *Fiber optic sensors: an introduction for engineers and scientists*. Wiley-Interscience Publication, John Wiley & Sons, 1991.

[5] I. Alasaarela, P. Karioja, and H. Kopola, "Comparison of distributed fiber optic sensing methods for location and quantity information measurements," *Opt. Eng.*, vol. 41, no. 1, pp. 181–189, 2002.

[6] A. D. Kersey, "A review of recent developments in fibre optic sensor technology," *Opt. Fiber Technol.: Mater., Devices Syst.*, vol. 2, pp. 291–317, 1996.

[7] J. Dakin and B. Culshaw, *Optical Fiber Sensors: Applications, analysis and future trends*, vol. 4. Artech House, London, 1997.

[8] K. Hotate, "Fiber sensor technology today," *Optical Fiber Technology*, vol. 3, no. 4, pp. 356–402, 1997.

[9] J. P. Dakin, "Distributed optical fibre sensors," *Crit. Rev.*, vol. CR44, pp. 162–199, 1992.

[10] M. Facchini, L. THévenaz, A. Fellay, and P.-A. Robert, "Tensile tests on optical fibre cables using distributed Brillouin analysis," *OFMC'99, 5th Optical Fibre Measurement Conference*, Nantes, 1999.

[11] A. Fellay, S. Le Floch, M. Facchini, L. Thévenaz, W. Scandale, and P.-A. Robert, "Brillouin gain curve measurements in fibres at cryogenic temperatures (3K-140K)," *OFMC'01, 6th Optical Fibre Measurement Conference*, Cambridge, 2001.

[12] S. Le Floch, *Etude de la diffusion Brillouin stimulée dans les fibres optiques monomodes standard. Application aux capteurs de température et de pression.* PhD thesis, Université de Bretagne Occidentale, 2001.

[13] M. Niklès, L. Thévenaz, A. Fellay, M. Facchini, P. Salina, and P.-A. Robert, "A novel surveillance system for installed fiber optics cables using stimulates Brillouin scattering," *Proc. of the 46th International Wire and Cables Symposium*, pp. 658–664, Philadelphia, 1997.

[14] L. Thévenaz, M. Facchini, A. Felly, M. Niklès, and P.-A. Robert, "Field tests of distributed temperature and strain measurement for smart structures," in *CLEO/Pacific Rim'01, Technical Digest I, 4th Pacific Rim Conference on Lasers and Electro-Optics*, pp. 490–491, Institute of Electrical and Electronics Engineers Inc., 2001.

[15] L. Thévenaz, M. Niklès, A. Fellay, M. Facchini, and P.-A. Robert, "Truly distributed strain and temperature sensing using embedded optical fibres," in *Proceedings of SPIE: 5th Annual International Symposium*

on Smart Structers and Materials, Conference 3330, (San Diego), pp. 301–314, March 2-4 1998.

[16] B. Culshaw, C. Michie, P. Gardiner, and A. McGown, "Smart structures and applications in civil engineering," *Proceedings of the IEEE*, vol. 84, no. 1, pp. 78–86, 1996.

[17] M. Facchini, *Distributed optical fiber sensors based on Brillouin scattering*. PhD thesis, Ecole Polythecnique Fédérale de Lausanne, 2002.

[18] M. Niklès, *La diffusion Brillouin dans les fibres optiques: étude et application aux capteurs distribués*. PhD thesis, Ecole Polytechnique Fédérale de Lausanne, 1997.

[19] A. Fellay, *Extreme temperature sensing using Brillouin scattering in optical fibres*. PhD thesis, Ecole Polytechnique Fédérale de Lausanne, 2003.

[20] M. K. Barnoski, M. D. Rourke, S. M. Jensen, and R. T. Melville, "Optical time domain reflectometer," *Appl. Opt.*, vol. 16, no. 9, pp. 2375–2379, 1977.

[21] M. Nakazawa and M. Tokuda, "Measurement of the fiber loss spectrum using fiber Raman optical-time-domain reflectometry," *Appl. Opt.*, vol. 22, no. 12, pp. 1910–, 1983.

[22] A. J. Rogers, "Polarization-optical time domain reflectometry: a technique for the measurement of field distributions," *Appl. Opt.*, vol. 20, no. 6, pp. 1060–1074, 1981.

[23] T. Kurashima, T. Horiguchi, H. Izumita, S. Furukawa, and Y. Koyamada, "Brillouin optical-fiber

time domain reflectometry," *IEICE Trans. Commun.*, vol. E76-B, no. 4, pp. 382–389, 1993.

[24] T. Horiguchi and M. Tateda, "BOTDA - Nondestructive measurement of single-mode optical fiber attenuation characteristics using Brillouin interaction: Theory," *J. Lightwave Technol.*, vol. 7, pp. 1170–1989, August 1989.

[25] K. Tsuji, K. Shimizu, T. Horiguchi, and Y. Koyamada, "Coherent optical frequency domain reflectometry for a long single-mode optical fiber using a coherent lightwave source and an external phase modulator," *IEEE Photon. Tech. Lett.*, vol. 7, no. 7, pp. 804–806, 1995.

[26] K. Hotate and O. Kamatani, "Reflectometry by means of optical-coherence modulation," *Electron. Lett.*, vol. 25, no. 22, pp. 1503–1505, 1989.

[27] S. J. Spammer, P. L. Swart, and A. A. Chtcherbakov, "Merged Sagnac-Michelson interferometer for distributed disturbance detection," *J. Lightwave Technol.*, vol. 15, no. 6, pp. 972–976, 1997.

[28] X. Fang, "A variable-loop sagnac interferometer for distributed impact sensing," *J. Lightwave Technol.*, vol. 14, no. 10, pp. 2250–2254, 1996.

[29] E. Brinkmeyer, "Analysis of the backscattering method for single-mode optical fibres," *J. Opt. Soc. Am.*, vol. 70, no. 8, pp. 1010–1012, 1980.

[30] A. Hartog and M. Gold, "On the theory of backscattering in single-mode optical fibers," *J. Lightwave Technol.*, vol. LT-2, no. 2, pp. 76–82, 1984.

[31] T. Horiguchi, T. Kurashima, and M. Tateda, "A technique to measure distributed strain in optical fibers," *IEEE Photon. Technol. Lett.*, vol. 2, no. 5, pp. 352–354, 1990.

[32] T. Horiguchi, K. Shimizu, T. Kurashima, M. Tateda, and Y. Koyamada, "Development of a distributed sensing technique using Brillouin scattering," *J. Lightwave Technol.*, vol. 13, no. 7, pp. 1296–1302, 1995.

[33] X. Bao, D. J. Webb, and D. A. Jackson, "32-km distributed temperature sensor based on brillouin loss in an optical fiber," *Opt. Lett.*, vol. 18, pp. 1561–1563, September 1993.

[34] M. Niklès, L. Thévenaz, and P.-A. Robert, "Simple distributed fiber sensor based on Brillouin gain spectrum analysis," *Opt. Lett.*, vol. 21, no. 10, pp. 758–760, 1996.

[35] C. Huygens, "Extrait d'une Lettre écrite de la Haye le 26 Fevrier 1665 [De la sympathie & concordance de deux Pendules suspendues d'une mesme perche]," *Le journal des sçavans*, no. XI, pp. 130–132, [16 Mars 1665].

[36] C. Huygens, *Oeuvres Complètes. Tome XVII*, pp. 183–187. Société Hollandaise des Sciences, La Haye, Martinus Nijhoff ed., 1932.

[37] A. E. Siegman, *Lasers.* University Science Books, Mill Valley, CA, 1986.

[38] M. Sargent III, M. O. Scully, and W. E. Lamb, *Laser physics.* Addison-Wesley, 1974.

[39] R. R. Ward, *The Living Clocks*. Alfred Knopf, NY, 1971.

[40] B. Razavi, "A study of injection locking and pulling," *IEEE J. Solid-State Circuits*, vol. 39, no. 9, September 2004.

[41] A. Pikovsky, M. Rosenblum, and J. Kurths, *Synchronization: a universal concept in nonlinear science*. Cambridge University Press, 2001.

[42] L. Glass and M. C. Mackey, *From clocks to chaos. The rythms of life*. Princeton University Press, Princeton, NJ, 1988.

[43] L. Rayleigh, "Acoustical notes," *Phil. Mag.*, vol. XIII, p. 316, 1907.

[44] H. Poincaré, "Sur le problème des trois corps et les équations de la dynamique," *Acta Mathematica*, vol. 13, pp. 1–270, 1890.

[45] E. V. Appleton, "The automatic synchronization of triode oscillator," *Proc. Cambridge Phil. Soc. (Math. and Phys. Sci.)*, vol. 21, pp. 231–248, 1922.

[46] B. van der Pol, "Forced oscillators in a circuit with non-linear resistance," *Phil. Mag.*, vol. 3, pp. 65–80, June 1927.

[47] B. van der Pol, "The nonlinear theory of electric oscillations," *Proc. IRE*, vol. 22, p. 1051, 1934.

[48] R. Adler, "A study of locking phenomena in oscillators," *Proc. IRE*, vol. 34, pp. 351–357, 1946.

[49] K. Kurokawa, "Noise in synchronized oscillators," *IEEE Transactions on Microwave theory and techniques*, vol. 16, no. 4, pp. 234–240, 1968.

[50] M. E. Hines, J.-C. R. Collinet, and J. G. Ondria, "FM noise suppression of an injection phase-locked oscillator," *IEEE Transactions on Microwave theory and techniques*, vol. 16, no. 9, pp. 738–742, 1968.

[51] H. L. Stover and W. H. Steier, "Locking of laser oscillators by light injection," *Appl. Phys. Lett.*, vol. 8, no. 4, pp. 91–93, 1966.

[52] C. J. Buczek, R. J. Freiberg, and M. L. Skolnick, "Laser injection locking," *Proc. IEEE*, vol. 61, no. 10, pp. 1411–1431, 1973.

[53] S. Kobayashi and T. Kimura, "Injection locking in AlGaAs semiconductor lasers," *IEEE J. Quantum Electron.*, vol. 17, no. 5, pp. 681–689, 1981.

[54] K. Otsuka and S. Tarucha, "Theoretical studies on injection locking and injection-induced modulation of laser diodes," *IEEE J. Quantum Electron.*, vol. 17, no. 8, pp. 1515–1521, 1981.

[55] S. Kobayashi, J. Yamada, S. Machida, and T. Kimura, "Single mode operation of 500 Mbit/s modulated AlGaAs semiconductor laser by injection locking," *Electron. Lett.*, vol. 16, pp. 746–748, 1980.

[56] D. J. Malyon and A. P. McDonna, "102 km unrepeated monomode fibre system experiment at 140 Mbit/s with an injection locked 1.52 μm laser transmitter," *Electron. Lett.*, vol. 19, pp. 445–447, 1983.

[57] H. Toba, Y. Kobayashi, K. Yanagimoto, H. Nagai, and M. Nakahara, "Injection-locking technique applied to 170 km trasnmission experiment at 445.8 Mbit/s," *Electron. Lett.*, vol. 20, pp. 370–371, 1984.

[58] K. Kikuchi, C.-E. Zah, and T.-P. Lee, "Amplitude-modulation sideband injection locking characteristics of semiconductor lasers and their applications," *J. Lightwave Technol.*, vol. 6, no. 12, pp. 1821–1830, 1988.

[59] L. Li, "Static and dynamic properties of injection-locked semiconductor lasers," *IEEE J. Quantum Electron.*, vol. 1994, no. 8, pp. 1701–1708, 30.

[60] J. Wang, M. K. Haldar, L. Li, and F. Mendis, "Enhancement of modulation bandwidth of laser diodes by injection locking," *IEEE Photon. Tech. Lett.*, vol. 8, no. 1, pp. 34–36, 1996.

[61] I. Petitbon, P. Gallion, G. Debarge, and C. Chabran, "Locking bandwidth and relaxation oscillations of an injection-locked semiconductor laser," *IEEE J. Quantum Electron.*, vol. 24, no. 4, pp. 148–154, 1988.

[62] K. Ywashita and K. Nakagawa, "Suppression of mode partition noise by laser diode light injection," *IEEE J. Quantum Electron.*, vol. QE-18, pp. 1669–1674, 1982.

[63] F. Mogensen, H. Olesen, and G. Jacobsen, "FM noise suppression and linewidth reduction in an injection-locked semiconductor laser," *Electron. Lett.*, vol. 21, pp. 696–697, 1985.

[64] M. R. Surette, D. R. Hjelme, R. Ellingsen, and A. R. Mickelson, "Effects on transients of injection

locked semiconductor lasers," *IEEE J. Quantum Electron.*, vol. 29, pp. 1046–1063, 1993.

[65] S. Piazzolla, P. Spano, and M. Tamburrini, "Small signal analysis of frequency chirping in injection-locked semiconductor lasers," *IEEE J. Quantum Electron.*, vol. QE-22, pp. 2219–2223, 1986.

[66] S. Mordiek, H. Burkhard, and H. Walter, "Chirp reduction of directly modulated semiconductor lasers at 10 Gb/s by strong CW light injection," *J. Lightwave Technol.*, vol. 12, no. 3, pp. 418–424, 1994.

[67] S. Kobayashi and T. Kimura, "Optical phase modulation in an injection locked AlGaAs semiconductor laser," *IEEE J. Quantum Electron.*, vol. QE-18, pp. 1662–1669, 1982.

[68] O. Lydoine, P. B. Gallion, and D. Erasme, "Modulation properties of an injection-locked semiconductor laser," *IEEE J. Quantum Electron.*, vol. 27, pp. 344–351, 1991.

[69] L. Li, "Small signal analysis of optical FM signal amplification by an injection-locked type semiconductor laser amplifier," *J. Lightwave Technol.*, vol. 10, pp. 477–481, 1992.

[70] L. Li and K. Petermann, "Small signal analysis of the optical-frequency conversion in an injection-locked semiconductor laser," *IEEE J. Quantum Electron.*, vol. 30, no. 1, pp. 43–48, 1994.

[71] L. Noël, D. Marcenac, and D. Wake, "Optical millimetre-wave generation technique with high efficiency,

purity and stability," *Electron. Lett.*, vol. 32, pp. 1997–1998, 21 1996.

[72] R. Lang, "Injection locking properties of a semiconductor laser," *IEEE J. Quantum Electron.*, vol. 18, no. 6, pp. 976–983, 1982.

[73] N. Schunk and K. Petermann, "Noise analysis of injection-locked semiconductor injection lasers," *IEEE J. Quantum Electron.*, vol. QE-22, pp. 642–650, 1986.

[74] P. Spano, S. Piazzolla, and M. Tamburrini, "Frequency and intensity noise in injection-locked semiconductor lasers," *IEEE J. Quantum Electron.*, vol. QE-22, pp. 427–435, 1986.

[75] A. Murakami, "Phase locking and chaos synchronisation in injection-locked semiconductor lasers," *IEEE J. Quantum Electron.*, vol. 39, no. 3, pp. 438–447, 2003.

[76] H. J. Troger, *Injection locking in semiconductor lasers.* PhD thesis, Ecole Polytechnique Fédérale de Lausanne, 1999.

[77] G. P. Agrawal and N. K. Dutta, *Semiconductor lasers.* Van Nostrand Reinhold, NY, 1993.

[78] K. Petermann, *Laser modulation and noise.* Kluwer Academic Publishers, 1991.

[79] L. Thévenaz, D. Alasia, S. Le Floch, and J. Troger, "Generation of high-quality signals for optical sensing using DFB injection locking lasers," *Proceedings of the SPIE - The International Society for Optical Engineering*, vol. 5502, no. 1, pp. 556–559, 2004.

[80] S. Afshar V., G. A. Ferrier, X. Bao, and L. Chen, "Effect of the finite extinction ratio of an electro-optic modulator on the performance of distributed probe-pump Brillouin sensor systems," *Opt. Lett.*, vol. 28, pp. 1418–1420, August 2003.

[81] L. Thévenaz, S. Le Floch, D. Alasia, and H.-J. Troger, "Novel schemes for optical signal generation using laser injection locking with application to Brillouin sensing," *Meas. Sci. Technol.*, vol. 15, pp. 1519–1524, August 2004.

[82] A. Fellay, L. Thévenaz, M. Facchini, and P.-A. Robert, "Limitation of Brillouin time-domain analysis by Raman scattering," *Proc. of the 15th Optical Fibre Measurement Conference, Nantes, France*, pp. 110–113, 1999.

[83] M. N. Alahbabi, Y. T. Cho, T. P. Newson, P. C. Wait, and A. H. Hartog, "Influence of modulation instability on distributed optical fibre sensors based on spontaneous Brillouin scattering," *J. Opt. Soc. Am. B*, vol. 21, no. 6, pp. 1156–1160, 2004.

[84] D. Alasia, M. González Herráez, L. Abrardi, S. Martin López, and L. Thévenaz, "Detrimental effect of modulation instability on distributed optical fibre sensors using stimulated Brillouin scattering," in *17th International Conference on Optical Fibre Sensors* (Marc Voet, Reinhardt Willsch, Wolfgang Ecke, Julian Jones, Brian Culshaw, ed.), pp. 587–590, Proceedings of SPIE Vol. 5855, SPIE, Bellingham, WA, 2005.

[85] A. Hasegawa and K. Tai, "Effects of modulational instability on coherent transmission systems," *Opt. Lett.*, vol. 14, no. 10, pp. 512–514, 1989.

Chapter 5

Original applications of distributed Brillouin sensing

In this chapter we report on an original application of distributed sensing to nuclear environments and on the observation of negative silica compaction in optical fibres. Omitting the well-known applications involving strain and temperature, extensively reviewed elsewhere [1–4], we emphasize in particular on the application of distributed measurements to the analysis of optical signals. In this context, we present a new generalised theoretical approach to the problem of sensing and report, eventually, on the first distributed measurement of the parametric gain in a single pump fibre-optics parametric amplifier (FOPA).

5.1 Application of distributed sensing to nuclear environments

Fibre optics sensing technology have been under evaluation for the past several years by the nuclear industry since it may bring promising alternatives to classical measurement techniques in harsh nuclear environments [5–8]. Distributed fibre sensing would allow, in particular, structural integrity monitoring of reactor containment buildings, nuclear waste repository survey and remote safety control of nuclear installations with significant benefits over conventional electronic instrumentation.

It is well known, however, that the exposure of optical fibres to ionising radiation results in a wavelength-dependent attenuation penalty. This effect limits the radiation acceptance level of intensity-based fibre optic sensors in nuclear environments and results in some radiation-induced errors which restrict the applicable area of such sensors. The potentialities of Raman distributed temperature sensors have already been studied in radiation environments [9–11], and special correction techniques for radiation-induced losses have been developed in order to take account of the differential radiation-induced attenuation for the Stokes and anti-Stokes lines which could cause incorrect temperature measurements. In contrast, the narrow wavelength encoding of the sensing information significantly helps to avoid the influence of the broadband radiation-induced loss, as already shown for fibre Bragg grating sensors [12].

Distributed sensors based on stimulated Brillouin scattering have actually an interesting potential for distributed strain and temperature monitoring in the nuclear industry. Since the sensing information is frequency-encoded, hence potentially radiation tolerant, it was interesting to study the radiation effects

on the Brillouin shift for application in ionising environments. In this section, we present novel results on the properties of the Brillouin gain spectrum under high gamma irradiation in a standard optical fibre up to very high gamma doses and the first observation - to our knowledge - of the compaction of silica in optical fibres.

5.1.1 Validation of the technique

We have investigated the effects of ionising radiation on the characteristics of the Brillouin gain spectrum in standard Ge-doped telecom single mode fibres (Lucent Allwave^{TM}). During this irradiation campaign, four fibre samples, cleaved to an identical length of 50 m, have been irradiated off-line in the underwater gamma irradiation facility 'BRIGITTE' of SCK ·CEN, Belgium (figure 5.1). The test chamber consists of a pressurised canister (figure 5.2), in which the samples are placed, which is then lifted down into the irradiation facility, so that the samples are surrounded by ten ^{60}Co γ-sources [13]. In this configuration the fibres have been irradiated at the same dose rate of 27 kGy·h^{-1} but with different exposure times to reach different total doses. The measured total dose absorbed by each fibre is listed in table 5.1.[1]

The fibre samples have been tested six weeks after the gamma irradiation campaign and have been monitored during several days.

We have first measured the total radiation-induced attenuation in the 1550 nm window for each sample using a commercial OTDR analyser. The results, summarized in table

[1]The absorbed dose is a measure of the energy deposited in a medium by ionising radiation. It is measured in *gray* (Gy) and corresponds to 1 J of energy per kg of matter.

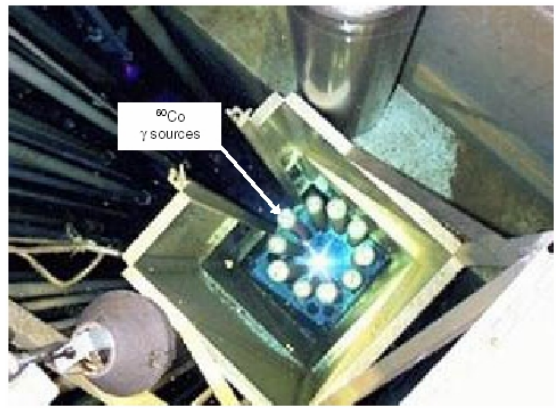

Figure 5.1: Photograph of BRIGITTE irradiation facility at SCK·CEN showing the ten ^{60}Co γ-sources. The open space inside the ring is the location where the sample canister is placed.

Fibre sample	Length (m)	Dose (MGy)
Reference	50	0
1	50	0.33
2	50	0.97
3	50	4.70
4	50	9.90

Table 5.1: Radiation dose experienced by the five samples of Lucent Allwave^{TM} single-mode fibres before measuring their Brillouin gain spectrum.

Figure 5.2: Photograph of the sample canister showing the inside structure with multiple shelves for sample storage. The canister is sealed against water ingress and maintained at constant temperature during the experiment, with dry nitrogen atmosphere at constant pressure.

5.2, are consistent with previous works [14]. Figure 5.3 shows and compares the spectral responses of the radiation-induced absorption measured by the cutback method, using a tungsten–halogen lamp and an optical spectrum analyser. This behaviour is typical of doped optical fibres when exposed to ionising radiation [14, 15]. However, despite the significant radiation-induced absorption, frequency-based systems like Brillouin distributed sensors still operate unbiased since the radiation-induced attenuation only affects the signal-to-noise ratio.

The effects of radiation on the properties of Brillouin scattering have been evaluated by a distributed measurement of the spectrum, in order to better discriminate the Brillouin characteristics of the irradiated fibre segments from those of the lead fibres. Figures 5.4 and 5.5 show the Brillouin central frequency (ν_B) and the Brillouin linewidth ($\Delta\nu_B$) as a function of the absorbed dose. The results presented here have been obtained by averaging several measurements carried out under the same conditions and at the same ambient temperature (T = 295.25 $\pm$ 0.05 K), in order to be free of systematic errors which could bias our data. The results are summarized in table 5.3 and show a small but clear dependence of the Brillouin scattering on the ionising radiation: frequency and linewidth increase *nonlinearly* as a function of the dose.

The reasons for this nonlinear behaviour will be discussed in details in the next subsection. What is quite important to stress here is that the frequency variation amounts to about 5 MHz for both central frequency and linewidth in the worst case (i.e., for the most irradiated sample). This corresponds approximately to a temperature change of about 5 K, or to a relative elongation of about $100\mu\epsilon$ for a total dose of about 10 MGy. It is useful to note, however, that the required radiation acceptance level for nuclear monitoring instrumentation is of

Fibre sample	Attenuation (dB/km)	Dose (MGy)
Reference	0.43	0
1	45	0.33
2	62	0.97
3	144	4.70
4	170	9.90

Table 5.2: Radiation-induced attenuation in the 1550 nm window measured using an OTDR analyser.

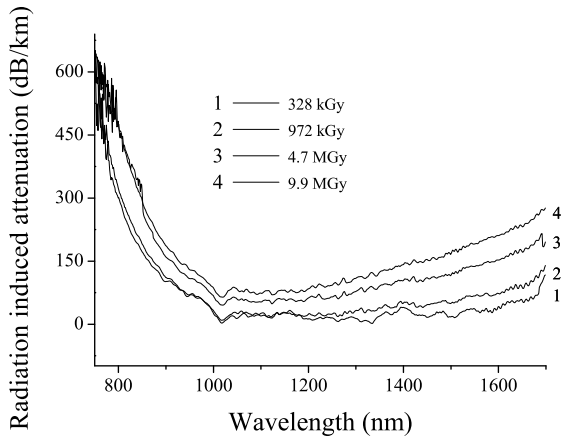

Figure 5.3: Spectral response of the radiation-induced attenuation. Curves have been normalized with respect to the spectrum of the reference fibre.

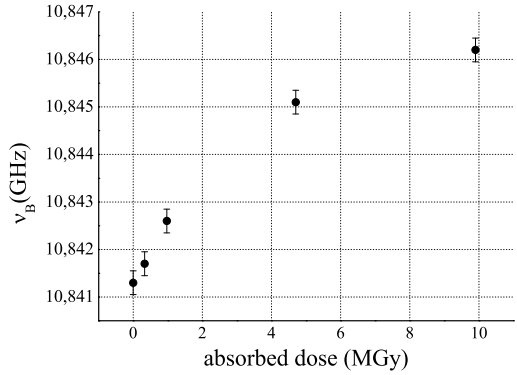

Figure 5.4: Brillouin central frequency ν_B measured as a function of the absorbed dose. All measurements were performed at a constant temperature (T = 295.25 ± 0.05 K).

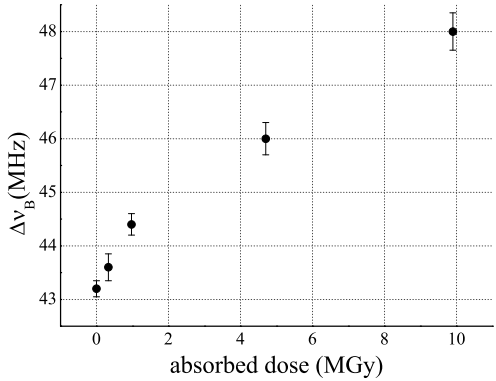

Figure 5.5: Brillouin FWHM linewidth $\Delta\nu_B$ measured as a function of the absorbed dose. All measurements were performed at a constant temperature (T = 295.25 ± 0.05 K).

Fibre sample	Brillouin frequency (GHz)		Brillouin linewidth (MHz)		Dose (MGy)
Reference	10.8413	10.8413*	43.2	43.2*	0
1	10.8417	10.8417*	43.6	43.5*	0.33
2	10.8426	10.8426*	44.4	44.2*	0.97
3	10.8451	10.8451*	46.0	46.0*	4.7
4	10.8462	10.8462*	48.0	48.1*	9.9

Table 5.3: Brillouin frequency and Brillouin linewidth as a function of the absorbed dose. The accuracy of the Brillouin central frequency is ±50 kHz and the accuracy of the half-linewidth is ±200 kHz. Starred values denotes the measurement of the Brillouin gain spectrum ten months later the irradiation campaign.

the order of 10–100 kGy at maximum. This means that, in practice, the radiation-induced shift of the Brillouin frequency cannot exceed 0.1 MHz (about 0.1 K on an equivalent temperature scale, and about $2\mu\epsilon$ on an equivalent strain deformation scale), so that it can be considered to be practically negligible in real applications.

Distributed sensors based on stimulated Brillouin scattering can, thus, be considered to be *radiation-tolerant* up to total doses of about 100 kGy, provided that the signal-to-noise ratio is kept acceptable, and constitute in this way an efficient monitoring tool for the nuclear facilities [16]. The sensing fibres can, moreover, be carefully pre-irradiated in order to minimise the effect of the radiation-induced shift (as adressed in the next section).

5.1.2 Observation of negative compaction in irradiated amorphous silica

The capability of Brillouin sensors to measure temperature or strain variations is intrinsically related to the physical origin of the Brillouin scattering, resulting from the change of the acoustic velocity with respect to variations of the silica density. In particular, the acoustic velocity can be related to the density by the following equation [17]:

$$v_a = \sqrt{\frac{E(1-\nu)}{(1+\nu)(1-2\nu)\rho}} \tag{5.1}$$

where E, ν and ρ represent respectively the Young modulus, the Poisson's number and the density of the fibre.

Since the Brillouin frequency ν_B is related to the acoustic velocity by the relation (see chapter 3):

$$\nu_B = 2nv_a/\lambda_0 \tag{5.2}$$

where n and λ_0 represent respectively the refractive index and the pump wavelength, a variation of the density inevitably induces a variation of the Brillouin frequency ν_B.

The results listed in table 5.3 show the shift of the Brillouin frequency ν_B due to ionisation radiation: this clearly tends to indicate a change in the silica density during the irradiation, by means of (5.1) and (5.2). It is well known that the radiation exposure of glasses and ceramics can cause important changes in the physical properties of the matter, such as density [18]. Depending on the type of silica, the irradiation can induce either a compaction or an expansion.

The most comprehensive experimental study of the *compaction* in bulk silica has been performed from the late 1950's

by Primak, who first investigated the physical mechanisms at the origin of radiation damages [19–22]. He observed that the products of irradiation can be described by a compacted vitreous state, which is characterised by a higher density with more disordered vitreous phase than vitreous silica. When silica is irradiated, knock-on displacements on the network atoms can occur as a result of collisions between incident particles or Compton electrons. In the same way, non-radiative decay of excitons (bound electron-hole pairs) formed by much lower energy photons can cause radiolytic displacements of the atoms. In either case, the irradiation creates displacements, electronic defects and breaks in the $\mathrm{Si}-\mathrm{O}-\mathrm{Si}$ bonds, which allow the structure to relax and fill the relatively large interstices existing in the interconnected network of silicon and oxygen atoms [19, 23].[2] A more recent review of compaction phenomena is available in [26].

In our case, the results depicted in figure 5.6 show that the ionising radiation induces a significant *negative compaction* (i.e., dilatation) of the optical fibres. These results are in excellent agreement with the pioneer work of Starodubtsev and Azizov [27], who first reported of an expansion caused by γ-irradiation. Primak and Kampwirth [22] suggested that the existence of impurities (Al or alkali) in the silica, fused from natural quartz, could be at the origin of the radiation-induced expansion. However, since the expansion has been observed in synthetic silicas with extremely low metallic impurity content, there must be an additional mechanism. Several studies have shown that a significant concentration of OH correlates with

[2] This phase, also known as the *metamict* phase, results from a radiation-induced loss of topological order [24]. The exact nature of this amorphous phase is still debated but has its origin in the change of the tetrahedral geometry and the ring-size arrangement distribution [25].

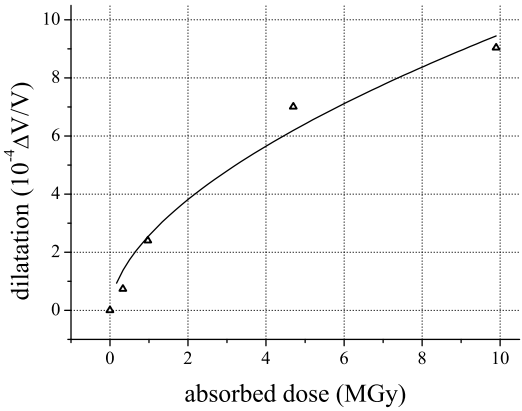

Figure 5.6: Dilatation due to ionisation radiation as a function of the absorbed dose. Experimental data (triangles) have been fitted with a power law (solid line): $\Delta V/V = AD^c$. The fitted constants read: $A = 2.577$ and $c = 0.566$.

radiation-induced expansion. When silica containing OH is irradiated, the radiolytic electrons and holes are trapped by the $Si - OH$, forming atomic hydrogen and non-bridging oxygen hole centres (NBOHCs) [28, 29]:

$$\equiv Si - OH + e^- + h^+ \rightarrow \equiv Si - O^\bullet + H^0 \qquad (5.3)$$

Following electron trapping, if the temperature is high enough, the atomic hydrogen diffuses away forming H_2, which can undergo a second reaction with the silica network [30]:

$$\equiv Si - O - Si \equiv +H_2 \rightarrow \equiv Si - OH + \equiv Si - H \qquad (5.4)$$

Large amounts of hydroxyls and hydrides are produced under these conditions, while NBOHCs and colour centre formation

are suppressed. If the expansion associated with reaction (5.4) is greater than any compaction associated with reaction (5.3) the net effect will be bulk expansion of the silica under irradiation [23].

Figure 5.6 shows, in addition, that the dose dependence of the dilatation obeys a power law as previously shown [23, 31]:

$$\frac{\Delta V}{V} = AD^c \tag{5.5}$$

where V is the volume, D the dose and A and c are constants. The exponent varies with the silica type and the nature of radiation. Primak and Kampwirth [19] found that $c = 1$ (linear growth) when silica was irradiated with neutrons (n^0), He^+, or D^+, whereas $c = 0.5 - 0.7$ when irradiated with H^+, electrons (e^-), or γ-rays [18]. By fitting our experimental data we have obtained $A = 2.577$ and $c = 0.566$, in agreement with previous results. Primak also showed that the sign of the compaction strongly depends not only on the silica type but also on the type and concentration of the dopants [20, 21].

The radiation induced compaction being an irreversible phenomenon, even for discontinued exposures to ionising radiation, the shift in the Brillouin frequency due to γ-rays is then permanently frozen in the fibre. This opens the way for preparing optical fibres with a reduced shifted Brillouin frequency by carefully choosing the dopant concentration and the fibre type, together with pre-irradiation. Measurements of the Brillouin gain spectrum done ten months after the irradiation campaign confirm the irreversibility of the compaction, the measured Brillouin frequencies and linewidths staying unchanged as shown in table 5.3.[3]

[3]The measurements have been held in the same experimental conditions than for the first measurement campaign.

Table 5.3 and figure 5.5 show the effect of the ionising radiation on the Brillouin linewidth $\Delta\nu_B$, as well. The reasons behind these variations are less clear than those about the Brillouin frequency, but they can be found in the structural change of the silica during the irradiation. Since the spectral broadening of the Brillouin spectrum is inversely proportional to the phonon lifetime ($\Delta\nu_B = 1/\pi\tau_p$), the results appear to confirm that the effect of irradiation is to introduce scattering centres into the fibre and lower the thermal phonon relaxation time [32–34]. The equivalent increase in the acoustic losses at high doses is certainly attributable to the appearance of radiation-induced defects, such as dislocations, interstitialcies, NBOHCs [35] and peroxy-radicals [36], which can be described by phenomenological models based on the existence of configurational tunnelling states, more simply described as two-level systems (TLS) [4,37]. Further investigations on different types of fibres with different types of dopants would be, anyhow, necessary to understand what really happens within the matter during irradiation. Nevertheless, this modest change in linewidth causes no impairment for the measurement of the Brillouin frequency ν_B, which is the essential information for sensing.

The results presented in this section represent - to our knowledge - the first observation and evidence of negative compaction due to ionising radiation in optical fibres [38]. Moreover, the use of the radiation-induced Brillouin shift as a tool of analysis can certainly bring new perspectives in the understanding of the compaction mechanisms and defect centres generation in irradiated amorphous silica. A short review of the origins of point defects in vitreous silica and of the radiation-induced damage processes is given in appendix A.

5.2 Application of distributed sensing to the analysis of optical signals

Distributed fibre sensors based on stimulated Brillouin scattering offer a unique capability for the analysis of optical signals and nonlinear phenomena in optical fibres. The local gain amplification inherent to the distributed measurement technique together with the back-scattered nature of the Brillouin scattering, which prevents possible mischievous interactions of either the pump or the probe[4] with the signal to be measured in the forward direction, make the BOTDA a versatile set-up and a useful tool of analysis for nonlinear optics.

During the past decade, on the ever increasing demand of the market for technical innovations, the efforts of the scientific community have been mainly concentrated on distributed sensing of different physical fields (strain, temperature, pressure, ...), with very successful and promising results; howbeit, few work has been carried out on the measurement of the spatial evolution of optical signals and the characterisation of nonlinear processes within the fibre. Horiguchi and Tateda [39] originally proposed and demonstrated the BOTDA technique as an efficient tool for the measurement of the optical fibre attenuation coefficient. Later, Thévenaz *et al.* [40] showed that an evaluation of the local birefringence of the fibre is also possible and, more recently, Song *et al.* [41] obtained an accurate mapping of local chromatic-dispersion with the best spatial resolution ever reported. Subías *et al.* [42] showed as well that, utilising the narrow spectral properties of the Brillouin spectrum, a full spectral analysis with very high resolution can also

[4]From this point on, the terms pump and probe denote exclusively the Brillouin pump and Brillouin probe of the BOTDA experiment, unless differently specified.

be performed.

In this section, we firstly present a generalised theoretical approach to the problem of localised sensing, and report, finally, on an original application of distributed sensing to the analysis of the parametric gain profile in a single-pump parametric amplifier.

5.2.1 Theoretical analysis

Generally, the optical fields exhibit a spatial evolution during their propagation within the fibre as a result of several nonlinear interactions occurring over the optical path. The optical signals of practical interest can be classified in two categories, according to the nature of their spatial dependence:

A. signals whose intensity variations are not issued from a gain (loss) interaction;

B. signals whose intensity variations result from an amplification (respectively attenuation) process.

A good example of the first case is represented by the power distribution of the FWM product fields generated from two strong copropagating pumps. By reason of the phase mismatch ($\Delta\beta$) between the waves involved in the interaction (see section 2.4.1), the corresponding power spatially oscillates according to the following law [43]: $P_{FWM}(z) = P_{FWM,0}\sin^2(\Delta\beta z/2)$, admitted that $P_{FWM,0}$ is sufficiently low [43, 44].[5] It is interesting to note that the nature of these intensity variations only depends on the phase-matching conditions of the interaction and is in no case related to a gain (loss) process. On the contrary, the spatial evolution of a signal which passes through a

[5]The factor $P_{FWM,0}$ actually depends on the pump powers and the phase mismatch $\Delta\beta$.

parametric amplifier (as it will be shown in section 5.2.2) fall in the second category.

Both these classes of signals can be efficiently retrieved as a function of location using the Brillouin optical time domain analysis in its pulsed pump-CW probe configuration (see section 4.2), but at rather diverse conditions.

In the first case (A), the BOTDA technique is used in a simple distributed Brillouin-amplifier configuration: the Brillouin pump is launched in the opposite direction to the signal to be measured (henceforth called the *measurand* signal) and we do not need to inject a CW probe in the fibre, the measurand signal acting itself as a probe for the Brillouin amplification interaction. In the second case (B), by contrast, to evince the spatial profile of an amplification (attenuation) process acting on a optical signal, both probe and pump must be used: the pulsed pump is then employed to seed the measurand process, while the spatial information is retrieved through the CW probe, which propagates in the opposite direction to the pump as in usual BOTDA. In principle, there is no reason why the probe should not be used as a seed for the interaction; in this particular condition, however, the spatial information can not be retrieved, the reasons of which are discussed below. For simplicity, the two cases are considered separately.

5.2.1.1 Case A

The optical waves involved in the analysis process are depicted in figure 5.7. We assume that the pump wave $P_p(z)$ propagates forward in the form of a narrow square pulse of width Δz, whereas the measurand signal $P_S(z)$ exhibits arbitrary spatial profile and propagates in the backward direction.

The pump pulse can be mathematically described by a rect-

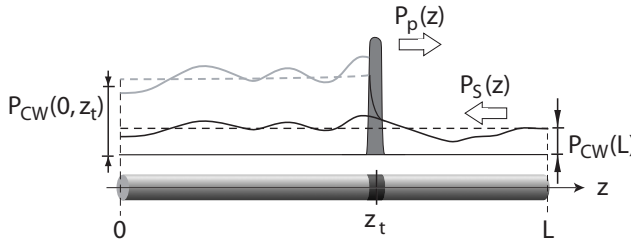

Figure 5.7: Brillouin analysis of optical signals. Case A. $P_S(z)$ can be decomposed into a CW part (black dashed line) and a varying envelope (black solid line). After the interaction with the pump pulse, the CW part (dashed grey line) and the envelope of the signal (solid grey line) are locally amplified.

angle function $\Pi_{\Delta z}(z)$ defined as follows:

$$\Pi_{\Delta z}(z) = u(z) - u(z - \Delta z) \tag{5.6}$$

where $u(z)$ represents the Heaviside function (see page 23).[6]

The measurand signal $P_S(z)$ can be decomposed as:

$$P_S(z) = P_{CW}(z)[1 + s(z)] \tag{5.7}$$

where $P_{CW}(z)$ denotes the mean continuous wave[7] part and $s(z)$ represents the varying envelope of the signal.

The forward-travelling pump pulse (launched at $t = 0$) crosses the signal at a generic position z_t and produces local Brillouin gain, which is detected at the input of the fibre ($z = 0$) at time $t = 2z_t/v_g$, with v_g the group velocity in the fibre (see section 2.2.2).

[6]Square pulses are used here for mathematical convenience; the approach can, anyway, be extended to any arbitrary pulse shape.

[7]The spatial dependence of the CW keeps into account the optical attenuation of the signal during its propagation within the fibre.

We assume then that the Brillouin interaction actually occurs between the pulsed pump, $P_p(z)$, and the CW part of the measurand signal, $P_{CW}(z)$, and that the envelope part, $s(z)$, only acts like a perturbation to the mean value. On the basis of the equations (3.53) introduced in Chapter 3, we can write two equations describing the evolution of the pulse peak power and of the continuous wave, and we associate the rectangle function $\Pi_{\Delta z}(z - z_t)$, which keeps account of the localised nature of the interaction, to the Brillouin gain, g_B. Assuming that the probe power is sufficiently low such that the interaction entirely occurs in conditions of non-depleted pump, and considering the optical attenuation, the process is completely modelled by the following equations:

$$P_p(z) \approx P_p(0)e^{-\alpha z} \tag{5.8a}$$

$$\frac{\partial P_{CW}}{\partial z} = -\frac{g_B}{A_{eff}}\Pi_{\Delta z}(z - z_t)P_p(z)[1 + s(z)]P_{CW}(z) + \alpha P_{CW}(z) \tag{5.8b}$$

By integration over the whole length of the fibre we obtain:

$$\begin{aligned} P_{CW}(0, z_t) &= P_{CW}(L)e^{-\alpha L} \cdot \\ &\quad \cdot e^{\left(-\int_L^0 \frac{g_B}{A_{eff}} P_p(z)[1 + s(z)]\Pi_{\Delta z}(z - z_t)dz\right)} \\ &= P_{CW}(L)e^{-\alpha L} e^{\left(\frac{g_B}{A_{eff}} \int_{z_t}^{z_t + \Delta z} P_p(z)[1 + s(z)]dz\right)} \\ &= P_{CW}(L)e^{-\alpha L} e^{\left(\frac{g_B}{A_{eff}} P_p(0)e^{-\alpha z_t}[1 + s(z_t)]\Delta z\right)} \end{aligned} \tag{5.9}$$

where $P_{CW}(0, z_t)$ denotes the power detected at $z = 0$ as a function of the pulse location, and where we used the fact

that:

$$\int_{z_t}^{z_t+\Delta z} P_p(z)[1+s(z)]\,dz \approx P_p(z_t)[1+s(z_t)]\Delta z \tag{5.10}$$

for Δz sufficiently small to neglect the spatial variations of $s(z)$ and $P_p(z)$ over the pulse duration.

As long as the Brillouin gain is not too large, at a first-order of approximation, the equation (5.9) can be simplified as follows:

$$P_{CW}(0,z_t) \approx P_{CW}(L)e^{-\alpha L}(1+G_B e^{-\alpha z_t}) + \underbrace{G_B P_{CW}(L)s(z_t)e^{-\alpha(L+z_t)}}_{\Delta P_{CW}} \tag{5.11}$$

where $G_B = g_B P_p(0)\Delta z/A_{eff}$ represents the net Brillouin gain over Δz. If we neglect the attenuation terms, this expression reveals that the detected variations (ΔP_{CW}) of the CW power are essentially proportional to the localised value of the envelope signal:

$$\Delta P_{CW}(0,z_t) \propto s(z_t) \tag{5.12}$$

in agreement with the model presented in [41].

We have thus demonstrated that the intensity variations of a CW signal - not issued from a gain (loss) process - can be fully retrieved through BOTDA.

5.2.1.2 Case B

Signals subjected to an amplification process exhibit a spatial profile as a consequence of the gain (respectively loss) cumulated during their propagation inside the fibre, which can be investigated only through the use of a test (or seed) signal. In

the context of BOTDA, this means that, a priori, either the pulsed pump or the CW probe could be employed to seed the measurand process; in practice, though, the probe fails in this task and only the pump can be efficiently used to retrieve the spatial evolution of the process.

We first consider the case involving the CW probe as a test signal (see figure 5.8(a)). If $\psi(z)$ denotes the cumulative gain (loss) as a function of position - this case includes also the optical attenuation - the equation governing the evolution of the probe wave reads:

$$\frac{\partial P_S}{\partial z} = -\frac{g_B}{A_{eff}}\Pi_{\Delta z}(z - z_t)P_p(z)P_S(z) \mp \psi(z)P_S(z) \quad (5.13)$$

with $P_p(z) \approx P_p(0)$, in non-depleted pump regime. Integrating over the whole length of the fibre we obtain:

$$\begin{aligned} P_S(0, z_t) &= P_S(L)e^{\mp\int_L^0 \psi(z)\,dz} e^{-\int_L^0 \frac{g_B}{A_{eff}}P_p(z)\Pi_{\Delta z}(z - z_t)\,dz} \\ &= P_S(L)e^{\mp\int_L^0 \psi(z)\,dz} e^{\frac{g_B}{A_{eff}}P_p(0)\Delta z} \end{aligned} \quad (5.14)$$

where the dependence on the local position z_t has disappeared in the right-hand side. This means that the measurand process acts on the probe in a completely independent way from the localised Brillouin interaction, and that a CW probe is not able to sense the spatial profile of such a process.

We consider now the case involving the pulsed pump as a test signal (see figure 5.8(b)). Assuming that the probe power is sufficiently low such that the interaction entirely occurs in

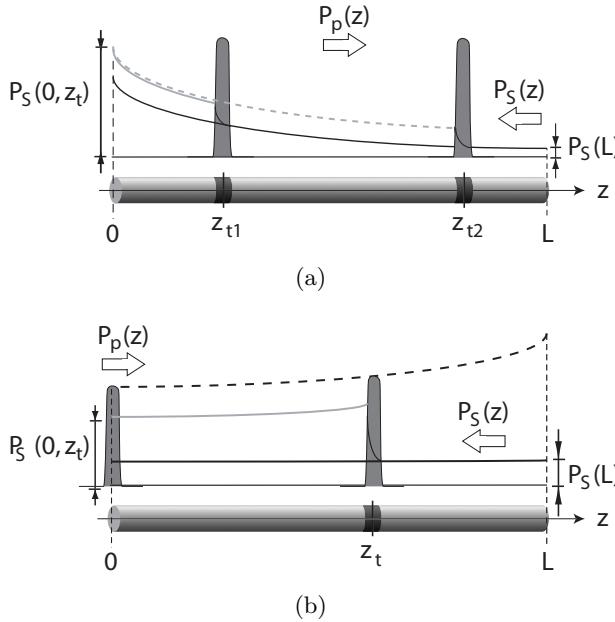

Figure 5.8: Brillouin analysis of signals. Case B. (a) The CW probe is used to seed the measurand process and experiences overall amplification: no local information can be retrieved. (b) The pulsed pump seeds the measurand process and experiences local amplification: spatial profile is fully retrievable.

conditions of non-depleted pump, and still neglecting the optical attenuation, the analysis process is completely described by the following equations:

$$\frac{\partial P_p}{\partial z} = \psi(z) P_p(z) \tag{5.15a}$$

$$\frac{\partial P_S}{\partial z} = -\frac{g_B}{A_{eff}} \Pi_{\Delta z}(z - z_t) P_p(z) P_S(z) \tag{5.15b}$$

By integrating (5.15a) over a generic distance z, and (5.15b) over the whole length of the fibre, we get:

$$P_p(z) = P_p(0) e^{\left(\int_0^z \psi(\zeta)\, d\zeta \right)} \tag{5.16a}$$

$$P_S(0, z_t) = P_S(L) e^{\left(\frac{g_B}{A_{eff}} P_p(z_t) \Delta z \right)} \tag{5.16b}$$

and inserting (5.16a) into (5.16b) we finally obtain:

$$P_S(0, z_t) = P_S(L)\ e^{\left(G_B e^{\left(\int_0^{z_t} \psi(\zeta)\, d\zeta \right)} \right)} \tag{5.17}$$

which, for small Brillouin gains ($G_B \ll 1$), reduces to:

$$P_S(0, z_t) \approx P_S(L) + G_B P_S(L) e^{\int_0^{z_t} \psi(\zeta)\, d\zeta} \tag{5.18}$$

This expression reveals that the detected variations of the CW probe power in logarithmic scale are essentially proportional to the definite integral of the cumulative gain (loss) measured at each position z_t within the fibre:

$$\ln \Delta P_S(0, z_t) \approx \ln[G_B P_S(L)] + \int_0^{z_t} \psi(\zeta)\, d\zeta \tag{5.19}$$

By simple derivative with respect to the localised position, it is possible to retrieve the exact distribution of the cumulative gain over the whole fibre length:

$$\frac{d \ln \Delta P_S(0, z_t)}{dz_t} \approx \psi(z_t) \tag{5.20}$$

We have thus demonstrated that the spatial profile of signals resulting from an amplification (attenuation process) is fully retrievable through BOTDA.

In literature, the only existing example utilising this kind of optical analysis process is the original paper of Horiguchi and Tateda [39]. They demonstrated that BOTDA is an efficient tool for the measurement of the optical fibre attenuation coefficient and they successfully (maybe unconsciously) used the pump pulse to seed the attenuation process. According to our development, the optical attenuation can be retrieved by simply setting: $\psi(z) = -\alpha$. No other applications involving distributed measurement of amplification processes have been reported since then. Only recently, the first spatial analysis of the parametric gain in a fibre-optics parametric amplifier has been demonstrated, and we report on this original application in the following section.

5.2.2 Distributed analysis of parametric gain in fibre-optics parametric amplifiers

Numerous recent studies have shown the extremely high potential of fibre-optics parametric amplifiers (FOPAs) for the realisation of future ultra-high bandwidth optical communication devices [45]. FOPAs are based on an efficient four-wave mixing (FWM) process between one or two pump waves and co-propagating signal and idler waves. Since the efficiency

of the FWM process relies on the phase-matching condition between these four interacting waves, it is essential to tune the pump wavelength near the zero-dispersion wavelength, λ_0, of the amplifying fibre, in order to maximize the overall gain bandwidth. In such conditions, usual FWM and modulation instability theories predict an exponential-like amplification for FOPA gain when the phase-matching condition is satisfied (see section 2.4.2).

In practice, though, the random fluctuations of λ_0 - which originate from the random variations of the optogeometric properties of the fibre during its fabrication - locally modify the phase matching conditions between pump(s), signal and idler and dramatically affect the properties of the parametric gain spectrum. The performances of FOPAs become, then, strongly phase-sensitive once the idler wave is generated, leading to a reduction of both the achievable parametric gain and bandwidth [46–48]. A distributed measurement of the FOPA gain along the optical fibre could, thus, reveal possible imperfections in the behaviour of the amplifier and, at the same time, provide useful informations on the longitudunal distribution of the zero-dispersion wavelength (ZDW) [43].

A technique based on gain optical time domain reflectometry (GOTDR) was recently proposed to characterise the gain of a FOPA as a function of the position along the fibre [49]: a pulse is launched through the amplifier in the opposite direction and the amplification on the weak Rayleigh backscattered light from the pulse is recorded. Nevertheless, this technique only brings informations on the accumulated gain from randomly distributed Rayleigh sources within the FOPA. By contrast, we propose and demonstrate an alternative and efficient approach to probe the localised small-signal parametric gain, using Brillouin optical time domain analysis [50].

5.2.2.1 Experimental set-up

The experimental set-up is shown in figure 5.9. The upper part is responsible for the generation of the continuous wave FOPA pump, whereas the lower part reproduces the BOTDA set-up presented in section 4.4.

The light emitted by a tunable laser (TL) is phase modulated by a pseudo-random binary sequence (PRBS) generator at the frequency of 3.5 GHz, in order to broaden the Brillouin gain bandwidth of the fibre and increase the threshold for noise generated by the stimulated Brillouin scattering (see section 3.2.4). The output of the modulator is then boosted by a 33 dBm-EDFA and filtered by an optical bandpass filter with a 3 dB bandwidth of 1 nm.

The FOPA pump and the BOTDA pump are then combined together using a 99:1 coupler, such that the pulsed Brillouin pump seeds the FOPA amplification process and the theoretical analysis described in section 5.2.1.2 can be applied. Additional optical bandpass filters have been used at the output of the EDFAs, to reduce the additive noise due to the amplified spontaneous emission, and in front of the detector, to filter the Rayleigh backscattered light from the Brillouin pump pulse. Finally, a polarization scrambler (PS) is used to reduce the polarisation-dependence of the Brillouin interaction.

Inside the fibre, the BOTDA pump pulse copropagates with the FOPA CW pump and experiences a parametric gain (cf. page 52) given by:

$$G_s(z) = \frac{P_p(z)}{P_p(0)} = 1 + \left[\frac{\gamma P_0}{g}\sinh(gz)\right]^2 \tag{5.21}$$

where $P_p(z)$ is the pump peak power as a function of location, g is the parametric gain coefficient and γ the nonlinear coeffi-

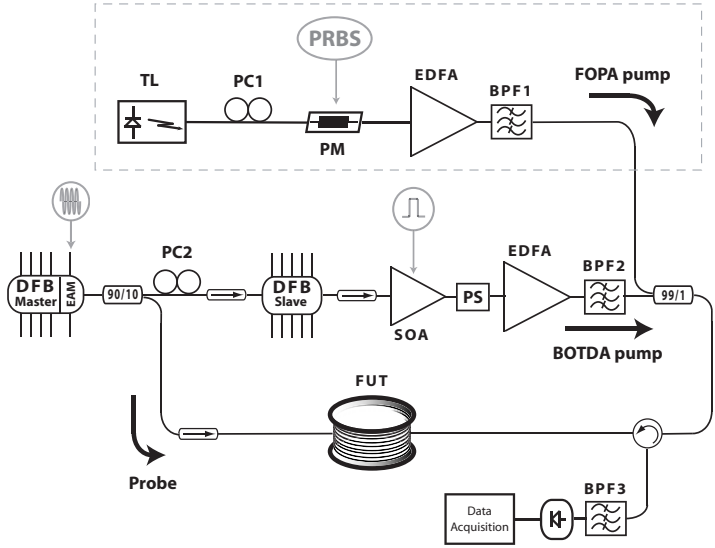

Figure 5.9: Experimental set-up for the measurement of parametric gain in fibres. TL: tunable laser; PC1, PC2: polarisation controllers; PM: phase modulator; PRBS: pseudo random binary sequence generator; BPF1, BPF2, BPF3: optical band pass filters; PS: polarisation scrambler.

cient. As discussed in section 2.4.2, for small gains (such that $g \approx 0$), the amplifier operates in the parabolic regime:

$$G_s(z) \approx 1 + (\gamma P_0 z)^2 \tag{5.22}$$

whereas for perfect phase matching ($\kappa \approx 0$) the amplifier operates in the exponential regime:

$$G_s(z) \approx \frac{1}{4} e^{2\gamma P_0 z} \tag{5.23}$$

The spatial profile of the parametric gain is then retrieved at

	HNLF	DSF
Length (km)	0.49	3.1
λ_0 (nm)	1553	1549.5
γ ($W^{-1}km^{-1}$)	11.2	2

Table 5.4: Generation of parametric gain in optical fibres: characteristics of the measured fibres.

each position along the fibre through the CW probe by means of the equation (5.18) by simply setting:

$$\psi(z) = \frac{d \ln G_s(z)}{dz} \tag{5.24}$$

By tuning the CW probe at a frequency $v_S = v_p + v_B$, we operate the distributed measurement using Brillouin loss instead of Brillouin gain, and ensure that no BOTDA pump depletion takes place during the interaction.

5.2.2.2 Results

Two different fibres were tested: a 490 m-long highly non linear fibre (HNLF) and a 3.1 km-long dispersion shifted fiber (DSF). The principal characteristics are summarised in table 5.4. During the whole measurement campaign, the probe wavelength was fixed to 1550.8 nm, and the BOTDA pump pulse width was set to 100 ns, corresponding to a spatial resolution of approximately 10 m. The measured FOPA pump power was 400 mW.

Figure 5.10(a) shows a typical evolution of the Brillouin loss spectra along the DSF fibre when the BOTDA pump is parametrically amplified. To be free of systematic errors which

could be introduced by possible variations of the Brillouin shift (due for example to inhomogeneities or local strains of the fibre), the experimental curves have been fitted for each position and only the maximum gain of each lorentzian curve has been retained. The net Brillouin losses for the cases where the FOPA pump is switched on and off are then depicted on Fig. 5.10(b), which clearly shows the parametric amplification of the BOTDA pump.

Figure 5.11 shows the derived FOPA local gain in linear units. In particular, figure 5.11(a) clearly shows both exponential gain ($\kappa = 0$) regime and small-gain parabolic ($g = 0$) regime, obtained by simply tuning the FOPA pump wavelength. We can see a fairly good agreement between the experimental results and the unsaturated gain (plotted in dashed lines) theoretically predicted by the equations (5.22) and (5.23), without saturation. Figure 5.11(b) reports instead the distributed FOPA gain in the HNLF for both forward and backward directions, with the FOPA pump wavelength close to λ_0: the profiles in the two directions show a similar gain but different longitudinal fluctuations. We can infer that the long scale (tens of meters) gain variations are due to the small κ or λ_0 fluctuations [48], and that they represent the signature of the phase-sensitive nature of FOPA.

Using the Brillouin optical time domain analysis in a novel configuration, we have been able for the first time - to our knowledge - to perform a distributed measurement of the parametric gain in a single-pump FOPA. The set-up could be easily extended to the study of other configurations, like two-pumps FOPAs, while the localised measurement of the parametric gain along a fibre opens up new means for the accurate mapping of ZDW fluctuations.

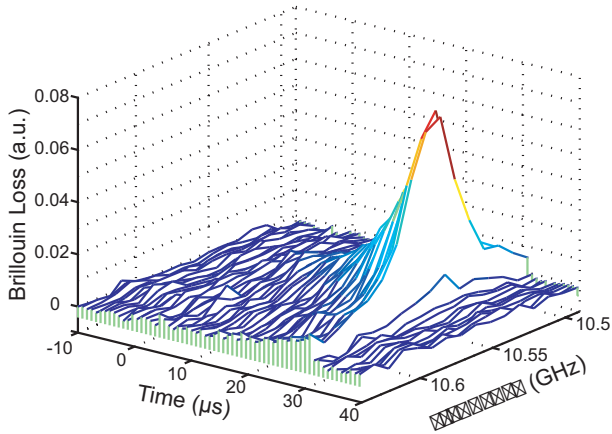

(a)

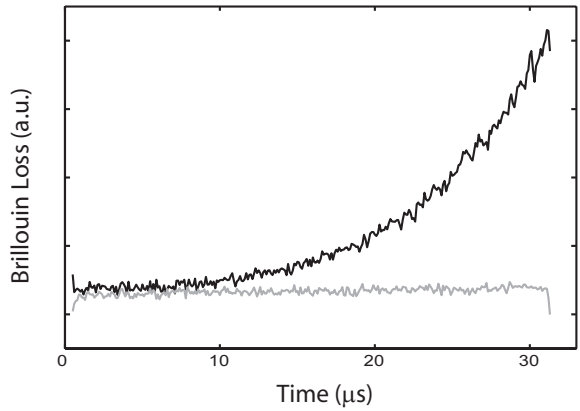

(b)

Figure 5.10: (a) Three dimensional plot showing the typical evolution of the Brillouin loss spectra along the DSF fibre when the BOTDA pump is parametrically amplified. (b) Profiles of the net Brillouin losses for the cases where the FOPA pump is switched on (black) and off (grey).

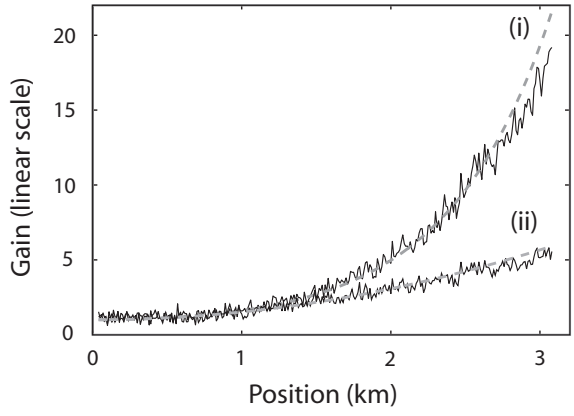

(a)

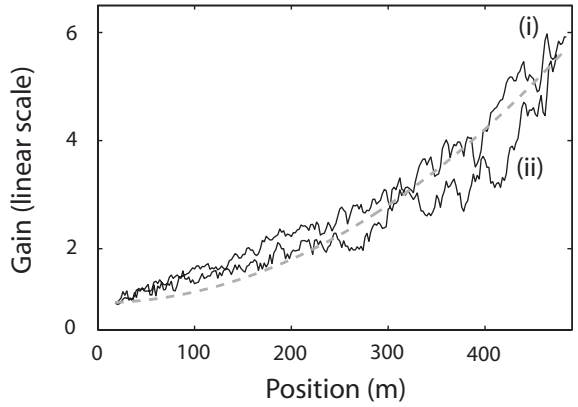

(b)

Figure 5.11: (a) Distributed analysis of the FOPA gain in a 3.1 km long dispersion shifted fibre (DSF) for two different gain regimes: i) exponential gain; ii) parabolic gain. (b) Distributed analysis of the FOPA gain in a 490 m long highly nonlinear fibre (HLNF) for both directions: i) backward; ii) forward.

Bibliography

[1] M. Niklès, *La diffusion Brillouin dans les fibres optiques: étude et application aux capteurs distribués.* PhD thesis, Ecole Polytechnique Fédérale de Lausanne, 1997.

[2] S. Le Floch, *Etude de la diffusion Brillouin stimulée dans les fibres optiques monomodes standard. Application aux capteurs de température et de pression.* PhD thesis, Université de Bretagne Occidentale, 2001.

[3] M. Facchini, *Distributed optical fiber sensors based on Brillouin scattering.* PhD thesis, Ecole Polythecnique Fédérale de Lausanne, 2002.

[4] A. Fellay, *Extreme temperature sensing using Brillouin scattering in optical fibres.* PhD thesis, Ecole Polytechnique Fédérale de Lausanne, 2003.

[5] E. Friebele, K. Long, C. Askins, M. Marrone, and D. Griscom, "Overview of radiation effects in fibre optics, in optical fibre sensing and systems in nuclear environments," *Proc. SPIE*, vol. 541, pp. 70–88, 1985.

[6] J. Berthold, "Overview of prototype fibre optic sensors for future application in nuclear environments, in optical fibre sensing and systems in nuclear environments," *Proc. SPIE*, vol. 2425, pp. 75–83, 1994.

[7] H. Henschel, O. Köhn, H. U. Schmidt, E. Bawirzanski, and A. Landers, "Optical fibres for high radiation dose environments," *IEEE Trans. Nucl. Sci.*, vol. 41, no. 3, pp. 510–516, 1994.

[8] A. Fernandez Fernandez, F. Berghmans, B. Brichard, and M. Decréton, "Towards the development of radiation-tolerant instrumentation data links for thermonuclear fusion experiments," *IEEE Trans. Nucl. Sci.*, vol. 49, pp. 2879–87, 2002.

[9] F. Jensen, E. Takada, M. Nakazawa, T. Kakuta, and S. Yamamoto, "Distributed Raman temperature measurement system for monitoring of nuclear power plant coolant loops," *Proc. SPIE*, vol. 2895, pp. 132–44, 1996.

[10] N. G. Craik, "Detection of leaks in steam lines by distributed fibreoptic temperature sensing (DTS)," in *Proc. IAEA Specialists' Meeting Monitoring and Diagnosis Systems to Improve Nuclear Power Plant Reliability and Safety*, Gloucester, UK, May, 1996.

[11] A. Kimura, E. Takada, K. Fujita, M. Nakazawa, H. Takahashi, and S. Ichige, "Application of a Raman distributed temperature sensor to the experimental fast reactor JOYO with correction techniques," *Meas. Sci. Technol.*, vol. 12, pp. 966–973, 2001.

[12] A. Fernandez Fernandez, B. Brichard, F. Berghmans, and M. Decréton, "Dose-rate dependencies in gamma-irradiated in-fibre Bragg gratings," *IEEE Trans. Nucl. Sci.*, vol. 49, pp. 2874–2878, 2002.

[13] A. Fernandez Fernandez, H. Ooms, B. Brichard, M. Coeck, S. Coenen, F. Berghmans, and M. Decréton, "SCK·CEN irradiation facilities for radiation tolerance assessment," *Proc. IEEE NSREC 2002, Radi-*

ation Effect Data Workshop (Phoenix, AZ), pp. 171–176, 2002.

[14] M. N. Ott, "Radiation effects data on commercially available optical fibre: database summary," in *IEEE Nuclear Science and Radiation Effects Conf. (Phoenix, AZ) (NSREC 2002, Data Workshop Proceedings)*, 2002.

[15] E. J. Friebele, C. G. Askins, and M. E. Gingerich, "Effect of low dose rate irradiation on doped silica core optical fibres," *Appl. Opt.*, vol. 23, no. 23, pp. 4202–4208, 1984.

[16] D. Alasia, A. Fernandez Fernandez, B. Brichard, L. Abrardi, and L. Thévenaz, "Study of the radiation effects on the properties of Brillouin scattering in standard Ge-doped optical fibres," in *17th International Conference on Optical Fibre Sensors* (Marc Voet, Reinhardt Willsch, Wolfgang Ecke, Julian Jones, Brian Culshaw, ed.), pp. 180–183, Proceedings of SPIE Vol. 5855, SPIE, Bellingham, WA, 2005.

[17] S. P. Timoshenko and J. N. Goodier, *Theory of Elasticity*, ch. 14. McGraw-Hill, NY, 1970.

[18] M. Rajaram and E. J. Friebele, "Effects of radiation on the properties of low thermal expansion coefficient materials: A review," *J. Non-Cryst. Solids*, vol. 108, no. 1, pp. 1–17, 1989.

[19] W. Primak and E. Edwards, "Radiation-induced dilatations in vitreous silica," *Phys. Rev.*, vol. 128, pp. 2580–2588, 1962.

[20] W. Primak and R. Kampwirth, "Impurity effect in the ionization dilatation of vitreous silica," *J. Appl. Phys.*, vol. 39, p. 6010, 1968.

[21] W. Primak, E. Edwards, D. Keiffer, and H. Szymanski, "Ionization expansion of compacted silica and the theory of radiation-induced dilatations in vitreous silica," *Phys. Rev.*, vol. 133, no. 2A, pp. A531–A535, 1964.

[22] W. Primak, "The compacted states of vitreous silica," in *Studies of Radiation Effects in Solids* (G. Dienes and L. Chadderton, eds.), Gordon and Breach, NY.

[23] J. A. Ruller and E. J. Friebele, "The effect of gamma-irradiation on the density of various types of silica," *J. Non-Cryst. Solids*, vol. 136, pp. 163–172, 1991.

[24] L. Hobbs and X. Yuan, "Topology and topological disorder in silica," in *Defects in SiO_2 and Related Dielectrics: Science and Technology* (G. Pacchioni, L. Skuja, and D. Griscom, eds.), ch. 2, pp. 37–71, Kluwer. Norwell, MA, 2000.

[25] B. Brichard, P. Borgermans, A. Fernandez Fernandez, K. Lammens, and M. Decréton, "Radiation effect in silica optical fiber exposed to intense mixed neutron-gamma radiation field," *IEEE Trans. Nucl. Sci.*, vol. 48, no. 6, pp. 2069–2073, 2001.

[26] E. Dooryhee, J.-P. Duraud, and R. Devine, "Radiation-induced defects and structural modifications," in *Structure and Imperfections in Amorphous and Crystalline Silicon Dioxide* (E. Dooryhe, J.-P. Duraud, and R. Devine, eds.), ch. 14, Wiley, NY, 2000.

[27] S. V. Starodubtsev and S. Azizov, "Change in linear dimensions of fused quartz during gamma irradiation," *Proc. Tashkent Conf. AEC-tr 6398*, vol. 1, p. 283.

[28] M. Stapelbroek, D. L. Griscom, E. J. Friebele, and G. H. Sigel Jr., "Oxygen-associated trapped-hole centers in high-purity fused silicas," *J. Non-Cryst. Solids*, vol. 32, pp. 313–326, 1979.

[29] T. Bakos, S. N. Rashkeev, and S. T. Pantelides, "Optically active defects in SiO_2: The nonbridging oxygen center and the interstitial OH molecule," *Phys. Review B*, vol. 70, p. 075203, 2004.

[30] J. E. Shelby, "Radiation effects in hydrogen-impregnated vitreous silica," *J. Appl. Phys.*, vol. 50, no. 5, pp. 3702–3706, 1979.

[31] C. B. Norris and E. P. EerNisse, "Ionization dilatation effects in fused silica from 2 to 18-keV electron irradiation," *J. Appl. Phys.*, vol. 45, no. 9, pp. 3876–3882, 1974.

[32] B. D. Silverman, "Ultrasonic attenuation in imperfect insulating crystals," *Progress of Theoretical Physics*, vol. 39, no. 2, pp. 245–69, 1968.

[33] M. Thuraisingham and R. Stephens, "Effects of gamma-irradiation on the ultrasonic attenuation in quartz and tourmaline at low temperatures," *Proc. of the 5th Int. Conf. on Internal Friction and Ultrasonic Attenuation in Crystalline Solids*, pp. 308–313, 1975.

[34] R. Nava, "Phonon contribution to the ultrasonic attenuation in neutron-irradiated quartz," *Phys. Review B*, vol. 31, no. 8, pp. 5497–5499, 1985.

[35] N. Jiang, J. Qiu, A. Ellison, and J. Silcox, "Fundamentals of high-energy electron-irradiation-induced modifications of silicate glasses," *Phys. Review B*, vol. 68, p. 064207, 2003.

[36] A. H. Edwards and W. B. Fowler, "Theory of the peroxy-radical defect in a-SiO_2," *Phys. Review B*, vol. 26, no. 12, pp. 6649–6660, 1982.

[37] A. Vanelstraete and C. Laermans, "Tunneling states in neutron-irradiated quartz: Measurements of the ultrasonic attenuation and velocity change," *Phys. Review B*, vol. 42, no. 9, pp. 5842–5854, 1990.

[38] D. Alasia, A. Fernandez Fernandez, B. Brichard, L. Abrardi, and L. Thévenaz, "The effects of gamma-radiation on the properties of Brillouin scattering in standard Ge-doped optical fibres," *Meas. Sci. Technol.*, vol. 17, pp. 1091–1094, May 2006.

[39] T. Horiguchi and M. Tateda, "BOTDA - Nondestructive measurement of single-mode optical fiber attenuation characteristics using Brillouin interaction: Theory," *J. Lightwave Technol.*, vol. 7, pp. 1170–1989, August 1989.

[40] L. Thévenaz, M. Facchini, A. Fellay, M. Niklès, and P.-A. Robert, "Evaluation of local birefringence along fibres using Brillouin analysis," in *Conference Digest, OFMC'97, 4th Optical Fibre Measurement Conference*, (Teddington UK), pp. 82–85, Sept. 29 - Oct. 1 1997.

[41] K. Song, M. González Herráez, and L. Thévenaz, "Mapping of chromatic-dispersion distribution along optical fibers with 20-m spatial resolution," *J. Lightwave Technol.*, vol. 23, no. 12, pp. 4140–4146, 2005.

[42] J. M. Subías Domingo, J. Pelayo, F. Villuendas, C. D. Heras, and E. Pellejer, "Very high resolution optical spectrometry by stimulated Brillouin scattering," vol. 17, no. 4, pp. 855–857, 2005.

[43] L. F. Mollenauer, P. V. Mamyshev, and M. J. Newbelt, "Method for facile and accurate measurement of optical fiber dispersion maps," *Opt. Lett.*, vol. 21, pp. 1724–1726, 1996.

[44] M. González Herráez, *Dessarrollo de técnicas non lineales para la medida de la distribución longitudinal de dispersión cromática en fibras ópticas monomodo.* PhD thesis, Universidad Politécnica de Madrid, 2004.

[45] J. Hansryd, P. Andrekson, M. Westlund, J. Li, and P.-O. Hedekvist, "Fiber-based optical parametric amplifiers and their applications," *IEEE JSTQE*, vol. 8, no. 3, pp. 506–520, 2002.

[46] M. Karlsson, "Four-wave mixing in fibers with randomly varying zero-dispersion wavelength," *J. Opt. Soc. Am. B*, vol. 15, no. 8, pp. 2269–2275, 1998.

[47] F. Yaman, Q. Lin, S. Radic, and G. Agrawal, "Impact of dispersion fluctuations on dual-pump fiber-optic parametric amplifiers," *IEEE Photon. Tech. Lett.*, vol. 16, no. 5, pp. 1292–1294, 2004.

[48] A. Mussot, E. Lantz, A. Durecu-Legrand, C. Simonneau, D. Bayart, T. Sylvestre, and H. Maillotte, "Zero-dispersion wavelength mapping in short single-mode optical fibers using parametric amplification," *IEEE Photon. Tech. Lett.*, vol. 18, no. 1, pp. 22–24, 2006.

[49] B.-E. Olsson, T. Torounidis, M. Karlsson, H. Sunnerud, and P. Andrekson, "OTDR technique for characterization of fiber optic parametric amplifiers," in *Proceedings of IEEE/OSA OFC*, (Anaheim, CA, USA), p. OWT3, 5-10 March 2006.

[50] A. Vedadi, D. Alasia, E. Lantz, H. Maillotte, L. Thévenaz, M. González-Herráez, and T. Sylvestre, "Brillouin optical time domain analysis od fiber optic parametric amplifiers," *to be presented at the 32nd European Conference on Optical Communication (ECOC 2006)*, Cannes, France, 24-28 September 2006.

Chapter 6

Conclusions

The distributed optical-fibre sensor based on the properties of Brillouin scattering is the central object of this thesis. A fully operative Brillouin optical time domain analysis (BOTDA) system, in a new and original configuration is presented. The key of the entire set-up resides in an innovative technique for the generation of optical signals based on the injection locking of two semiconductor lasers, instead of the traditional techniques using external modulators. This not only represents an innovative approach, but also brings significant improvements in terms of SNR and costs.

When intense pulses propagate along the fibre, however, the optical signals can be seriously degraded by several nonlinear interactions occurring within the fibre. Taking into account that the fibres used for sensing usually present anomalous dispersion at the pump wavelength, we point out that the nonlinear effect exhibiting the lowest threshold power is the modulation instability (MI) process. Its effect is twofold: on the one hand, it is primarily responsible for a significant amount of pump broadening, and on the other hand, the probe wave lying

within the MI gain spectrum generated by the pump pulse can experience an amplification along the fibre at the detriment of the pump power. From the study of the dynamical behaviour of MI, we could observe the Fermi-Pasta-Ulam (FPU) recurrence over few periods in very comfortable conditions, in good agreement with predictions of both theoretical and numerical models.

First intended as exploratory tests of feasibility for the application of Brillouin sensing to nuclear environments, we investigated the effects of ionising radiation up to very high total doses on the characteristics of the Brillouin gain spectrum in standard Ge-doped telecom single mode fibres. The measurement campaign has shown that distributed sensors based on stimulated Brillouin scattering are radiation-tolerant up to total doses of about 100 kGy, equivalent to the required radiation acceptance level for nuclear monitoring instrumentation, and constitute in this way an efficient monitoring tool for the nuclear facilities. The observation of a small but clear nonlinear dependence of the Brillouin frequency shift and Brillouin linewidth on the total dose constitutes the first observation - to our knowledge - of the negative compaction due to ionising radiation in silica-based optical fibres.

Distributed fibre sensors based on stimulated Brillouin scattering offer, as well, a unique capability for the analysis of optical signals and nonlinear phenomena in optical fibres. The local gain amplification inherent to the distributed measurement technique together with the back-scattered nature of the Brillouin scattering make the BOTDA a versatile set-up and a useful tool of analysis for nonlinear optics. We presented a new generalised theoretical approach to the problem of localised sensing and reported also on the first distributed measurement - to our knowledge - of the parametric gain in a single-pump

fibre-optics parametric amplifier (FOPA).

Original contributions

The original contributions of this work can be summarised by the following points:

1. We pointed out the serious impact of modulation instability in the performances of distributed sensors in high pulse powers operations, giving an explanation to the pump depletion occurring in long-range measurements;

2. We experimentally observed the FPU recurrence in good agreement with the predictions of both theoretical and numerical models;

3. We demonstrated the tolerance of distributed Brillouin sensors to the ionising radiation up to very high doses, and we extended the potential applications to the monitoring of harsh environments in the nuclear industry;

4. We consider the observation of the negative compaction in silica-based fibres as a major result from a fundamental physics point of view, since it validates the Brillouin analysis as a useful tool for investigating the nature of the products resulting from irradiation, and contributes to a better understanding of the fascinating nature of amorphous silica;

5. We discussed an original new approach to the problem of distributed sensing, validating the Brillouin analysis as a useful tool in nonlinear optics for investigating the spatial evolutions of optical signals and nonlinear processes;

6. We demonstrated the first distributed measurement of the parametric gain in a fibre parametric amplifier, opening up new means for the accurate mapping of ZDW fluctuations along the fibre.

Appendix A

On the nature of vitreous silica

This appendix aims to give short review of the radiation-induced damages in amorphous silica and owes mainly to the monographs of [1] and [2].

A.1 Physical properties of amorphous silica and point defects

Thermodynamic studies have shown that silica has a glass transition and a stable state at room temperature. The most generally adopted structural model of a-SiO_2 is the continuous random network (CRN) [3], which is based on the assumption that directional bonding of mixed covalent and ionic character applies both in crystalline and a-SiO_2. In this model, short-range order dominates, with each Si atom at the centre of a regular tetrahedron and four oxygen atoms at the vertexes forming O-Si-O angles of 109.5° (see figure A.1). Each oxygen

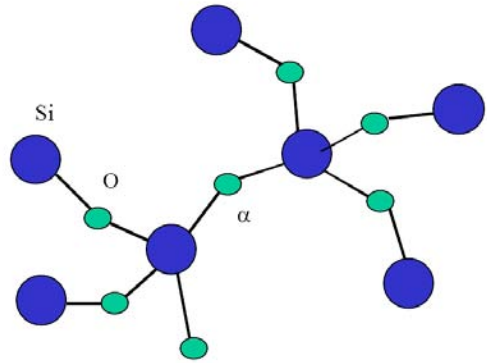

Figure A.1: Fragment of amorphous silica representing the atomic disposition and the linking between tethraedra ($\alpha = 109.5°$). From [2]

atom binds two silicon atoms and bridges two tetrahedra. This order is similar to that of most of the crystalline polymorph of SiO_2, but in the amorphous state the $Si-O-Si$ angle presents some variability, resulting in a random orientation distribution of SiO_4 tetrahedra. The amorphous matrix features, in this way, a crystalline-like short-range order, due to the close similarity between the structural units SiO_4 in both matrices. As a consequence, the electron structure and density of states are very similar, which yields, also in the amorphous state, a wide energy-gap between the valence and the conduction bands (nearly 8 eV for an ideal a-SiO_2 matrix). This explains why the a-SiO_2 reproduces several macroscopic properties, like transparency in the visible and electrical insulation, typical of α-quartz crystalline SiO_2. These properties are on the basis of many technological applications of a-SiO_2, such as optical fibres and most of the silicon-based metal–oxide–semiconductor

devices.

It is worth to note that the CRN model for the amorphous state is still debated. Other models have been constructed from old crystallite theory that depicted the amorphous as an aggregate of extremely small crystals [4]. Besides, other models derive from computational techniques (molecular dynamics, for example) [5] or from topological construction [6]. Nevertheless, it has been quite well established that the CRN model, in which the SiO_4 tetrahedral units are randomly linked together at the corners, well describes the structure of a-SiO_2.

In the framework of the CRN model, point defects are defined in a straightforward way by extending the models proposed for a crystal. The embedding of defects in the amorphous state has the consequence that, even if they have a well-defined structural identity, they explore various different environments. In general, a point defect can be visualised as a local distortion of the atomic structure caused by a bond rupture, an over or undercoordinated atom, the presence of an impurity atom (homo or heterovalent substitution, interstitialcies), etc. [7]. These defects are usually indicated as *intrinsic* when they are due to irregular arrangements of the crystal atoms (Si and O for SiO_2), and *extrinsic* when they are related to impurities (atoms differing from Si or O).

A further general classification of the point defects can be made on the basis of their electronic configuration: those having unpaired electrons constitute paramagnetic defects, and the others the diamagnetic defects. Both typologies could in principle be characterised by optical activities as absorption and emission bands. Instead, only the paramagnetic defects have a further feature since they are responsible for a non-zero magnetic moment, having unpaired electrons, and are responsible for the magnetic resonance absorption (Electron Param-

agnetic Resonance, EPR).[1]

Examples of point defects are: the *vacancy* (an atom is removed from its 'reticular' position), the *interstitial* (an atom is in a non-reticular position) and the *valence* defect (a break in the Si-O bonds) [1]. In particular, among the intrinsic defects in silica we found:

- the neutral oxygen vacancy: $O \equiv Si - Si \equiv O$
- the peroxy bridge: $O \equiv Si - O - O - Si \equiv O$
- the non-bridging oxygen: $O \equiv Si - O^{\bullet}$ (NBOHC)
- the tricoordinated silicon: $O \equiv Si^{\bullet}$ (E' centre)
- the twofold coordinated silicon: $O = Si^{\bullet\bullet}$.

Some of these defects are shown in figure A.2. It is worth to note that these defects may present several charge states due to electron or hole trapping.

Many extrinsic defects in amorphous silica are associated to metallic, halogen and substitutional elements trapped in the starting materials or involved in the manufacturing procedure. The Germanium (Ge) is particularly important since it is homovalent to Si and it can give rise to defects with analogous structures to the intrinsic defects reported in figure A.2 but with Ge substituting Si. Another impurity that plays a prominent role in amorphous silica is the hydrogen. This is mainly captured during the manufacturing in the form of OH radicals

[1]EPR, also referred to as Electron Spin Resonance (ESR), is a spectroscopic method which detects the presence of unpaired electrons in a sample under test. It can provide meaningful structural and dynamic information, even from ongoing chemical or physical processes without influencing the process itself.

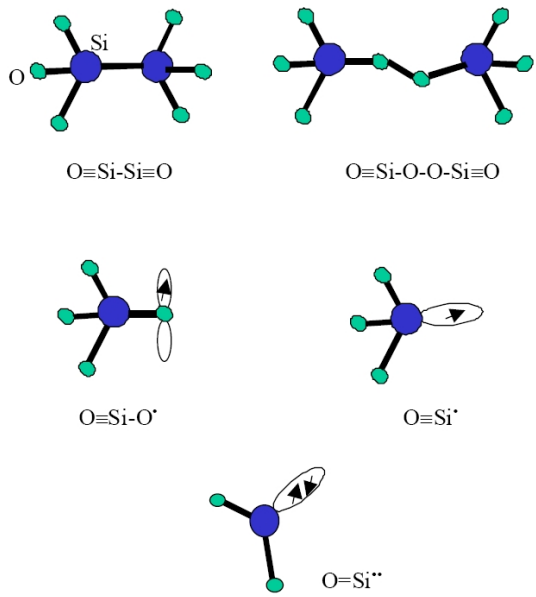

Figure A.2: Fragments of amorphous silica representing various point defects. By arrows are indicated the electron spins, inserted in pictorial orbits.

(from <1 ppm, to ∼1000 ppm) or bonded to Si. Its importance is due to the supposed participation in various generation processes of defects, both intrinsic and extrinsic, and to the high mobility, also at low temperatures [8].

Electronic states (ground and excited) of a point defect may have energy separation lower than the energy-gap (∼ 8 eV) of the silica matrix. The broken bond defects like $O \equiv Si^{\bullet}$ or $O = Si^{\bullet\bullet}$, for instance, are related to the (anti-bonding) localised states that should actually be found between the valence and the conduction band [8]. As a consequence, the

transitions among electronic states of the defect, induced by the electromagnetic field, give rise to absorption and emission bands with energy spanning from below $\sim$ 2 eV, in the visible range, up to $\sim$ 8 eV, in the vacuum UV (VUV) region, thus explaining the loss of transparency of the material. In addition, the defects may trap charges, electrons or holes, hence influencing the insulation properties of silica. Finally, in the case of paramagnetic defects, a redistribution of the electronic levels, related to the presence of a magnetic field, is introduced with very low separation energy ($\sim$10 meV), which induces variations in the magnetic properties of the material.

A.2 Formation processes of point defects

The origin of point defects has to be found in the manufacturing and the history of the material. The same traditional production of a-SiO_2, in fact, implies its rapid cooling (quenching) from a high temperature melt ($\sim$2000 K) with the ensuing formation of intrinsic defects [1]. Also, depending on the starting material used in the melt and on the atmosphere of the manufacturing process, some impurities may be trapped. On the basis of the traditional commercial manufacturing procedures four main typologies of high purity silica glasses have been distinguished. In general, they contain different low concentrations of metallic, OH and other impurities:

- **Type I (natural dry)**: fusion of quartz powder by electric arc in a crucible in vacuum or inert gas atmosphere at low pressure. [OH] $<$ 30 ppm; other impurities, usually less than 10 ppm.
- **Type II (natural wet)**: flame fusion of quartz powder in water vapour atmosphere. [OH] = 150 $\div$ 400 ppm;

other impurities are less than the starting material because some of them are volatilised in the flame.

- **Type III (Synthetic wet)**: hydrolysis of pure silicon compounds, usually $SiCl_4$, injected in gas-phase into a hydrogen/oxygen flame. Actually, the process is an oxidation, since the compound is transformed in the flame into fused drops of SiO_2. [OH] $\geq$100 ppm; other impurities content negligible since the starting material contains much less impurities than the natural quartz.

- **Type IV (Synthetic dry)**: Reaction of O_2 with $SiCl_4$ in water-free-plasma. [OH] $<$ 1 ppm; other relevant impurity: [Cl] $\sim$ 100 ppm

It is worth to note that comparison of the point defects in these four silica types may be useful to evidence if a defect is related with a particular impurity, for example containing it, or if the defect induction is favored by the impurity, as evidenced for the hydrogen [8].

Of course, post-manufacture treatments of the material can also produce defects [9]. In particular, it is known that defects may be induced or transformed after the exposure to special atmosphere, heating, drawing, as in the production of optical fibers [10], exposure to particle or ionising radiation, etc. [1]. The examination of the external treatments effects has been and is still of basic importance in the physics of defects in solids since it gives useful information on their atomic structures and generation mechanisms. A given external treatment may cause the appearance, the increment or the reduction of a specific macroscopic property (e.g., an optical absorption band, an EPR signal, etc...). The variations (growth, reduction or bleaching, thermal annealing) of these physical properties may

be measured as a function of the time duration or intensity of the external treatment and often they can evidence correlation (or anti-correlation) among kinetics of the different properties.

A lot of progresses in the knowledge of defects is related to the individuation of these correlations, which may be used to clarify the different phenomenologies of the properties related to defects. Besides, the correlations may put in evidence conversion mechanisms from a type of defect to another, giving precious information to identify their atomic structures. By this way it can be evidenced if the defects arise from the unperturbed matrix or from a pre-existing defect, named *precursor*.

A particularly useful technique in the investigation of the mechanisms of defect generation is the irradiation of silica with beam of particles (electrons, neutrons, ions, etc.) or ionising radiation (UV, X, g, etc.) [11]. Three main mechanisms are distinguished [1]:

- the *knock-on processes*, in which atomic displacements are caused by the direct transfer of the projectile kinetic energy;
- the *radiolysis processes*, in which atomic motion or bond ruptures are caused through ionisation or electron excitation;
- the *electronic rearrangement processes*, in which the electrons or holes resulting from the excitation can either be trapped into diamagnetic defects or can cause bonds to break.

The radiation induced defects include all the typologies encountered in vitreous silica, vacancy, interstitial and valence defects. By this method, the characterisation of a wide variety

of defects is thus possible. The kinetics of variation of the defects can be easily investigated by varying the irradiation time or intensity. As an example, when the concentration of a radiation induced defect reaches a constant value after a prolonged irradiation, the existence of a precursor can be reasonably assumed. In fact, the irradiation process converts the precursor until they are exhausted. Also, since some of the irradiation processes may occur only at a given energy, the selection of an appropriate beam can discriminate the reaction mechanisms.

Thermal annealing is another external treatment which is frequently used for the investigation of point defects. In fact, many varieties of radiation-induced defects can be destroyed on increasing the temperature, as for the case of the E' centres [8].[2] In general, by warming an irradiated material it is possible to individuate the temperature at which a given defect is destroyed. By this way, useful information related to the defect structure, as for example the strength of the molecular-bonds and the depth of the defect potential well, can be obtained.

A.3 Radiation-damage processes

Knock-on processes

In the knock-on processes the projectile particles of the incident beam interact directly with the atoms of the material causing displacements (for example, vacancy-interstitial Frenkel pair) or site distortions. Two kinds of knock-on processes are generally considered: the elastic, that conserves the total kinetic energy, and the inelastic, in which some of the

[2]The E' centres identify the situation in which an electron is trapped in the sp^3 hybrid orbital of Si at the site of an oxygen vacancy.

projectile kinetic energy is lost in electronic transitions (excitation, ionisation,...) or nuclear reactions [1]. In order to create defects by displacements, it is necessary that the projectile gives sufficient energy to the target atom to break its bonds and to prevent that the knocked-on atom is recaptured from its neighboring atoms. The value of this energy for a given atom in the matrix is called displacement energy T_d, and it has been estimated that, in SiO_2, $T_d^O \approx 10$ eV and $T_d^{Si} \approx 20$ eV, for O and Si displacements, respectively, assuming a Si-O bond energy of $\sim$5 eV [12]. The environment of the knocked-on atom influences these energies and in general they are found to depend both on the topological arrangement and on the temperature.

Several types of radiation may produce displacements by knock-on collisions: fast neutrons, thermal neutrons, energetic ions, energetic electrons and γ-rays (through the generated electrons). Cascades of knock-on may also occur in the case of energetic particles when they transfer a large amount of kinetic energy to the displaced atoms [13].

Radiolytic processes

In radiolytic processes the irradiation primarily changes the state of an electron, but no stable ionic or atomic defects are initially formed [1, 11]. The energy absorbed appears in the form of electrons in a normally empty conduction band and holes in the normally occupied valence bands, or in the form of excitons (electron-hole pairs bound to each other) at some site of the material. These excitations can be considered just as a first step and are followed by other processes that lead to stable electronic states. A significant fraction of these electron-hole pairs recombine radiatively (inducing luminescence) or are

separately trapped on impurities, on pre-existing defects or on radiation-induced defects, or are absorbed in non-radiative processes involving phonons. Finally, if the electron-hole pair recombines non-radiatively and its energy is focused on an atom it may be converted into kinetic energy of the latter (as for example an ion repelled by electrostatic forces), resulting in bond ruptures or in the creation of vacancy-interstitial pairs.

The radiolysis processes (electronic excitation, ionisations and bond rupture) have been found to be predominant in electron and γ-irradiation as they overcome the efficiency of the knock-on processes by at least an order of magnitude [1].

Among the various irradiation damage sources the γ-rays are very interesting. They can act through photoelectric effect, Compton effect and pair production (electron-positron) [14] and give rise to primary electrons and a cascade of scattered energetic electrons and photons. The electrons produced by γ-rays are sufficiently energetic to induce knock-on as well as radiolysis processes. In this respect, the path of a γ-ray through the matrix can be visualised as a succession of electrons, ions and excited molecules that may directly produce defects or may diffuse outside the path to react with other sites of the material.

Metamictisation

A final interesting aspect regards the limit of very high doses of irradiation. In particular, after prolonged irradiation, the physical properties (density, refractive index, elastic constants) of crystalline and amorphous SiO_2 become almost identical and, in addition, a common amorphised structure is observed [15]. This state is also almost independent of the irradiation process (knock-on or radiolysis), and is distinguishable from or-

dinary non-irradiated vitreous silica since it has density slightly higher by 3-4%. This heavily damaged state of SiO_2 is known as *metamict* state [1, 16, 17] and is considered to arise through different stages involving point defects. In particular, it has been proposed that the metamictisation process is a structural relaxation triggered by a critical defects concentration, since the latter provides enough freedom to influence the atomic network connectivity [18, 19]. For example, in quartz it has been supposed that point defects progressively lower the network connectivity, until the solid can no longer freely accommodate additional point defects, and a rearrangement of the damaged network takes place. The transition to the metamict state should thus be definitely considered as a cooperative effect resulting from the presence of point defects [20].

Bibliography

[1] S. R. Elliott, *Physics of amorphous solids.* Longman Inc., NY, 2nd ed., 1983.

[2] S. Agnello, *Gamma ray induced processes of point defect conversion in silica.* PhD thesis, Dip. Scienze Fisiche e Astronomiche, Università di Palermo, 2000.

[3] W. H. Zachariasen, "The atomic arrangement in glass," *J. Am. Chem. Soc.*, vol. 54, pp. 3841–3851, 1932.

[4] E. Porai-Koshits in *Glass science and technology* (D. Uhlmann and N. Kreidl, eds.), Academic Press, 1990.

[5] P. Jund and R. Jullien, eds., *Physics of glasses.* AIP 489, 1999.

[6] R. Devine, J. Duraud, and E. Dooryhée, eds., *Structure and imperfections in amorphous and crystalline silicon dioxide.* John Wiley & Sons, 2000.

[7] C. Kittel, *Introduction to solid state physics*, ch. 5. John Wiley & Sons, Inc., 4th ed., 1971.

[8] D. Griscom, "Defect structure of glasses : Some outstanding questions in regard to vitreous silica," *J. Non-Cryst. Solids*, vol. 73, pp. 51–77, 1985.

[9] C. de Novion and A. Barbu in *Materials under irradiation* (A. Dunlop, F. Rullier-Albenque, C. Jaouen, C. Templier, and J. Davenas, eds.), Trans Tech Publications Ltd, 1993.

[10] H. Rawson, *Glasses and their applications.* The Institute of Metals, 1991.

[11] J. J. Cawford and L. Slifkin, eds., *Point defects in solids*. Plenum Press, New York, 1972.

[12] W. Primak, "Threshold for radiation effects in silica," *Phys. Review B*, vol. 6, no. 12, pp. 4846–4851, 1972.

[13] N. Doan and F. Rossi in *Materials under irradiation* (A. Dunlop, F. Rullier-Albenque, C. Jaouen, C. Templier, and J. Davenas, eds.), Trans Tech Publications Ltd, 1993.

[14] E. Balanzat and S. Bouffard in *Materials under irradiation* (A. Dunlop, F. Rullier-Albenque, C. Jaouen, C. Templier, and J. Davenas, eds.), Trans Tech Publications Ltd, 1993.

[15] G. Arnold, "Ion implantation effects in crystalline quartz," *Nucl. Instr. Meth. in Phys. Res. B*, vol. 65, pp. 213–216, 1992.

[16] A. Pabst, "The metamict state," *Am. Mineralogist*, vol. 37, pp. 137–157, 1952.

[17] W. Primak, "The compacted states of vitreous silica," in *Studies of Radiation Effects in Solids* (G. Dienes and L. Chadderton, eds.), Gordon and Breach, NY.

[18] N. Itoh, "Self-trapped exciton model of heavy-ion track registration," *Nucl. Instr. Meth. in Phys. Res. B*, vol. 116, pp. 33–36, 1996.

[19] L. Douillard and J. P. Duraud, "Swift heavy ion amorphization of quartz: a comparative study of the particle amorphization mechanism of quartz," *Nucl. Instr. Meth. in Phys. Res. B*, vol. 116, pp. 212–217, 1996.

[20] L. Douillard and J. P. Duraud, "Amorphization of α-quartz under irradiation," *J. Phys III France*, vol. 6, pp. 1677–1687, 1996.

Publications

[1] A. Vedadi, D. Alasia, E. Lantz, H. Maillotte, L. Thévenaz, M. González-Herráez, and T. Sylvestre, "Brillouin optical time domain analysis od fiber optic parametric amplifiers," *to be presented at the 32nd European Conference on Optical Communication (ECOC 2006)*, Cannes, France, 24-28 September 2006.

[2] D. Alasia, A. Fernandez Fernandez, B. Brichard, L. Abrardi, and L. Thévenaz, "The effects of gamma-radiation on the properties of Brillouin scattering in standard Ge-doped optical fibres," *Meas. Sci. Technol.*, vol. 17, pp. 1091–1094, May 2006.

[3] D. Alasia, M. González Herráez, L. Abrardi, S. Martin López, and L. Thévenaz, "Detrimental effect of modulation instability on distributed optical fibre sensors using stimulated Brillouin scattering," in *17th International Conference on Optical Fibre Sensors* (Marc Voet, Reinhardt Willsch, Wolfgang Ecke, Julian Jones, Brian Culshaw, ed.), pp. 587–590, Proceedings of SPIE Vol. 5855, SPIE, Bellingham, WA, 2005.

[4] D. Alasia, A. Fernandez Fernandez, B. Brichard, L. Abrardi, and L. Thévenaz, "Study of the radiation effects on the properties of Brillouin scattering in standard Ge-doped optical fibres," in *17th International Conference on Optical Fibre Sensors* (Marc Voet, Reinhardt Willsch, Wolfgang Ecke, Julian Jones, Brian Culshaw, ed.), pp. 180–183, Proceedings of SPIE Vol. 5855, SPIE, Bellingham, WA, 2005.

[5] L. Thévenaz, D. Alasia, S. Le Floch, and J. Troger, "Generation of high-quality signals for optical sensing using DFB injection locking lasers," *Proceedings of the SPIE - The International Society for Optical Engineering*, vol. 5502, no. 1, pp. 556–559, 2004.

[6] L. Thévenaz, S. Le Floch, D. Alasia, and H.-J. Troger, "Novel schemes for optical signal generation using laser injection locking with application to Brillouin sensing," *Meas. Sci. Technol.*, vol. 15, pp. 1519–1524, August 2004.

[7] D. Alasia and L. Thévenaz, "A novel all-fibre configuration for a flexible polarimetric current sensor," *Meas. Sci. Technol.*, vol. 15, pp. 1525–1530, August 2004.

[8] F. Briffod, D. Alasia, L. Thevenaz, G. Cuenoud, and P.-A. Robert, "Extreme current measurements using a fibre optics current sensor," *15th Optical Fiber Sensors Conference Technical Digest. OFS 2002 (Cat No.02EX533)*, May 2002.

Nomenclature

List of symbols

α	Attenuation coefficient
α_m	Laser cavity loss
α_{int}	Laser internal loss
β	Optical propagation constant, FM modulation index
β_c	Linewidth enhancement factor
β_2	Second-order dispersion term
β_3	Third-order dispersion term
β_a	Propagation constant of the anti-Stokes wave
β_i	ith-order dispersion term
β_p	Propagation constant of the pump wave
β_s	Propagation constant of the Stokes wave
χ	Mean dielectric susceptibility

χ_{xxxx}	Unique non-zero component of $\boldsymbol{\chi}^{(3)}$
$\Delta\epsilon$	Scalar fluctuations of the dielectric constant
$\Delta\nu_B$	Brillouin linewidth
$\Delta\omega$	Spectral width
$\delta\omega$	Angular frequency broadening of spontaneous Brillouin scattering
$\Delta\rho$	Density variations
Δp	Pressure fluctuations
Δs	Entropy fluctuations
ϵ_0	Vacuum permittivity
ϵ_{NL}	Non-linear dielectric constant
$\eta(z)$	Normalised dimensionless pump wave amplitude
η_i	Laser internal quantum efficiency
η_b	Bulk viscosity coefficient
η_P	Polarisation efficiency of the Brillouin process
η_s	Shear viscosity coefficient
Γ	Acoustic damping coefficient, laser confinement factor
γ	Non-linear coefficient of the fibre, photon loss
Γ_B	Modified acoustic damping coefficient
γ_e	Electrostrictive constant, laser total carrier loss

κ	Thermal conductivity
κ_L	Normalised linear mismatch
κ_{NL}	Normalised non-linear mismatch
λ	Optical wavelength
λ_0	Zero-dispersion wavelength
λ_p	Wavelength of the pump optical wave
λ_s	Wavelength of the signal optical wave
μ_0	Vacuum permeability
ν	Poisson's number
ν_B	Brillouin frequency shift; acoustic wave frequency
ν_p	Pump lightwave frequency
ν_S	Stokes lightwave frequency
Ω	Angular frequency of the MI perturbation
ω, ω'	Angular frequency
ω_{th}	Angular frequency of the slave laser at threshold
Ω_c	MI critical angular frequency
ω_i	Angular frequency of the idler optical wave
Ω_{max}	Angular frequency at which the MI gain is maximum
ω_p	Angular frequency of the pump optical wave

ω_s	Angular frequency of the signal optical wave
$\Phi(\xi)$	Phase of the FWM process
ϕ_s, ϕ_m	Slave and master laser phases
ϕ_{NL}	Non-linear phase shift
$\phi_{p,S}^{SBS}$	Additional phase shifts on the pump and Stokes waves induced by the Brillouin process
ρ	Free charges density, material density, injection-locking ratio
ρ_0	Mean density of the material
τ_π	Acoustic phonons lifetime
τ_L	Cavity round-trip time
τ_R	Vibrational time delay
τ_g	Group delay per unit length
ξ	Longitudinal scaled distance
ζ	Injection-locking coupling factor
$\boldsymbol{\chi}$	Susceptibility tensor
$\boldsymbol{\chi}^{(1)}$	First-order susceptibility tensor
$\boldsymbol{\chi}^{(2)}$	Second-order susceptibility tensor
$\boldsymbol{\chi}^{(3)}$	Third-order susceptibility tensor
$\boldsymbol{\Delta\chi}$	Tensor representing the temporal fluctuations in the dielectric susceptibility

$\boldsymbol{\Delta\epsilon}$	Tensor representing the temporal fluctuations in the dielectric tensor
$\boldsymbol{\Delta\epsilon}^a$	Anti-symmetric part of $\boldsymbol{\Delta\epsilon}^t$
$\boldsymbol{\Delta\epsilon}^s$	Symmetric part of $\boldsymbol{\Delta\epsilon}^t$
$\boldsymbol{\Delta\epsilon}^t$	Traceless tensor describing the contribution of the fluctuations to the dielectric tensor
$\boldsymbol{\epsilon}$	Dielectric tensor
$\Delta\omega$	Angular frequency difference between master and slave laser
$\tilde{\boldsymbol{\chi}}^{(1)}$	Fourier transform of the linear susceptibility tensor
$\hat{n}_1$	Fibre core refractive index
$\hat{n}_2$	Fibre cladding refractive index
$\hat{x}$	Unit polarisation vector
$\tilde{A}(\omega)$	Amplitude function
$\tilde{E}_z$	Longitudinal component of the electric field
$\tilde{H}_z$	Longitudinal component of the magnetic field
a	Fibre core radius
$a(z,\tau)$	Amplitude of the MI perturbation
$A(z,t)$	Longitudinal slowly-varying amplitude
A_s, A_m	Slave and master laser slowly varying field amplitudes

$a_a(z)$	Normalised dimensionless anti-Stokes wave amplitude
A_{eff}	Effective core area
$a_s(z)$	Normalised dimensionless Stokes wave amplitude
c	Vacuum light speed
c_p	Specific heat at constant pressure
C_s	Adiabatic compressibility
D	Chromatic dispersion
E	Young modulus
E_s, E_m	Slave and master laser complex electric field
E_a	Electric field of the anti-Stokes wave
E_p	Electric field of the pump wave
E_s	Electric field of the Stokes wave
$E_{p,S}$	Pump and Stokes wave amplitudes involved in the Brillouin process
$F(\rho)$	Modal function
f_R	Fractional contribution of the delayed Raman response to the non-linear response of the fibre
G	Integrated modulation-instability gain
g	Parametric gain coefficient
$g(\Omega)$	MI spectral gain

$G(t)$	Modal gain per unit time
g_B	Line-centre Brillouin gain factor
$g_B(\nu)$	Brillouin gain spectrum
g_{max}	Maximum MI gain
G_s	Unsaturated single-pass parametric gain
$H(\eta, \Phi)$	Hamiltonian of the TWM process
h_R	Raman response function
I	Optical intensity
$I_{p,S}$	Pump and Stokes intensities involved in the Brillouin process
K	Bulk modulus
K	Wave number of the MI perturbation
k_0	Optical wavevector
L_D	Dispersion length
L_{eff}	Effective interaction length
L_{NL}	Non-linear length
M	AM power modulation index
m	Integer identifying the fibre mode
N	Order of the soliton, laser free charge carrier number
n	Refractive index

n_0	Linear refractive index
n_2	Non-linear refractive index
p	Pressure
P_{out}^{fr}	Free-running laser output power per facet
P_m	Master laser injected photon number
P_s	Slave laser intracavity photon number
p_{12}	Longitudinal elasto-optic coefficient
P_{sat}	Laser saturated photon number
P_s	Power of the signal optical wave
q	Optical wave vector modulus
R_{sp}	Laser spontaneous emission rate
S	Boundary surface of V
s	Entropy
T	Temperature
t	Time
T_0	Initial width of a pulse propagating in the fibre
$u(\theta, \zeta)$	Soliton optical wave
V	Volume
v_g	Group velocity
V_P	Volume of the laser optical mode

v_a	Velocity of sound
W	Electrical energy dissipated within a dielectric medium; total work
L	Optical fibre length
$\mathbf{B}$	Magnetic induction vector
$\mathbf{D}$	Electric displacement vector
$\mathbf{E}$	Electric field vector
$\mathbf{e}_{p,S}$	Unit polarisation vectors
$\mathbf{E}_p$	Pump optical wave
$\mathbf{E}_S$	Stokes optical wave
$\mathbf{f}$	Electrostrictive force density per unit volume
$\mathbf{H}$	Magnetic field vector
$\mathbf{I}$	Identity tensor
$\mathbf{J}$	Current density vector
$\mathbf{k}, \mathbf{k}^{'}$	Optical wave vector
$\mathbf{M}$	Magnetisation vector
$\mathbf{P}$	Polarisation vector
$\mathbf{P}_L$	Linear polarisation vector
$\mathbf{P}_{NL}$	Non-linear polarisation vector
$\mathbf{P}_{p,S}^{NL}$	Nonlinear polarisation terms originating from electrostriction

$\mathbf{q}$	Optical wave vector
$\mathbf{r}$	Displacement vector
$\mathbf{v}$	Matter displacement velocity vector
$\tilde{\mathbf{E}}$	Fourier transform of the electric vector
$\tilde{\mathbf{P}}_L$	Fourier transform of the linear polarisation
$\bullet$	Symbol denoting a hole centre in a chemical element

List of acronyms

AM	Amplitude modulation
BOTDA	Brillouin optical time domain analysis
BOTDR	Brillouin optical time domain reflectometry
BPF	Band-pass filter
CARS	Coherent anti-Stokes Raman
CD	Chromatic dispersion
CRN	Continuous random network
CW	Continuous wave
DFB	Distributed-feedback laser
DFG	Difference-frequency generation
DSF	Dispersion shifted fibre
EAM	Electro-absorption modulator

EDFA	Erbium-doped fibre amplifier
EOM	Electro-optic modulator
EPR	Electron paramagnetic resonance
ESR	Electron spin resonance
FM	Frequency modulation
FMCW	Frequency-modulated continuous wave
FOPA	Fibre optics parametric amplifiers
FP	Fabry-Pérot
FPU	Fermi-Pasta-Ulam
FWM	Four-wave mixing
FWMH	Full width at maximum half
GOTDR	Gain optical time domain reflectometry
GVD	Group velocity dispersion
HNLF	Highly non-linear fibre
IST	Inverse scattering transform
MFD	Mode field distribution
MI	Modulation instability
NBOHC	Non-bridging oxygen hole centre
NLSE	Non-linear Schrödinger equation
OCDR	Optical coherence domain reflectometry

OR	Optical rectification
OSA	Optical spectrum analyser
OTDR	Optical time domain reflectometry
PC	Polarisation controller
PE	Pockels effect
PG	Parametric gain
PID	Proportional-integral-derivative
POTDR	Polarisation optical time domain analysis
PRBS	Pseudo random binary sequence
RF	Radio frequency
SBS	Stimulated Brillouin scattering
SFG	Sum-frequency generation
SHG	Second-harmonic generation
SMF	Single-mode fibre
SOA	Semiconductor optical amplifier
SPM	Self-phase modulation
SRS	Stimulated Raman scattering
SVEA	Slowly-varying envelope approximation
TE	Transversal electric
THG	Third-harmonic generation

TLS	Two-level system
TM	Transversal magnetic
TWM	Three-wave mixing
XPM	Cross-phase modulation
ZDW	Zero-dispersion wavelength

Alasia Dario

Av. de Saugiaz, 13
1020 Renens (VD), Switzerland
Phone : (+41) 21 693 56 28
Email : dario.alasia@epfl.ch

Born on January the 26th, 1976

Single
Italian

EDUCATION

2001 – to date: **PhD**
Ecole Polytechnique Fédérale de Lausanne (EPFL)
Nanophotonics and Metrology Laboratory
Research domain: nonlinear optics, distributed sensors

1999 – 2001: **Degree in Electrical Engineering**
Ecole Polytechnique Fédérale de Lausanne (EPFL)
Project topic: speech coding algorithms implementation

1995 – 2001: **Degree in Electronic Engineering**
Politecnico di Torino, Italy
Major in microwaves and microelectronics

1990 – 1995: **Italian Baccalaureate in science**
Liceo scientifico "G.B. Bodoni", Saluzzo (Italy)

PROFESSIONAL EXPERIENCES

2001 – to date: *Ecole Polytechnique Fédérale de Lausanne (EPFL)*
Research Assistant
- In charge of the distributed sensors research activity
- In charge of the fibre-optic current sensors project
- Author of scientific publications

Teaching Assistant
- Supervision of seven undergraduate projects
- Responsible for class lectures and laboratory sessions

2001 (2 months): *Institut de Microtechnique (IMT), Université de Neuchatel*
Stage
Training in speech coding techniques and algorithms

LANGUAGES

Italian:	Native language
French:	Native level
English:	Fluent
Spanish:	Conversational level
German:	Basic knowledge

COMPUTER SKILLS

Operating Systems:	Windows 9x/NT, UNIX/Linux, MacOS
Languages:	C, C++, Pascal, Assembly 80x86, Fortran, HTML, Lisp, VHDL
Software:	MS Office, MS Visual Studio, Adobe Suite, Macromedia Suite, Maple, Mathematica, Matlab, Labview, Cadence

NON PROFESSIONAL ACTIVITIES

Sports:	Biking, Swimming, Hiking, Trekking, Climbing
Music:	Pipe organ (professional level), Piano, Harpsichord, Choir direction, Composition, Singing
Hobbies:	Philosophy, Traveling, Reading